Experiments and modelling for glow discharge plasmas applied to niobium sputter deposition in superconducting radiofrequency cavities

Thèse N° 9243

Présentée le 7 juin 2019

à la Faculté des sciences de base
SPC - Physique des Plasmas de Base
Programme doctoral en physique

pour l'obtention du grade de Docteur ès Sciences

par

Thibaut François Hugo RICHARD

Acceptée sur proposition du jury

Prof. H. M. Rønnow, président du jury
Prof. I. Furno, Dr A. Sublet, directeurs de thèse
Prof. D. Depla, rapporteur
Dr A. Pflug, rapporteur
Prof. S. Alberti, rapporteur

2019

ÉCOLE POLYTECHNIQUE
FÉDÉRALE DE LAUSANNE

On pourrait concevoir une série de coordonnées ou d'espaces de phases comme une succession de cribles, dont le précédent chaque fois serait relativement un état chaotique et le suivant un état chaoïde, si bien qu'on passerait par des seuils chaotiques au lieu d'aller de l'élémentaire au composé. L'opinion nous présente une science qui rêverait d'unité, d'unifier ses lois, et aujourd'hui encore chercherait une communauté des quatre forces. Plus obstiné pourtant, le rêve de capter un morceau de chaos même si les forces les plus diverses s'y agitent. La science donnerait toute l'unité rationnelle à laquelle elle aspire pour un petit bout de chaos qu'elle pourrait explorer.

Gilles Deleuze, Félix Guattari, *Qu'est-ce que la philosophie?*, Les Editions de Minuit, 1991.

You get a shiver in the dark
It's raining in the park but meantime
South of the river you stop and you hold everything
A band is blowing Dixie double four time
You feel alright when you hear that music ring.

Dire Straits, *Sultans of Swing*, 1978.

Abstract

Thin film coatings are ubiquitous in modern daily lives, from the semi-conductor industry to aesthetic applications, and rely on the modification of a given material to enhance its surface properties.
At CERN (European Organization for Nuclear Research), thin film coatings are used for several applications related to the accelerator technology field, such as electron cloud mitigation, continuous pumping or radio-frequency (RF) superconductivity.
This PhD thesis aims at studying the use of a Particle-in-Cell Monte Carlo/ Direct Simulation Monte Carlo (PICMC/DSMC) numerical code applied to the modelling of deposition processes. The present study focuses on niobium thin film deposition on copper RF cavities of peculiar geometries and large sizes. Numerical simulations can help to understand and improve process parameters in existing systems, and guide the design of future coating systems such that thin film characteristics can be predicted and expensive times of Research and Development can be reduced.
In the first part of this thesis, critical parameters are identified to provide an accurate modelling of glow discharge plasmas commonly used in coating applications with the PICMC module of the numerical code. A dedicated experimental system is designed to enable both DC diode and DC magnetron operation with a coaxial cylindrical plasma source. Suitable ion-induced secondary electron emission yield and energy distribution are numerically assessed by matching simulated discharge voltages and currents with experimental ones. Simulated local plasma parameters, such as electron density and energy, are compared with experimental measurements obtained with a Langmuir probe.
In the second part, transport simulations of sputtered neutral niobium atoms performed with the DSMC method are validated by comparing simulated deposition rates on a substrate with experimental ones with a compact hollow cathode magnetron sputtering source.
At last, the validated *ab initio* methodology for coating process modelling, from plasma simulation and extraction of sputtering profiles to sputtered niobium atoms transport, is applied to typical coating systems used at CERN. The scalability of low discharge power simulation results to realistic powers is first demonstrated for a planar magnetron source in terms of cathode erosion and deposited thin film thickness profiles. Then, an elliptical RF cavity is used as a case study to apply the full methodology in a real substrate of complex shape. PICMC and DSMC simulation results are further extended towards thin film growth modelling, and simulated thin film morphology is compared with experimental Focused Ion Beam/Scanning Electron Microscopy imaging of the niobium layer.

Keywords:
Particle-in-Cell Monte Carlo, Direct Simulation Monte Carlo, Superconducting coatings, DC sputtering, Film growth simulation

Résumé

Les dépôts de couches minces sont omniprésents dans nos vies quotidiennes, avec des applications dans des domaines aussi différents que l'industrie des semi-conducteurs ou les revêtements esthétiques, et se fondent sur la modification des propriétés de surface d'un matériau donné.
Au CERN (Organisation européenne pour la recherche nucléaire), les dépôts de couches minces sont utilisés dans plusieurs applications liées au domaine de la technologie des accélérateurs de particules, pour la mitigation du phénomène d'*electron cloud*, comme outil de pompage continu ou pour la supraconductivité radiofréquence (RF).
Cette thèse de doctorat a pour objectif d'étudier l'utilisation d'un code numérique *Particle-in-Cell Monte Carlo/ Direct Simulation Monte Carlo* pour la modélisation de procédés de dépôts. Cette étude se focalise sur le dépôt de couches minces de niobium sur des cavités RF en cuivre caractérisées par des géométries de grandes tailles et de formes complexes. Les simulations numériques peuvent permettre de comprendre et d'améliorer les paramètres de procédé de systèmes de dépôt existants, et de guider la conception de futurs systèmes de dépôt afin de prédire les caractéristiques des couches minces et de réduire les temps et coûts de Recherche et Développement.
La première partie de cette thèse se concentre sur l'identification de paramètres critiques permettant une modélisation précise des plasmas à décharge luminescente couramment utilisés dans les applications de dépôt par le module PICMC du code de simulation. Un système dédié est conçu pour être opéré dans les configurations DC diode et DC magnétron avec une source plasma cylindrique coaxiale. Un rendement et une distribution en énergie des électrons secondaires émis par bombardement ionique appropriés sont déterminés numériquement en comparant les tensions et courants de décharge simulés avec leurs équivalents expérimentaux. Les paramètres plasma locaux simulés, comme par exemple les densités et énergies des électrons, sont comparés avec ceux mesurés par une sonde de Langmuir.
Dans la deuxième partie de cette thèse, les simulations DSMC du transport des atomes neutres de niobium pulvérisé sont validées en comparant les taux de dépôt simulés sur un substrat avec leurs équivalents expérimentaux, en utilisant une source de pulvérisation de type cathode creuse magnétron.
Enfin, la méthodologie *ab initio* développée et validée pour modéliser les procédés de dépôts, depuis la simulation du plasma et l'extraction des profils de pulvérisation cathodique jusqu'au transport des atomes de niobium pulvérisés, est appliquée à des systèmes de dépôts typiquement utilisés au CERN. La possibilité d'extension des résultats de simulations effectuées à

basses puissances de décharge vers des puissances réalistes est tout d'abord démontrée en termes de profils d'érosion cathodique et d'épaisseurs de couches minces pour une source magnétron planaire. Ensuite, une cavité RF elliptique est utilisée comme cas d'étude pour valider la méthodologie complète dans un substrat réel de géométrie complexe. Les résultats des simulations PICMC/DSMC sont étendus à la modélisation de croissance de couches minces, et la morphologie simulée des couches de niobium est comparée avec des images expérimentales obtenues par sonde ionique focalisée/microscopie électronique à balayage (FIB/SEM).

Mots-clés :
Particle-in-Cell Monte Carlo, Direct Simulation Monte Carlo, Dépôts supraconducteurs, Pulvérisation cathodique DC, Simulation de croissance de couches minces

Acknowledgements

A PhD thesis is by definition limited in terms of outcomes and duration. Yet, at this moment and as small as my contribution can be, I feel that I have been lucky to meet so many people who, throughout the years, have helped me evolve scientifically, professionally and personally.
For this, I first wish to thank my PhD supervisors Ivo Furno and Alban Sublet, who helped me countless times to refine my thoughts, to give me focus when I was strayed, for their quality of scientific and human interactions and for their trust in my abilities when I was in doubt.
I am also grateful to the members of the jury who agreed to evaluate the present work, and especially to Andreas Pflug for the quality of his numerical code support and scientific exchanges.
I then want to express my appreciation to EPFL, and especially to the director of the Swiss Plasma Center, Ambrogio Fasoli, for accepting me as a doctoral student in their midst.
I also wish to express my deepest thanks to Mauro Taborelli for his presence whenever it was needed and for his comments on the present text, to Paolo Chiggiato without whom I would never have had the chance to step a foot into CERN, and who always renewed his trust in me while keeping me intellectually motivated.
I wish then to give my thanks to my close CERN colleagues: Guillaume, who *tolerated* my presence in a shared office for four years, and was always eager to share both scientific and casual discussions, to Pedro and Fabio, members of the *dramatic pictures lab*, for their enthusiasm and constant joyfulness, and to Valentine for her peculiar thoughts on the life as a PhD student and on human social interactions. My special thanks go to Spyros: in addition to your daily energy and optimism and to your constant practical help in the most dire experimental situations, I mostly enjoyed your freedom of speech and the political discussions we had.
At some point during my work, the development of the HPC cluster infrastructure at CERN started to worry me, and I wish to thank the CERN/IT team for soothing my anxiety. This includes Nils, Carolina, Pablo and Philippe, without whom the present work could not have been possible or at least not in such enjoyable conditions.
I also wish to give a thought to friends met at CERN over the years, either during my PhD or even before. Marton, Akos, Ildi and Cedric, you will always remind me of times of pure fun, when youth came prior to any sense of adulthood and responsibility! Valentin, Hakon, Edgar, you all left too soon but our time together was priceless! Antonios, Theo, Giovanni, you were part of my daily life for so long, and yet always renewed and looking forward. I will keep within me the guitar sessions, the barbecues and the inherent philosophical talks!

Bien que nos rencontres aient été rares durant mes années de thèse, je remercie des amis de longue date rencontrés à Toulouse. Mathieu, Marius, Sébastien, à chacune de nos rencontres ou conversations et quelles que soient nos situations respectives, il me semble que nous ne nous sommes jamais quittés. Antoine, Hélène, merci de m'avoir supporté en coloc, et de fonder la relation d'amitié sur des bases de compréhension et d'entraide profondes, tout en recherchant et en appréciant les instants de pur bonheur partagé. Cette amitié n'a pas de prix.
Mes pensées vont également à Roselyne et Pierre, qui m'ont soutenu dans mon parcours et m'ont aidé à concrétiser le projet d'entrer au CERN quand il était encore dans mon esprit un rêve inaccessible.
Mes remerciements vont aussi à Claudine et Didier, Véronique, Emmanuel, Léo et Anna. Vous m'avez connu pendant tant d'années et m'avez toujours conforté dans mes aspirations. Léo et Anna, perséverez dans vos êtres!
Enfin, ma dernière pensée va à Nicole. Maman, tu as toujours été présente, sans jugements ou pensées *a priori*, au long des années. Sans toi, jamais je n'aurais faite mienne l'idée de toujours hausser la barre, de repousser les limites de mes possibilités, tout en gardant la curiosité de l'enfance et la lucidité d'un adulte. Sans toi, cette thèse ne serait pas advenue.

Meyrin, 8 mars 2019 T. R.

Contents

List of Figures

List of Tables

List of physical constants, conversion factors and practical formulae

Quantity	Symbol	Value
Boltzmann constant	k_B	1.3807×10^{-23} J/K
Elementary charge	e	1.6022×10^{-19} C
Electron mass	m	9.1095×10^{-31} kg
Proton mass	M	1.6726×10^{-27} kg
Permittivity of free space	ϵ_0	8.8542×10^{-12} F/m
Permeability of free space	μ_0	$4\pi \times 10^{-7}$ H/m
Avogadro number	N_A	6.0220×10^{23} molecules/mol
eT[volts]		$k_B T$[kelvins]
1 Pa		10^{-2} mbar
1 Gauss		10^{-4} tesla
1 sccm		4.4780×10^{17} particles/s
1 A		13.9383 sccm
Electron Debye length	λ_{De}	$(\epsilon_0 \mathrm{T_e}/e n_e)^{1/2}$ [m]
Electron plasma angular frequency	ω_{pe}	$(e^2 n_e/\epsilon_0 m)^{1/2}$ [s^{-1}]
Cyclotron angular frequency	Ω_C	eB/m [s^{-1}]

Introduction

Thin film coatings used at CERN (European Organization for Nuclear Research) cover a wide range of applications answering to different specific needs of the particle accelerator field: non-evaporable getters for distributed pumping [1], amorphous carbon for electron cloud mitigation [2], or niobium for the production of superconducting radiofrequency (SRF) accelerating cavities.

The niobium-on-copper deposition technique has been developed and studied at CERN since the Large Electron Positron (LEP) collider era and involves either Direct Current (DC) diode or DC magnetron sputtering configurations for the production of accelerating cavities. Their wide variety of shapes and sizes usually dictates expensive and time-consuming experimental research and development phases to design coating systems suited for each specific object. Superconducting performances of the coated cavities are strongly linked to the resulting thin film morphology [3].

This PhD thesis was motivated by the need to refine sputtering source design by resorting to numerical simulations to obtain qualitative and quantitative understanding and prediction of thin film characteristics for future cavities and coating systems.

The thesis outline is organised as described in figure 1.

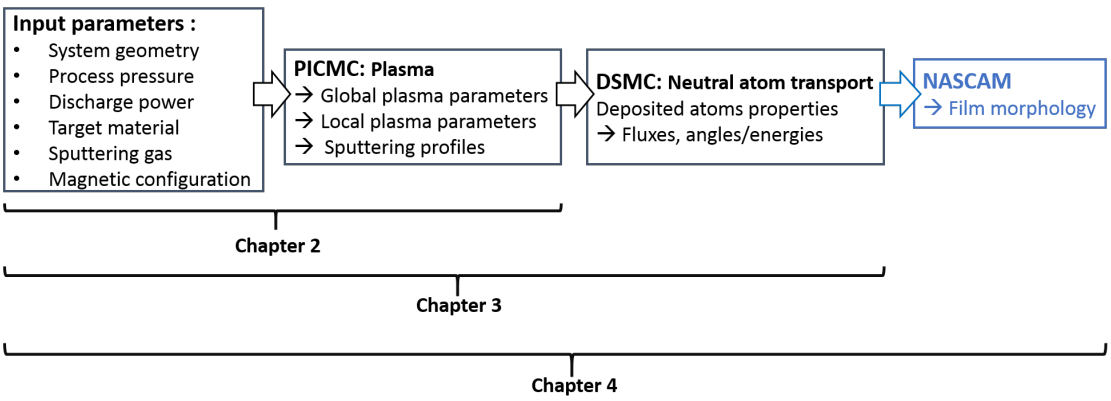

Figure 1 – Thesis outline.

Chapter 1 overviews the general context of superconducting thin film coatings applied to RF cavities, and the different techniques and physical phenomena involved in their coating processes. It also describes the simulation tools used in this thesis.

Chapter 2 focuses on the validation of Particle-in-Cell Monte Carlo (PICMC) plasma simulations [4] against experimental data in a coaxial cylindrical system used in DC diode and DC magnetron, emphasizing the influence of ion-induced secondary electron emission parameters on plasma discharge global parameters. Simulated local plasma parameters are compared with those experimentally measured by a Langmuir probe. The influence of numerical constraints on 2D simulation results is discussed.

Chapter 3 details the methodology used to extract sputtering profiles from the plasma simulations and to use them as input for Direct Simulation Monte Carlo (DSMC) transport simulations of sputtered neutral atoms with the same code [4]. Numerical and experimental deposition rates are compared for a compact hollow cathode magnetron sputtering source.

Chapter 4 focuses on the application of the *ab initio* methodology developed in chapters 2 and 3 to relevant case studies. The extrapolation of low power simulation results to realistic discharge powers is discussed. Then, a real cavity case is presented, for which experimental thin film morphology is compared with simulations using the NASCAM software [5].

Appendix A gives the Matlab code used for sputtering yield computation, based on [6].

Appendix B discusses the discrepancy between sputtering yields based on the full ion energy distribution and those evaluated at the cathode voltage, by summarizing simulated data from all chapters.

Appendix C presents additional preliminary results on the 1.3 GHz elliptical cavity case study in terms of cathode erosion influence on the stability of plasma simulations, and on the change of process gas from argon to krypton.

1 Context of the study

In particle accelerators, charged particle acceleration is driven by the application of an oscillating radiofrequency (RF) electric field into resonant elements (cavities), such that synchronization of the field frequency with passing particles provides them with an accelerating electric field.

In order to minimize the RF losses on the cavity walls and enhance the accelerating gradient, superconducting niobium has been used preferentially to produce these cavities, because it has the highest critical temperature ($T_c = 9.25K$) and the highest lower critical magnetic field strength H_{c1} of all pure metals [7]. By placing such objects in cryostats cooled with liquid helium (4.2 K for niobium-on-copper coated cavities) or superfluid helium (1.8 K for niobium bulk), the RF surface resistance of superconducting niobium is reduced to less than a thousandth of copper resistance. For example, RF surface resistance of high conductivity copper at 500 MHz and room temperature is 5.8 $m\Omega$ while at the same frequency and 4.2 K, the BCS (Bardeen-Cooper-Schrieffer) surface resistance of niobium is 70 $n\Omega$ [8, Superconducting cavities (Part 1 and 2)]. Hence, the power dissipated as heat during RF operation is greatly reduced, and energy coupling to the beam is improved such that higher accelerating gradients can be obtained.

In the 1980s at CERN, the Large Electron Positron (LEP) collider upgrade required the installation of 288 superconducting radiofrequency (SRF) cavities in the accelerator ring, driving research to find alternatives to expensive bulk niobium cavities [9]. To achieve better thermal stability (resilience to quenches) and reduced material cost, the idea of coating a niobium thin film onto a copper bulk cavity was successfully explored. Since then, niobium deposition onto copper substrates of complex shapes by means of DC diode and magnetron sputtering has become a well-known and mature technique [3].

In the present work, SRF cavities are only considered as a diversity of large and complex shaped copper objects onto which a niobium thin film has to be coated. As such, the correlation between thin film properties and SRF properties will not be directly discussed, but general thin film layer properties required for SRF applications will be detailed in section 1.1.5. Examples

of cavity geometries are given in figure 1.1, illustrating the challenges of coating such objects.

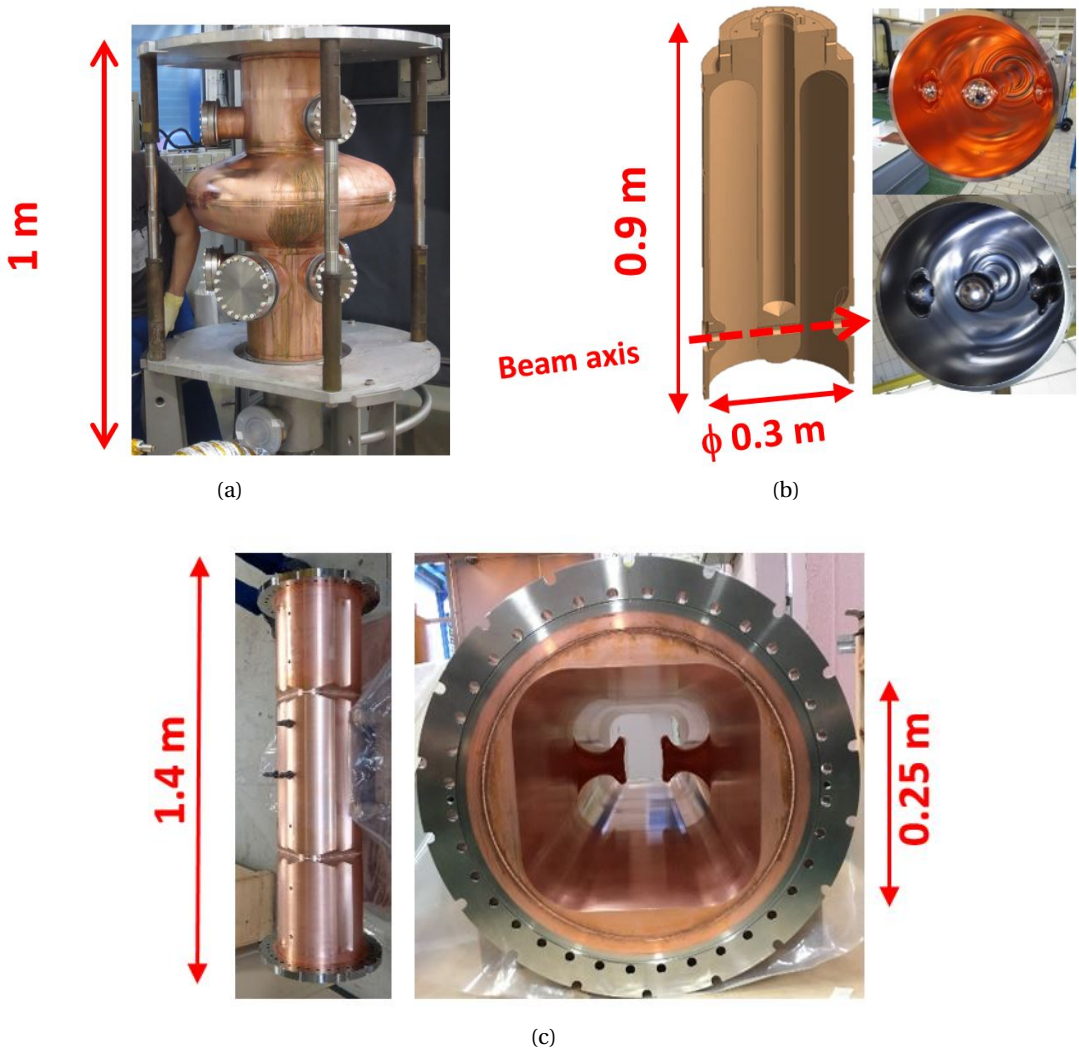

(a) (b)

(c)

Figure 1.1 – (a) LHC elliptical cavity (400 MHz) (b) HIE-ISOLDE Quarter Wave Resonator [10] (101.28 MHz) CAD view, pictures before and after coating (c) Wide Open Waveguide [11], niobium-on-copper crab cavity for the FCC project (400 MHz).

All sputtering techniques described in the following belong to the physical vapour deposition (PVD) group, since the grown niobium films require high purity to optimise superconducting performances. Thus, the use of other techniques such as chemical vapour deposition (CVD) or plasma-enhanced CVD is ruled out for SRF applications, because such techniques employ chemical precursors which are sources of contamination for the SC films.

Some alternatives to conventional DC sputtering for SRF cavity coatings, which are beyond the scope of this work, are currently investigated and include energetic condensation techniques such as electron cyclotron resonance (ECR) plasmas, vacuum arc deposition and high power

impulse magnetron sputtering (HiPIMS) [7].

In this introductory chapter, we first describe the fundamentals of DC plasma glow discharges and the physical processes that are involved in thin film deposition applications. In the second part, we present the numerical tools used in this work to model these processes, with an emphasis on the Particle-in-Cell Monte Carlo (PICMC) and Direct Simulation Monte Carlo (DSMC) modules of a numerical code developed at the Fraunhofer Institute for Surface Engineering and Thin Films IST [4].

1.1 Direct Current plasma discharges applied to thin film coatings

We describe here the working principles governing DC plasma discharges and how the physical sputtering occurring on the negatively biased cathode can be used for thin film deposition. We will consider in this work that the ion population of the plasma is solely made of positively charged ions. This assumption is justified because we only use noble gases (mostly argon). Furthermore, we assume that these ions are at most singly charged because of the low degree of ionisation of the discharges described in this manuscript.

1.1.1 DC diode glow discharge

1.1.1.1 Characteristics of a glow discharge

Glow discharge plasmas have been discovered and studied since the early 1800's, such that abundance of details can be found in the literature [12], [13, chapter 8], [14, chapter 14].

Commonly to other types of plasmas, glow discharge plasmas are defined as an ionized gas in which the sum of positive and negative charges is on average zero (quasi-neutrality). As seen in figure 1.2, they belong to the group of weakly ionized plasmas, meaning that their density of charged particles (ranging from $\sim 10^{12}$ m^{-3} to $\sim 10^{19}$ m^{-3}) is only a small fraction of the density of neutral gas atoms. Furthermore, the fraction of electron energy transferred to process gas atoms by elastic collisions is much smaller than the one of ions colliding with neutrals due to the mass ratio difference between electrons and ions with respect to the mass of neutrals. Therefore, electron temperatures T_e are larger than ion temperatures (the ions are said to be *thermalised*). This is why glow discharge plasmas are also qualified as non-equilibrium *cold plasmas*.

A charged particle placed in the plasma bulk attracts charged particles of the opposite sign, and its electric potential exponentially decays with a typical dimension called the *Debye length*,

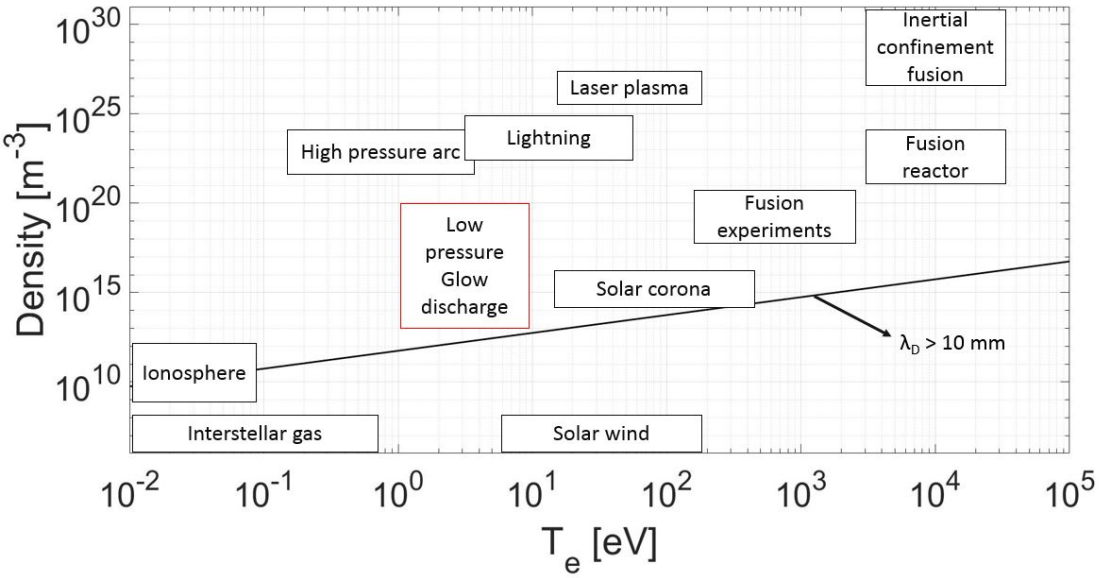

Figure 1.2 – Ranges of plasma as a function of density [m^{-3}] and electron temperature T_e [eV]. Low pressure glow discharge plasmas are highlighted in red. Adapted from [14, Figure 1.7].

defined as :

$$\lambda_D = \sqrt{\frac{\epsilon_0 T_e}{e n_e}} \quad [\mathrm{m}], \tag{1.1}$$

where ϵ_0 is the permittivity of free space (ϵ_0 = 8.8542x10^{-12} [F/m]), T_e [eV] is the electron temperature, e is the elementary charge (e = 1.6022x10^{-19} [C]) and n_e [m^{-3}] is the electron density. After a few Debye lengths, the electric potential generated by the single charge is *screened* by the surrounding charges of opposite sign, which explains the plasma bulk quasi-neutrality.

1.1.1.2 Gas breakdown

The typical Direct Current (DC) diode configuration consists of two metallic parallel plates (electrodes) separated by a gap filled with a sub-atmospheric pressure of process noble gas (e.g. argon). When a negative voltage is applied on one of the electrodes (cathode) while keeping the other one grounded (anode), an electric field is created in their gap d. The voltage-current characteristic curve of a gas breakdown leading to the glow discharge regime is shown in figure 1.3.

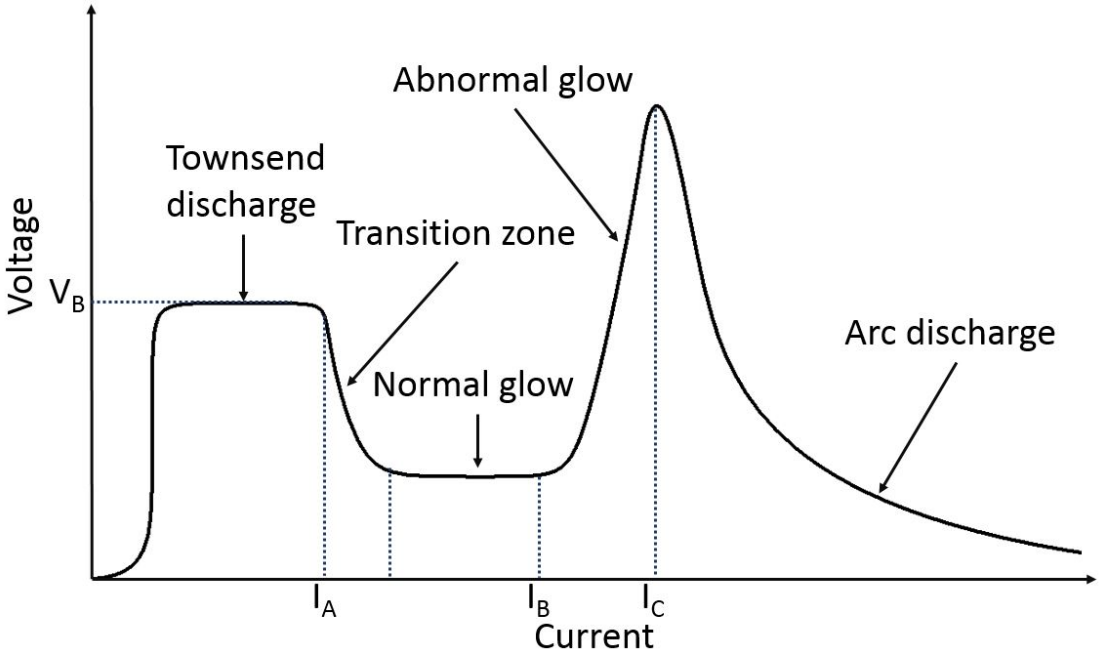

Figure 1.3 – Typical voltage/current characteristic of a gas breakdown leading to the DC glow discharge regime. Adapted from [12, Figure 1], [14, Figure 14.2], [13, Figure 8.4], [15, Figure 13.2].

At first, seeding electrons present in small density in the inter-electrodes gap volume due to background radiation (e.g. cosmic rays ionization or natural radioactivity) are accelerated from the cathode towards the anode. By increasing the voltage, enough energy is given to these electrons such that they start ionizing gas atoms. Newly created ions generate secondary electrons upon bombardment of the cathode, which are in turn accelerated away from the cathode and contribute to gas ionization and an increase in current. The discharge enters the Townsend regime, and the *breakdown voltage* V_B is reached once ion generation and subsequent electron emission balance electron collection. Secondary electrons sourced into the plasma volume lead to an ionization avalanche and an increase of discharge current while the voltage remains constant. As charged particles densities grow in the gap volume, space charge effects develop, and after a transition regime above I_A the *normal glow discharge* regime is reached. Its name stems from atoms excited by electron impact emitting visible radiation through de-excitation transitions. Such a discharge can be seen in figure 1.4, with the pink-purple characteristic color of an argon plasma, and with visible striations.

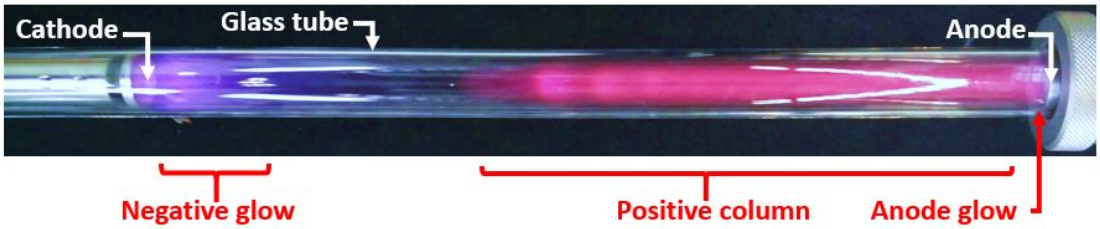

Figure 1.4 – Photograph of a Direct Current glow discharge in a glass tube. Argon pressure of ~ 0.1 mbar. Cathode and anode disks made of niobium. Picture taken from a CERN setup used for demonstration purposes.

The normal glow discharge regime is characterised by a constant voltage, while the current can be increased if enough power is supplied by an enlargement of the ion-bombarded surface of the cathode up to the current value I_B. After this point, a rise in voltage results in a current increase due to an augmented current density at the cathode surface while keeping the surface of ion bombardment constant. This regime located between I_B and I_C is called the *abnormal glow*, and is commonly used for sputtering applications[12]. A further increase in discharge current above I_c initiates a transition towards the arc discharge regime, characterised by an abrupt drop in discharge voltage and increase in discharge current.

The transition from the non-self-sustained discharge to the Townsend discharge can be analytically described with the following condition:

$$\alpha d = \ln\left(1 + \frac{1}{\gamma_{IISEE}}\right), \qquad [14, \text{p. } 544] \tag{1.2}$$

where α [cm^{-1}] is the *first Townsend coefficient* corresponding to the inverse of an ionisation mean free path, d [cm] is the inter-electrode distance, and γ_{IISEE} is the *second Townsend coefficient* which corresponds to the number of secondary electrons emitted from the cathode surface under ion bombardment:

$$\gamma_{IISEE} = \frac{\text{Number of secondary electrons}}{\text{Number of bombarding ions}}. \tag{1.3}$$

The value of γ_{IISEE} depends on the process gas and on the cathode material, as will be detailed in section 1.1.1.4. In the case of parallel electrode plates, α can be expressed with the following empirical formula:

$$\alpha = Ap\exp\left(-\frac{Bpd}{V}\right), \qquad [14, \text{p. } 545] \tag{1.4}$$

where A [cm^{-1}Torr^{-1}] and B [Vcm^{-1}Torr^{-1}] are empirical parameters depending on a given process gas and on the electric field E = V/d, p is the process gas pressure [Torr] and V [V] is the discharge voltage.

When combining equations 1.2 and 1.4, we obtain the following expression for the breakdown

voltage V_B:

$$V_B = \frac{Bpd}{\ln(Apd) - \ln\left[\ln\left(1 + 1/\gamma_{IISEE}\right)\right]}. \qquad [14, \text{p. } 546] \tag{1.5}$$

From equation 1.5, it is possible to draw the voltage breakdown as a function of the product pd. This representation is called the *Paschen curve*, of which an example is shown in figure 1.5 for an argon discharge with $\gamma_{IISEE} = 0.1$.

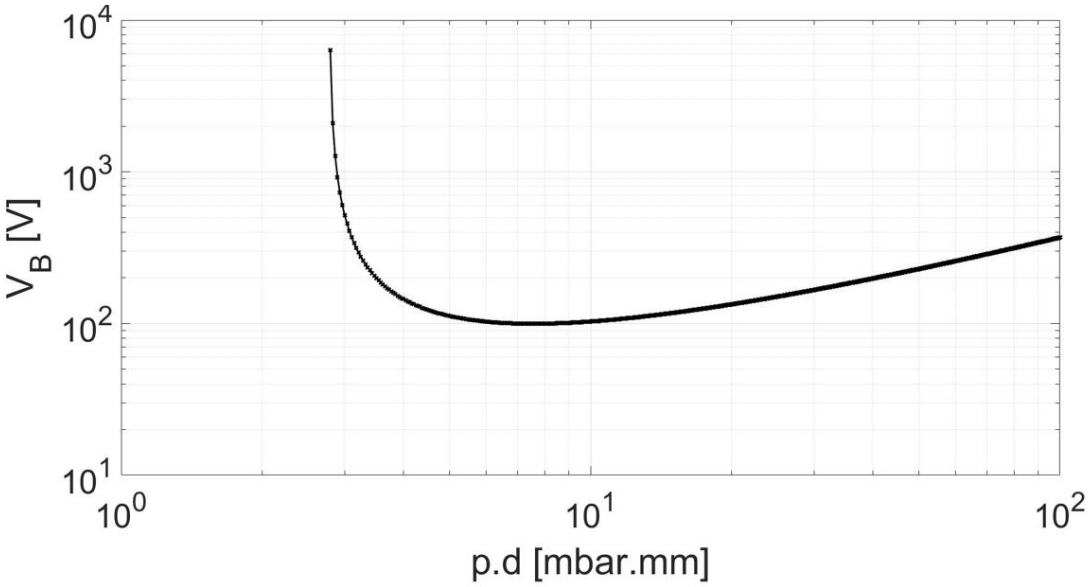

Figure 1.5 – Example of a Paschen curve for argon: breakdown voltage V_b [V] as a function of pd [mbar.mm]. Adapted from data of [14, p. 546] with $\gamma_{IISEE} = 0.1$.

At low pd, V_B increases dramatically because fewer collisions require a high ionisation probability and hence a high electric field, whereas at high pd, short ionisation mean free paths require high electric fields to reach the ionisation energy.
From equation 1.5, it can be understood that DC glow discharges depend strongly on the geometry of the electrodes (through the parallel plates approximation and the inter-electrode distance d) and on their material (through γ_{IISEE}), on the type of gas (through A, B and γ_{IISEE}) and on the working pressure. This dependence will be further analysed in chapter 2.

1.1.1.3 Plasma sheath

After describing the gas breakdown phenomena and the glow discharge characteristics, we now discuss what happens when a glow discharge plasma is confined inside a vacuum vessel and interacts with its surrounding metallic or dielectric surfaces.

As mentioned before, electrons have higher temperatures than ions (respectively T_e and T_i) in cold plasmas, and also have a lighter mass m (respectively M). It means that the electron thermal velocity $v_{the} = (eT_e/m)^{1/2}$ is much larger than the ion thermal velocity $v_{thi} = (eT_i/M)^{1/2}$. Assuming a typical ratio $T_e/T_i \simeq 10$, and $M/m \simeq 1836$ for a proton, the ratio $v_{th_e}/v_{th_i} \simeq 100$. Hence, electrons will travel to any physical element in contact with the plasma faster than ions from the bulk. This results in the formation of a thin electron-depleted layer called a plasma *sheath* around the physical elements. In this sheath, quasi-neutrality is not anymore satisfied as this layer is positively charged with respect to the physical surface potential because of ion densities being larger than electron densities. Therefore, a local electric field E directed from the plasma bulk to the wall is created, which drives electrons back into the plasma according to the electric force $-eE$. After a few Debye lengths, this electric potential is screened and the plasma bulk electric potential goes to zero.

Three main cases of physical surfaces immersed in a plasma can be found in our applications:

- A dielectric surface (such as an insulating ceramic) that cannot draw any net current. Its surface will first be negatively charged by the mobile electron flux up to the point that it repels incoming electrons and attracts positive ions, thus balancing the electron and ion fluxes and settling at the so-called *floating potential*.
- A grounded surface (such as a metallic anode) will be surrounded by a positive ion sheath, and thus will bring the plasma potential to be slightly positive with respect to the ground.
- A negatively biased surface (such as a metallic cathode) will attract positive ions and repel electrons. Its negative electric potential is screened after a few Debye lengths.

This description will be further applied to electrostatic probe diagnostics such as Langmuir probes, used to extract local plasma parameters in chapter 2.
The typical electric potential profile in the gap between two electrodes generating a DC glow discharge is shown in figure 1.6.

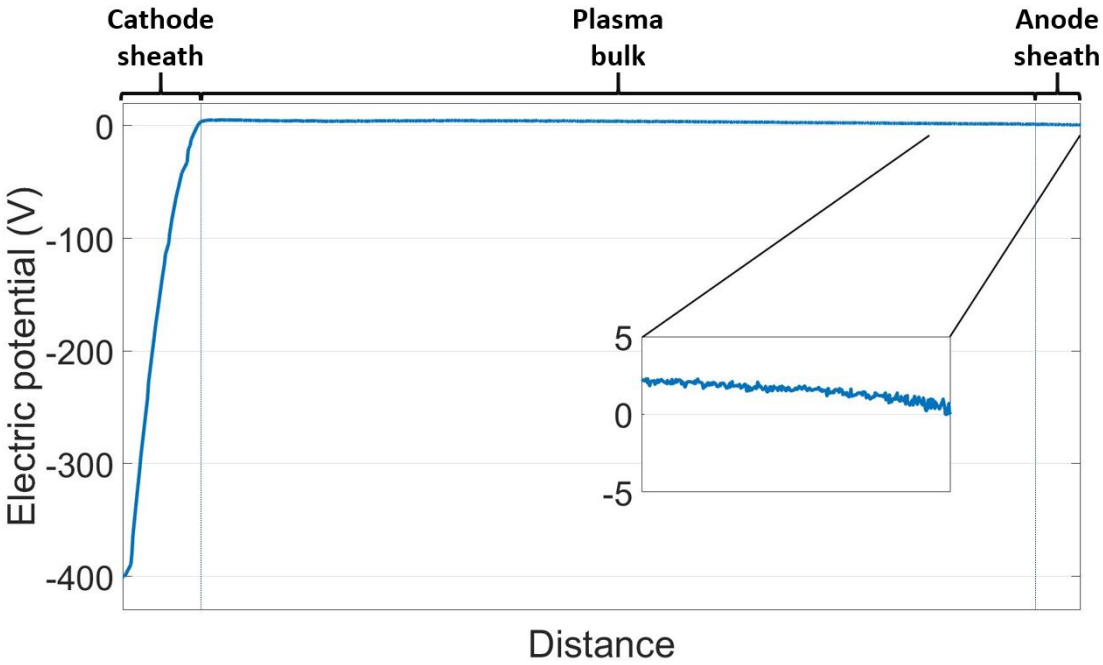

Figure 1.6 – Typical electric potential profile in a DC glow discharge between a cathode negatively biased at -400 V (left) and a grounded anode (right). The negative potential inside the cathode sheath is screened and the plasma potential is slightly positive with respect to the ground. Simulated curve taken from figure 2.11(e) at P_{Ar} = 0.3 mbar.

1.1.1.4 Ion-induced secondary electron emission

As first mentioned in section 1.1.1.2 for its impact on discharge breakdown, secondary electron emission generated by ion bombardment on the cathode is the driving mechanism which contributes to the DC glow discharge sustainability.

In the plasma bulk, electrons colliding with neutral atoms can undergo collisions involving excitation, ionization and elastic scattering processes. Secondary electrons generated at the cathode surface have the highest energy with respect to the plasma potential due to the acceleration provided in the cathode sheath. Each additional electron generated by gaseous ionisation has a lesser initial energy compared to the one of the impact electron. Thus, without supply of secondary electrons from the cathode, the ionisation cascade would eventually fade away.

This phenomenon of free electron extraction by ion bombardment of a surface is ruled by two main mechanisms called *kinetic emission* and *potential emission*:

- Kinetic emission, as its name suggests, relies on the transfer of the ion kinetic energy towards the valence electrons of a target such that electrons can be extracted into vacuum.

- Potential emission happens when the ionisation energy of the impinging ion is released upon neutralization close to the solid surface, and is sufficient to free electrons into vacuum (two-electron Auger process).

These two mechanisms were described in particular in [16, 17] and in [18, 19, 13], respectively. Kinetic emission yield is reported to dominate over potential emission at large ion velocities: a threshold of 6×10^4 m/s for argon is given in [20], corresponding to an energy of ~ 750 eV, and a linear trend with incident kinetic energy is reported up to a few hundred keV.

On the contrary, potential emission does not depend on the kinetic energy of the impinging ion, but only on its ionization energy E_i and on the work function ϕ and the Fermi energy E_F of the target. Its yield γ_{IISEE} is constant for a given ion/target material couple. Empirical formulas for potential emission yield were suggested by several authors and are summarized in [21] as follows:

$$\gamma_{IISEE} = 0.2(0.8E_i - 2\phi)/E_F \qquad [19] \qquad (1.6)$$

$$\gamma_{IISEE} = 0.032(0.78E_i - 2\phi) \qquad [16] \qquad (1.7)$$

$$\gamma_{IISEE} = 0.016(E_i - 2\phi). \qquad [13, \text{p.71}] \qquad (1.8)$$

Potential emission can only occur if $E_i > 2\phi$, and the cut-off energy of the emitted electrons spectrum is $E_i - 2\phi$. Choosing singly charged argon ions Ar^+ impinging on a niobium target as a meaningful example for our application, with $E_{i_{Ar^+}} = 15.76$ eV, $\phi_{Nb} = 4.2$ eV and $E_{F_{Nb}} = 5.32$ eV [22], equations 1.6, 1.7 and 1.8 respectively give $\gamma_{IISEE} = 0.158$, 0.125 and 0.118, with 7.36 eV as the cut-off energy of secondary emitted electrons.
In addition, the angular distribution of the secondary electrons is commonly described by a cosine law, as the memory of their collisions with the bulk atoms is forgotten when they are released from the surface.

The bias voltages used in DC glow discharges of this thesis do not exceed 1000 V[1] such that singly charged ions accelerated in the cathode sheath and bombarding its surface cannot exceed 1 keV. As such and faced with the scarcity of experimental data for ion-induced secondary electron emission below 1 keV, we chose to only consider potential emission in our study, though kinetic emission may need to be addressed for higher discharge voltages. The influence of the IISEE parameters on the accurate modelling of glow discharges will be discussed in chapter 2.

As reported in [13, section 4.7] and [23], photon and metastable atom bombardment on the cathode can play an additional role in the secondary electron emission from the cathode.

[1] Because there is little necessity for higher voltages in our applications apart from occasional need for a transient higher voltage during the plasma ignition phase, most of our DC plasma power supplies are limited to 1 kV.

We do not investigate this contribution in the present study since it would entail a growing complexity in simulation collision reaction models. Nevertheless, an experimental campaign for measuring IISEE parameters in a system featuring an ion gun is currently ongoing at CERN, though preliminary results are not presented in this work. It will help to refine the precise contribution of IISEE in the total secondary electron emission yield.

1.1.2 Physical sputtering

The phenomenon of sputtering occurring in plasma discharges was evidenced early in 1852 by W. R. Grove during his study of gas discharges in a glass vessel while varying working gases and electrode materials [24]. It consists in the ejection of atoms from a surface under energetic particle bombardment. Under collision with the cathode (target), energetic particles transfer part of their energy to atoms of the surface layers, which in turn can go through several collision cascades with neighbouring atoms and eject some of them away from the target by momentum transfer. In the present study, we assimilate these energetic bombarding particles to ions accelerated in the cathode sheath exclusively, although neutral process gas atoms can gain sufficient energy through charge transfer with ions in the sheath (see reaction 3 in table 1.2) and contribute to sputtering.
The sputtering yield $Y = \frac{\text{Number of sputtered atoms}}{\text{Number of impinging ions}}$, defined as the ratio of sputtered atoms over impinging ions, depends on the angle and energy of the incident ions.
Since Sigmund's analytic approach [25], numerical codes have been developed to compute sputtering yields (see section 1.2.3), which have also been provided by semi-empirical formulas fitting experiments such as the one of Yamamura [6]. Yamamura's formula for normal incidence ion bombardment depends on the impinging ion energy, on the surface binding energy, on the atomic numbers and masses of projectile and target elements and on some fitting parameters. It also defines a threshold energy of the impinging ion below which no sputtering occurs, depending on the surface binding energy and masses of the ion and target atoms. A Matlab script used to compute sputtering yields according to the procedure described in [6] is given in Appendix A.
In the specific case of normal incidence Ar^+ bombardment on niobium, the formula accurately fits experimental datasets gathered by Yamamura from the existing literature, and the sputtering yield is plotted as a function of ion energy in figure 1.7.

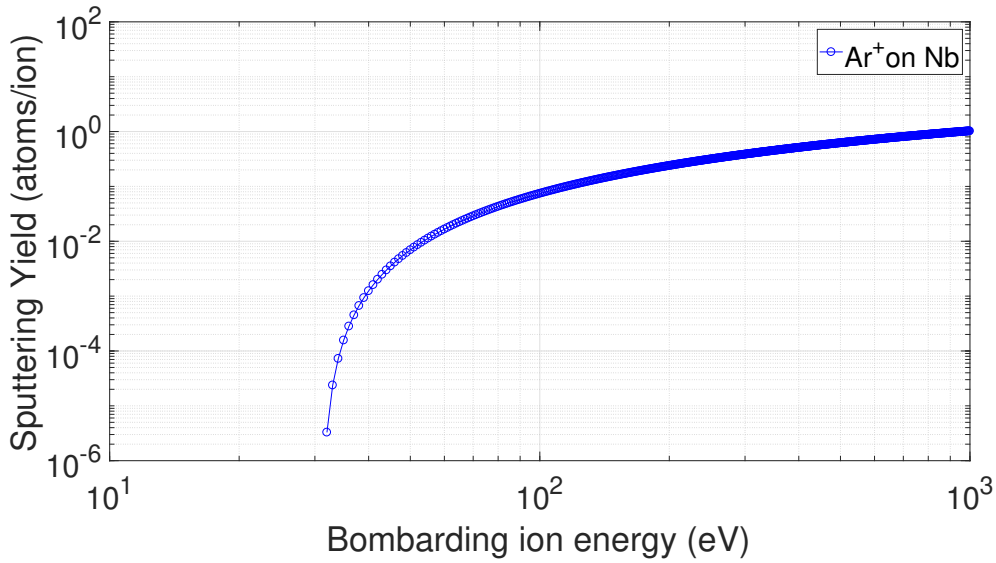

Figure 1.7 – Sputtering yield of Nb under Ar^+ bombardment based on Yamamura's formula.

We assume in the rest of this study that ions bombarding the cathode have a normal angle of incidence (i.e. 0 ° with respect to the surface normal vector) because of their strong directional acceleration through the cathode sheath, and we will therefore not consider the influence of the ion incidence angle on the sputtering yield.

The energy and angular distribution function of the sputtered particles can be written as $f(E,\theta) = f(E) \times f(\theta)$, which was derived by M.W. Thompson [26, equation 12] as :

$$f(E,\theta) \propto \frac{E}{(E+E_b)^{3-2m}} cos\theta, \tag{1.9}$$

where E is the energy of the sputtered atom, θ is its ejection angle with respect to the surface normal, E_b is the surface binding energy of the target (often assumed to be equal to its sublimation energy in eV) and m is a parameter describing the interatomic potential between surface target atoms. The parameter m is equal to 0 in the hard-sphere approximation, such that the peak of the energy distribution occurs at $E = E_b/2$. Thus, sputtered atoms have energies of a few eVs when they are emitted from the cathode ($E_{b_{Nb}} = 7.59\,eV$).

The *cosine* angular distribution means that sputtered atoms are emitted isotropically from the target. Its validity depending on incident ion energy range, target cristallinity and surface state has been discussed in [27, 28, 29, 30, 31] and concurred that for low energy ions (sub-keV), angular distributions tend to be *undercosine* or *heart-shaped*, while increasing ion energies leads to cosine or overcosine distributions. The influence of this parameter on sputtered atoms transport simulation results will be studied in section 4.2.3.
A detailed review on physical sputtering can be found in [32].

Once emitted from the cathode surface, sputtered neutral atoms experience collisions with

the process gas atoms depending on the process pressure, and form the desired thin film layer upon condensation on the substrate surface.

1.1.3 DC diode configuration

In the DC diode configuration, electrons move in straight lines along the electric field from cathode to anode. Therefore, for a given inter-electrodes gap distance d, the discharge sustainability requires relatively high voltages (i.e. low current densities at a given discharge power) and high working pressures (high 10^{-2} mbar to low 10^{-1} mbar) such that sufficient ionizing collisions with the neutral working gas atoms can occur (see the analysis of the Paschen curve displayed in figure 1.5). This technique has an obvious drawback when applied to coatings, which is that the high working pressure also induces many collisions between sputtered atoms and working gas atoms. This effect is often undesired, as most of the sputtered atoms are redeposited on the cathode after experiencing these collisions and drastically lower the deposition rates, the further the substrate is from the cathode, the lower the deposition rate is. Also, as will be discussed in 1.1.5, the few sputtered atoms that finally reach the substrate to be coated have lost most of their energy during these neutral-neutral collisions (*thermalization*), having an impact on the deposited film morphology.

1.1.4 DC magnetron configuration

To sustain the glow discharge at lower pressures more favourable to coating applications, the idea of adding a magnetic field in the DC diode discharge configuration was proposed in the early 1900's, with the goal of increasing the path of electrons between cathode and anode and thus increasing the number of ionizing collisions before electron collection on the anode. The work of Penning in the 1930's, which also led to the development of the cold cathode Penning pressure gauge [33], was extended and applied to sputter deposition in the 1960's [34, 35] with the design of the first closed-field **E**×**B** magnetron sputtering sources [2].

Several magnetron configurations have been developed over the years and rely on the application of a magnetic field parallel to the cathode surface, including the coaxial cylindrical (figure 1.8(a)) and the planar magnetron sputtering sources (figure 1.8(b)), by means of either an external solenoid or permanent magnets assemblies.

In addition to being accelerated by the electric field, electrons follow a cyclotron motion around the magnetic field lines along with a **E**×**B** drift motion, therefore moving in cycloids [37]. Compared with the diode configuration, the path of electrons is increased before their collection, which allows magnetron operation at typical pressures of $\sim 10^{-3}$ mbar for magnetic field strengths of a few hundreds Gauss.

Contrarily to electrons, ions are not confined by the magnetic field because of their large Larmor radius defined as $r_L = \frac{v_\perp}{\Omega_c} = \frac{Mv_\perp}{eB}$ where $v_\perp$ is the charged particle velocity component orthogonal to the magnetic field, Ω_c is the angular cyclotron frequency, M is the charged

[2] A historical review of thin-film sputter deposition including magnetron sputtering can be found in [36]

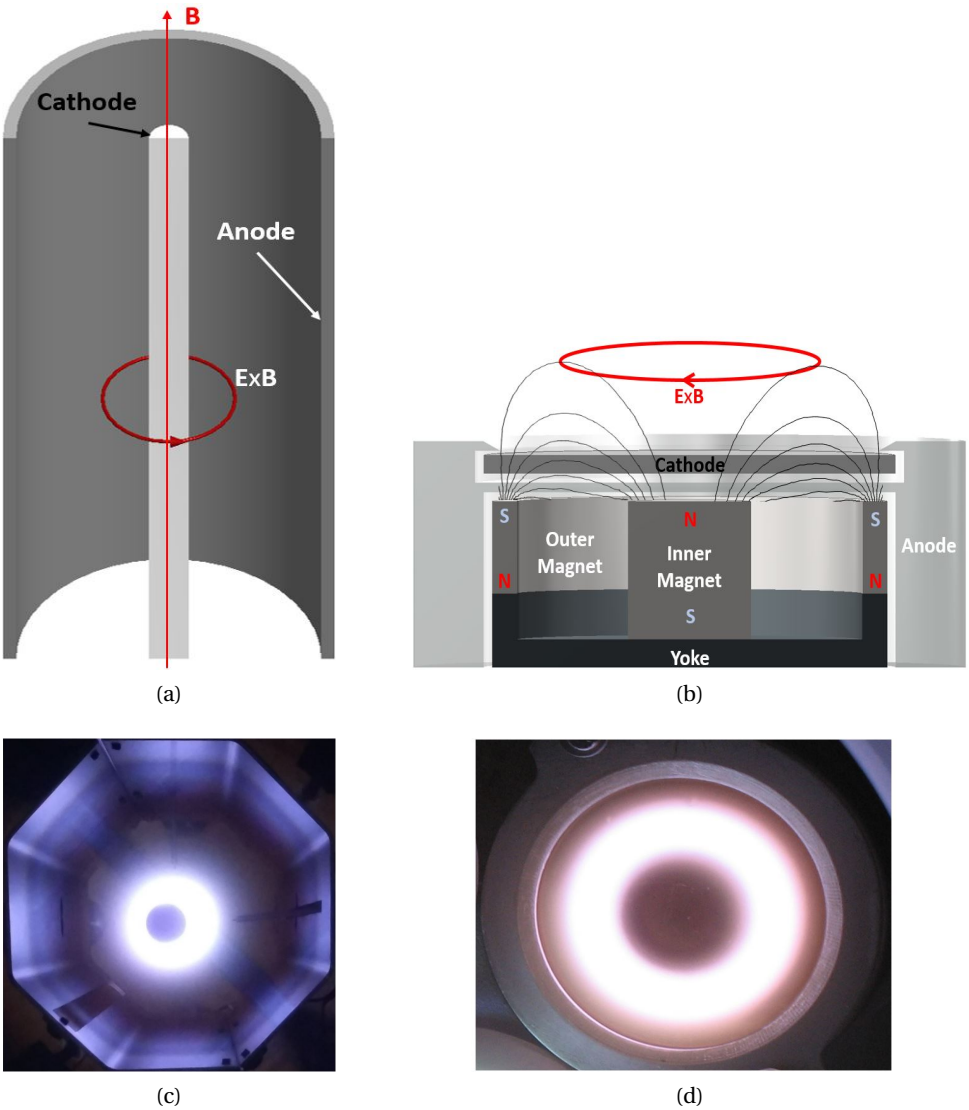

Figure 1.8 – Schematic cutviews : (a) Coaxial cylindrical magnetron and (b) Planar magnetron with magnetic flux lines overlay and **E**×**B** drift drawn in perspective; Pictures: (c) Bottom view in the coaxial configuration described in chapter 2 (d) Top view of a planar magnetron described in chapter 4.

particle mass and B the magnetic field strength. Hence, they are accelerated by the cathode sheath electric field from the plasma bulk towards the cathode which is eroded by physical sputtering as described in section 1.1.2.
In the presence of a magnetic field, secondary electrons can be recaptured by the cathode depending on their angle of emission, initial energy and first collisions with the gas atoms. Models based on *effective* secondary electron emission coefficients provide estimates for the minimum voltage necessary to sustain the discharge and can be found in [37, 38, 39].

1.1.5 From coating processes to film growth

The topic of thin film growth is vast and will not be *directly* explored in this work, apart from section 4.2 where it will be shallowly considered but without correlating thin film morphology to SRF properties. It has a huge *indirect* impact on this work though, since our practical end goal is to be able to design coating systems which can provide thin films of niobium matching the requirements of SRF cavities[40].
Indeed, our application requires that niobium films have good *adhesion*, are *dense*, *defect and impurity free*, *smooth* and with a thickness profile as *uniform* as possible such that they can provide good SRF performances. *Ideally*, each of these qualities would be met by the possibility of acting **independently** on each of the physical processes described so far. For example, adapting the cathode geometry to match a specific cavity shape could improve thickness uniformity. Using a DC diode or a DC magnetron configuration could impact the efficiency of sputtered atoms transport through their different working pressure ranges, also helping with the uniformity of film thickness. Tuning the energy of the condensed sputtered atoms as well as bringing ion flux bombardment towards the substrate would enhance atom surface mobility during film growth, and hence help with film smoothness and density [41][42]. Reducing the angle of incidence of impinging sputtered atoms could suppress self-shadowing and push towards compact and defect-free layers.
In the real picture, although these examples are of precious help as first-order principles when designing or understanding coating systems, they are very often entangled and have to be considered as a whole[3]. For instance, cathode geometry driven by space constraints of a given cavity will often limit the available choices in terms of plasma operation and working pressures, thus directly impacting sputtered atoms transport and in turn film growth.
This complexity justifies the necessity of dedicating time and efforts on the R&D phase for each new cavity project, to ensure that each step can be validated or modified according to its specific requirements.
Therefore, the use of simulation tools is justified in order to get as much insight as possible on the physical processes, thus aiming at accelerating and optimising the design of each coating system.

1.1.6 Tools for thin film analysis

In this section, we describe two techniques available at CERN with their respective instruments used in this work for thin film analysis : X-Ray fluorescence (XRF) for thin film thickness measurements and Focused Ion Beam coupled with Scanning Electron Microscopy (FIB/SEM) for cross-sectional imaging of thin film layers.

[3] A source of relief regards the requirements in terms of adhesion and absence of contamination of the grown layers. Since the production of the LEP cavities in the 1980's, tremendous efforts have been made in terms of cavity preparation: mechanical and chemical surface polishing, clean room assembly, ultra-high vacuum procedures have indeed become standards when dealing with coatings for SRF cavities.

1.1.6.1 X-Ray fluorescence

X-Ray fluorescence can be used to measure thicknesses of thin film layers coated on specific substrates. The XRF measurement method relies on the excitation of atomic species in a sample by an external X-ray source. Excited core electron shells can in turn emit element-specific X-ray lines, in the present case both from the film and from the substrate. The source irradiates an area of ~ 0.4 mm radius on the sample. From the intensity of both substrate and thin film lines and by taking into account attenuation and secondary fluorescence effects, the concentrations of their respective elements and/or the film thickness can be extracted.
The instrument used at CERN is a Helmut Fischer GmbH Fischerscope® X-Ray XDAL® -T9 operated with the WinFTM® control and measurement software[43]. Its range of measurable elements spans from aluminium (Z = 13) to uranium (Z = 92). In this work, we will use the routine for thickness measurements of niobium thin films coated on copper substrates, along with the one for niobium coatings on stainless steel samples in chapter 3. Both routines are calibrated independently on bulk samples of the different materials. The practical interest of this instrument is that large samples can be analysed in a fast and pre-programmed systematic way, such that thin film thickness profiles on coated samples of large scales (up to a length of ~ 0.5 m) can be extracted. Its main drawback for the present study is that it does not account for thin film layer porosity, as it relies on the comparison of relative energy peaks signals of the irradiated substrate and thin film layer.

1.1.6.2 Scanning Electron Microscopy coupled with Focused Ion Beam

The second instrument of choice for thin film analysis at CERN is a Zeiss Crossbeam 540 Field Emission Scanning Electron Microscope (SEM) featuring a Gemini® II electron optical column [44]. This Scanning Electron Microscope also features a combined Focused Ion Beam column with a gallium liquid metal ion source, such that samples can be locally coated with a protective platinum layer, milled with the FIB ion source and imaged with the SEM *in situ* and perpendicularly to the milling direction, as seen in figure 1.9. Thus, FIB/SEM combination enables to obtain a material cross section in vacuum while avoiding contamination or oxidation of the milled region between the steps of FIB milling and SEM imaging of the sample.

As it will be discussed in section 4.2.4.3, the FIB/SEM method presents the advantage for thin film analysis of directly imaging the coated layer on top of its substrate, and as such can provide direct information in terms of thin film thickness and morphology. The image contrast is obtained in SEM mode by the different secondary emission yields of the film and substrate materials, and in a less pronounced way by the grain orientation. It can also be produced in ion beam imaging mode by the ion-induced electron yield. In some cases (strong difference between the atomic number of materials), a marked contrast can also be obtained from elastically backscattered electrons.
The main disadvantage of this technique stems from its locality of measurement, with typical size of ~ a few tens of μm, which prevents its use for thin film thickness profile extraction on large samples with a local resolution.

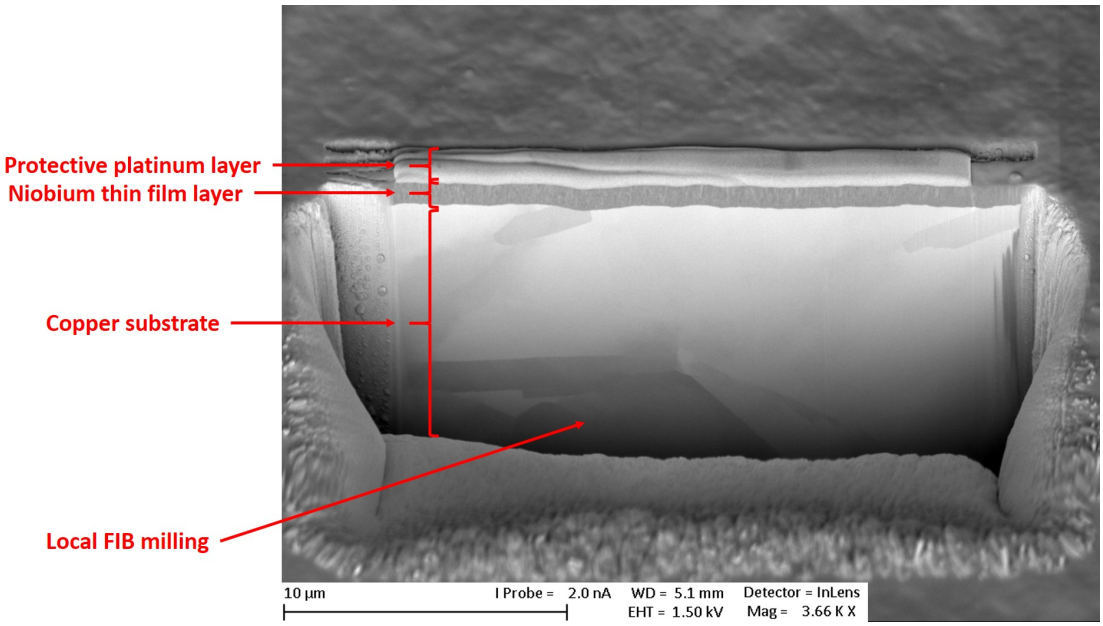

Figure 1.9 – Example of a copper sample coated with a niobium thin film, coated *in situ* with a protective platinum layer, milled with FIB and imaged with SEM.

1.1.6.3 Comparison of thin film thicknesses measured by XRF and FIB/SEM

As discussed before, FIB/SEM imaging provides accurate local measurement of thin film thickness and morphology. Therefore, FIB/SEM measurements of local thin film thicknesses are taken as the reference. However, they cannot be systematically used to extract thickness profiles on large samples, and for this purpose we use XRF measurements. It is quite difficult to give an absolute instrumental error for the XRF measurement technique, as it depends on the local thickness range, on the calibration history of the instrument for the thin film/substrate pair, on the time of sample irradiation and on the spot size, on the accuracy of X-Ray focus, for example. Thus, to bridge the gap between local FIB/SEM measurements of thicknesses and XRF measurements at a global scale, we estimate the XRF measurement uncertainty by comparing dense niobium-on-copper thin film thicknesses from different samples analysed at CERN in the recent years both by FIB/SEM and XRF methods. This comparison is presented in figure 1.10(a), while figure 1.10(b) shows the relative errors of these XRF measurements compared with the FIB/SEM thicknesses taken as reference.

In figure 1.10(a), it can be seen that XRF thickness measurements follow a linear trend with FIB/SEM measurements in the [600; 3200] nm range. Figure 1.10(b) shows that XRF errors are within ± 10 % of the FIB/SEM measurements, with a general tendency to underestimate FIB/SEM thicknesses. Because of the respective features of the two techniques, we will use XRF measurements when thickness profiles on large samples are needed as reference for comparison with simulated profiles, and we will use FIB/SEM measurements in section 4.2.4.3 when local measurements are required for comparison of thin film morphology with

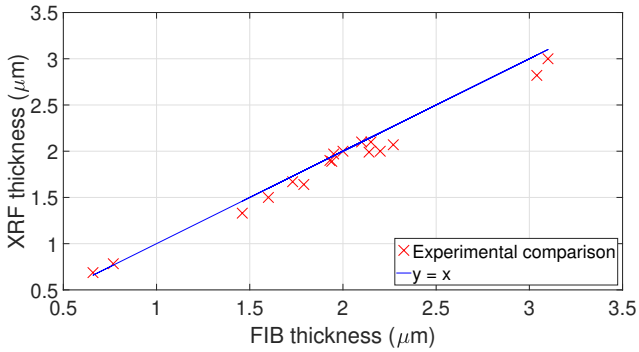

(a)

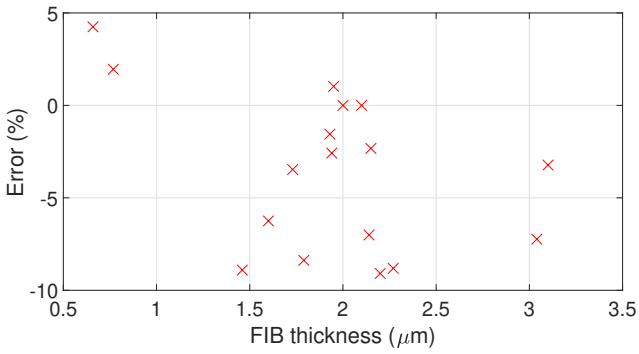

(b)

Figure 1.10 – (a) Comparison of Nb/Cu thickness [μm] measured by XRF as a function of corresponding reference FIB/SEM thicknesses on various samples coated at CERN (red crosses), plotted along with the y = x straight line (blue) (b) Relative error of XRF measurements with respect to FIB/SEM ones [%].

simulations.

1.2 Simulation tools

We introduce in this section the simulation tools used in this thesis to model DC plasma glow discharges and neutral sputtered atoms transport towards our substrates, accordingly to the workflow described in figure 1. These simulations rely respectively on the Particle-in-Cell Monte Carlo (PICMC) and the Direct Simulation Monte Carlo (DSMC) modules of a numerical code developed at the Fraunhofer Institute for Surface Engineering and Thin Films IST [4][4].

1.2.1 Introduction

Several methods can be used for plasma modelling, and the choice of one rather than another depends on which kind of plasma one has to deal with, on what level of accuracy is desired and on which phenomena and *outputs* are of interest.
When studying low pressure non-equilibrium plasmas such as the ones found in *glow discharges*, *fluid* models which treat the plasma as a continuum are not appropriate since they rely on the assumption of a local thermal equilibrium, meaning that the electron energy distribution function (EEDF) is considered as Maxwellian. Although this assumption can be in fact close to reality in the plasma bulk provided that the high energy tail of the EEDF is neglected, it loses its validity when plasma sheaths are to be described accurately. Also, magnetron sputtering operation usually occurs at pressures too low to be tackled by fluid models, as mean free paths of atoms are often of the order of or larger than the typical system dimensions, corresponding to the transition flow regime[5].

For these reasons and as we are interested in modelling glow discharges *ab initio* from plasma ignition to steady-state and sputtered atoms transport self-consistently and quantitatively, a commercial simulation code developed at the Fraunhofer Institute for Surface Engineering and Thin Films IST has been selected [4, 46, 47, 48]. It relies on the Particle-in-Cell Monte Carlo (PIC-MC) method for plasma modelling, and the Direct Simulation Monte Carlo (DSMC) method for neutral gas flow simulations.

[4] Detailed practical information on the PICMC code used in this work can be found in [45]

[5] Loosely defined as the region in which the Knudsen number $K_n = \frac{\lambda}{L} \in [0.001; 1]$, where L is a typical system dimension and λ is the mean free path $\lambda = \frac{k_B * T}{\sqrt{2}\pi d^2 p}$, with d the diameter of the gas particles [m] and p the pressure [Pa]. For argon, with typical pressures of [0.1; 10] Pa, $\lambda \in [0.6; 60]$ mm.

1.2.2 Particle-in-Cell Monte Carlo plasma simulations

1.2.2.1 Introduction

Particles in the plasma can be represented in the six-dimensional phase-space ($\mathbf{r}$, $\mathbf{v}$) of positions $\mathbf{r}$ and velocities $\mathbf{v}$ by the concept of distribution function $f(\mathbf{r}, \mathbf{v}, t)$, with the following description:

$$\mathrm{d}N = f(\mathbf{r}, \mathbf{v}, t)\mathrm{d}^3\mathbf{r}\mathrm{d}^3\mathbf{v}, \tag{1.10}$$

where $\mathrm{d}N$ is the number of particles whose positions are in the volume element $\mathrm{d}^3\mathbf{r}$ about $\mathbf{r}$ and whose velocities are in the velocity space element $\mathrm{d}^3\mathbf{v}$ about $\mathbf{v}$, at a given time t.
When balancing the number of particles entering or going out of the phase-space volume element $\mathrm{d}^3\mathbf{r}\mathrm{d}^3\mathbf{v}$ during a time interval dt, either because of their drift or under the influence of macroscopic forces $\mathbf{F}$, the Boltzmann equation is obtained (see for instance [14, p. 28]), and can be written as:

$$\frac{\partial f}{\partial t} + \mathbf{v} \cdot \nabla_{\mathbf{r}} f + \frac{\mathbf{F}}{m} \cdot \nabla_{\mathbf{v}} f = \left.\frac{\partial f}{\partial t}\right|_{coll}, \tag{1.11}$$

where ∇ is the gradient operator, $\cdot$ is the dot product, and in Cartesian coordinates $\nabla_{\mathbf{r}} = \mathbf{e}_x \partial/\partial x + \mathbf{e}_y \partial/\partial y + \mathbf{e}_z \partial/\partial z$, and $\nabla_{\mathbf{v}} = \mathbf{e}_x \partial/\partial v_x + \mathbf{e}_y \partial/\partial v_y + \mathbf{e}_z \partial/\partial v_z$, m is the particle mass, and the right-hand term $\left.\frac{\partial f}{\partial t}\right|_{coll}$ represents the collisions between species.

Fluid numerical codes do not solve directly equation 1.11, but rather consider *moments* of the Boltzmann equation to solve the particle, momentum and energy conservation equations, while a *closure* relation has to be assumed. This relation usually postulates that species are in thermal equilibrium such that their velocities can be described with Maxwellian distributions.

Instead of considering the plasma as a macroscopic continuum, the Particle-in-Cell (PIC) method [49, 50, 51] describes it as a large number of *numerical* particles (often referred to as *superparticles*), each of them representing a number of physical *real* particles but treated by the code as a single one. Therefore, the PIC method solves the Boltzmann equation by assimilating the distribution functions of particles (see equation 1.10) to a large number of statistically representative *superparticles* inside each phase-space volume element.

The simulation domain is divided into Cartesian cells representing elementary space volumes of dimensions $\Delta x * \Delta y * \Delta z$. A typical time cycle of the PIC method is shown in figure 1.11.

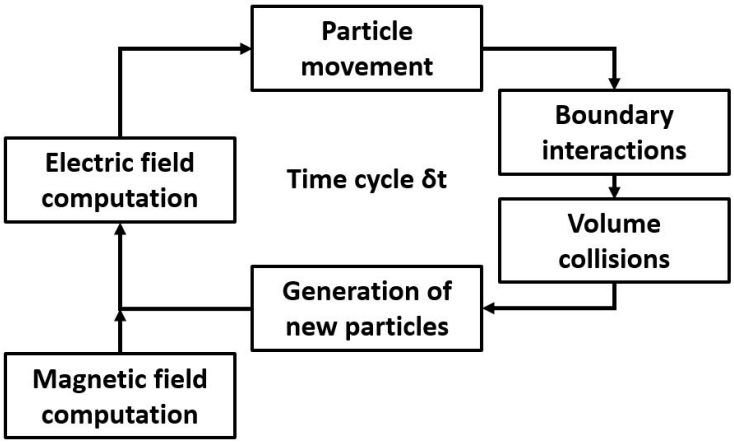

Figure 1.11 – Description of a PICMC typical time cycle.

The electric field is first computed on the nodes of each cell based on the charged particles densities within its volume by solving the Poisson equation. Each superparticle is then *pushed* based on the computed electromagnetic field by solving the equations of particle motion. Pushed particles can either interact with physical surfaces (boundaries) or with other particles, which in turn induces changes of particle densities within each cell. The Monte Carlo (MC) technique is used to handle collisions between particles (right-hand side of the Boltzmann equation 1.11) as stochastic rather than deterministic events. A time loop through these steps provides a self-consistent description of the plasma, as particles are tracked in *continuous* phase space while *macro-quantities* such as particle densities or fields are computed at discrete positions (respectively cell centres and cell nodes).

The application of the PICMC technique to real cases can be challenging because of computing power limitations along with long simulation times required for a valid plasma description. Yet, the very recent *democratisation* of High Performance Computing (HPC) clusters along with the development of parallel computing code implementations have greatly expanded the horizons of applications for PICMC codes such as the one used in this work.

The chosen PICMC code is therefore suited for the simulation of non-equilibrium glow discharge plasmas, provided that each physical phenomenon described in section 1.1 is accurately modelled, and that corresponding physical parameters are correctly input.

1.2.2.2 Numerical constraints

As PIC simulations rely on time and space discretisation of equations, several numerical constraints on the time step and cell dimensions are inherent to the numerical schemes used to solve these equations. Analytical criteria of stability constraining numerical parameters with respect to typical plasma characteristics have been derived [50, 52], and can be applied to the PIC code used here:

$$\Delta t \leq 0.2\omega_{pe}^{-1} = 0.2\sqrt{\frac{m\epsilon_0}{n_e e^2}} \qquad \text{where} \quad \Delta t \quad \text{is the simulation time step} \tag{1.12}$$

$$\Delta x \leq 3.4\lambda_D = 3.4\sqrt{\frac{\epsilon_0 \mathrm{T}_e}{e n_e}} \qquad \text{where} \quad \Delta x \quad \text{is the simulation mesh size.} \tag{1.13}$$

Equation 1.12 defines a maximum simulation time step Δt to resolve plasma density oscillations of typical frequency $\mathrm{f}_{pe} = \omega_{pe}/2\pi$, where $\omega_{pe} = \left(\frac{n_e e^2}{m\epsilon_0}\right)^{1/2}$. Equation 1.13 defines a maximum simulation spatial resolution Δx to resolve the typical plasma quantities (electric field, densities...) at the scale of the Debye length. This is particularly important to properly model the cathode sheath, as density and field gradients are especially large in this region.
When a magnetic field is present, the angular plasma frequency ω_{pe} also has to be replaced by the cyclotron frequency Ω_c in equation 1.12 to provide an additional constraint such that gyrokinetic electron trajectories are well resolved. Typical time steps values Δt can be found in table 1.1 as a function of plasma density n_e [m^{-3}] and magnetic field strength B [gauss].

Table 1.1 – Examples of required maximum simulation time steps Δt depending on plasma density n_e [m^{-3}] and magnetic field strength B [gauss].

n_e [m^{-3}]	$\Delta t = 0.2\omega_{pe}^{-1}$ [s]	B [gauss]	$\Delta t = 0.2\Omega_C^{-1}$ [s]
10^{13}	1.1211×10^{-9}	100	1.1371×10^{-10}
10^{14}	3.5452×10^{-10}	200	5.6856×10^{-11}
10^{15}	1.1211×10^{-10}	300	3.7904×10^{-11}
10^{16}	3.5452×10^{-11}	400	2.8428×10^{-11}
10^{17}	1.1211×10^{-11}	500	2.2742×10^{-11}

These numerical constraints induce obvious consequences on the feasibility of simulations. Indeed, very small time steps result in large computation times required to achieve relevant physical time spans, and can be excessively large. While also adding to the computation time, very small mesh sizes induce large memory loads which can be challenging for the computational infrastructure, especially in the case of large space domains required in 3D simulations of SRF cavity coatings.

As an example, for $n_e = 10^{15}\,m^{-3}$ and $T_e = 3\,eV$ typically found in glow discharge plasmas, equation 1.13 implies $\Delta x \leq 1.4$ mm. If a simulation volume of $1\,m \times 0.2\,m \times 0.2\,m = 4.10^{-2}\,m^{-3}$ is discretised with a regular 3D Cartesian mesh of $\Delta x = \Delta y = \Delta z = 1.4$ mm, the number of cells in the simulation is of $\simeq 15$ millions. Increasing the density to $n_e = 10^{17}\,m^{-3}$ while keeping the electron temperature unchanged would result in $\Delta x \leq 0.14$ mm, and the simulation volume now contains 15 billion cells. This is excessively large even for a parallel computing code running on a HPC cluster such as the one described in section 1.2.4, because the global computation time includes equation solving at the level of each cell, and because the computer memory needed to store the information about particles and fields at the cell resolution is not sustainable.
Failing to satisfy the spatial numerical constraint of equation 1.13 can lead to *numerical heating* of electrons, meaning that insufficient spatial resolution of the electric field can induce artificially high electron kinetic energies [53] up to the extreme point of simulation divergence. The influence of these constraints on simulation results will be discussed in chapter 2, section 2.3.

Two other numerical constraints are inherent to the handling of collisions by the Monte Carlo method. First, to properly evaluate collisions, *cell hopping* should not happen such that particles have to stay within the same grid cell for at least one time step. This requires:

$$\Delta t \times v < \Delta x, \tag{1.14}$$

where v is the particle velocity. To evaluate the *worst case scenario* corresponding to the minimum Δx below which *cell hopping* could occur, we can choose the smallest value of Δt from table 1.1, i.e. $\Delta t = 1 \times 10^{-11}\,s$. Likewise, the worst case scenario regarding particle velocities is the one of electrons of high kinetic energies when accelerated through the cathode sheath. Considering that their highest velocity would be $v = \sqrt{\frac{2qU}{m}}$ if neglecting the energy loss due to collisions, and taking $U = 1000\,V$ as the largest voltage of typical power supplies, we obtain $v = 1.9 \times 10^7\,m.s^{-1}$, which requires $\Delta x > 0.19$ mm. This constraint is therefore not too difficult to satisfy, as we will usually use smaller time steps in simulations ($5 \times 10^{-12}\,s$), and as we try to keep larger cell sizes (~ 0.5 to 1 mm depending on the model) for viability of computational load.

The second constraint requires that a minimum number of neutral and charged superparticles is present within each simulation cell, such that inter-species collisions are accurately computed.
This constraint relies on the concept of *scale factor* N_{scale}, which can be written within each cell as :

$$N_{scale} = \frac{\text{Number of real physical particles per cell } N_{physical}}{\text{Number of numerical superparticles per cell } N_{numerical}}. \tag{1.15}$$

By using the *ideal gas law* for neutral process gas atoms:

$$pV = N_{physical} k_B T, \tag{1.16}$$

equation 1.15 can be expressed as:

$$N_{scale} = \frac{pV}{N_{numerical} k_B T}, \tag{1.17}$$

where p [Pa] is the process gas pressure, V [m^3] is the cell volume, k$_B$ is the Boltzmann constant (k$_B$ = 1.3807x10^{-23} [J/K]) and T [K] is the gas temperature .

For charged particles, using $N_{physical} = nV$ with n [m^{-3}] being the charged particle density and V [m^3] the cell volume, equation 1.15 is modified into:

$$N_{scale} = \frac{nV}{N_{numerical}}. \tag{1.18}$$

A good practice is to have $N_{numerical} \sim 10$ to 20 within each cell [45], such that scale factors for neutrals and charged particles can be chosen accordingly to the process gas pressure p, to the cell volume V and to the expected charged particle densities n.

1.2.2.3 Volume reactions

Volume reactions used in argon plasma simulations are described in table 1.2, with their respective cross-sections plotted in figure 1.12.

Table 1.2 – Set of volume reactions used in argon plasma modelling.

Reaction	Type	Reference
1. $Ar + Ar \rightarrow Ar + Ar$	Momentum Transfer	[54, p. 408]
2. $Ar^+ + Ar \rightarrow Ar^+ + Ar$	Momentum Transfer	[55, 56, 57]
3. $Ar^+ (fast) + Ar (slow) \rightarrow Ar (fast) + Ar^+ (slow)$	Charge Transfer	[55, 56, 57]
4. $e + Ar \rightarrow e + Ar$	Elastic Momentum Transfer	[23, eq. B5]
5. $e + Ar \rightarrow e + Ar^*$	Total Excitation	[23, eq. B6]
6. $e + Ar \rightarrow 2e + Ar^+$	Ionization	[23, eq. B7]

When a plasma simulation involving argon neutrals, argon ions and electrons is initialised, the reactions listed in table 1.2, which are part of a larger library, are selected. The full library of reactions can be user-customised, such that new species or reactions can be added. This is not done in the present work because argon discharge reactions are well documented, but could be explored in the future for other process gases.

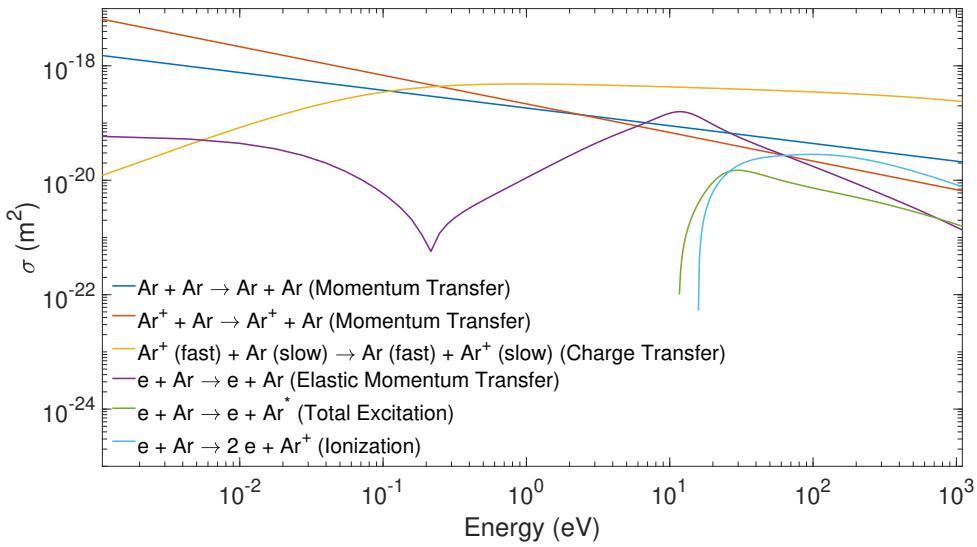

Figure 1.12 – Summary of volume reactions cross sections [m^2] used in argon plasma modelling.

1.2.2.4 Workflow of a typical plasma simulation

To start a new simulation, its geometrical model corresponding to the real coating system first has to be designed. This can be done with any Computer-Aided Design (CAD) software able to export models as *.step* files, as can be seen in figure 1.13(b), or directly within the open source software GMSH for simple cases [58]. Once the geometry is loaded in GMSH, surfaces of the model are then selected and grouped according to the physical element they belong to, e.g. cathode, anode or cavity. A 2D surface mesh representing these physical elements in the plasma simulation is generated, such as seen in figure 1.13(c). Figure 1.13 shows that only surfaces in contact with the vacuum side (or vacuum volume in which the plasma is contained) are of interest and should be accurately modelled. Via a script command, the geometric mesh file is analysed and a parameter file template adapted to the mesh geometry is created. This file has to be modified according to the desired simulation parameters[6]. These parameters include time step Δt, total physical time to be simulated, discharge power setpoint[7], species involved in the simulation with their respective initial densities and scale factors, subvolume division for optimized parallel computing and cell division defining mesh sizes in the XYZ Cartesian frame. In the present study, we always start simulations with an initial density of seeding charged particles uniform in the simulation volume.
For each physical surface defined in GMSH, either a bias voltage for a conductor or a relative dielectric permittivity for a floating element have to be specified.
Surface reactions occurring on each element also have to be declared, such as ion-induced

[6]A detailed description of a typical parameter file can be found in [45].
[7]A discharge current or voltage setpoint can be specified instead, but we only use the power setpoint as it is done experimentally with DC power supplies.

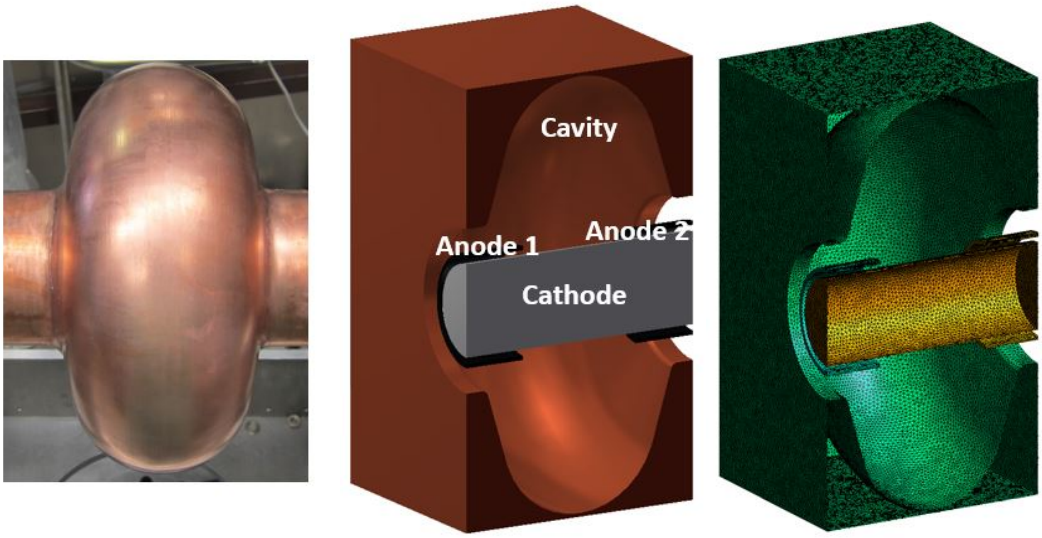

(a) (b) (c)

Figure 1.13 – Geometry modelling process of a real cavity: (a) Picture of a 1.3 GHz elliptical cavity used for R&D (b) Half-section CAD view with cathode and anodes assembly as designed with Autodesk Inventor Professional 2015 (c) Half-section view of the 2D surface mesh as generated with GMSH. More details on the study of this model can be found in chapter 4, section 4.2.

secondary electron emission (see section 1.1.1.4) or species collection. They require the respective yields, energy and angular distributions of the secondary emitted species. We will assume in our simulations that electrons impinging on any physical surface have a capture probability of 100 %, and we will neglect secondary electron emission under electron bombardment.
If a magnetic field is required, it can either be imported from an external text file (see section 2.2.4) or computed by a module of the simulation tool using the Boundary Element Method (BEM), provided that the geometrical model of the magnet assembly, the relative permeabilities and magnetic remanences of its elements are supplied (see for instance section 3.1.2). The plasma simulation is then launched on the Linux HPC cluster described in section 1.2.4 by specifying the number of processes required for parallel computing. This number of parallel processes cannot exceed the number of simulation geometrical subvolumes, and we will always use as many computing cores as the number of simulation subvolumes to optimise the parallel computing efficiency.

1.2.2.5 Plasma simulation outputs

During a simulation run, output files are written at regular time steps according to the parameter file specifications [8]. They can include 3D data of density, pressure, temperature, energy and

[8] See reference [45] for detailed information

velocity of species, and electromagnetic fields resolved at the cell scale. Data of collection or emission (e.g. sputtering) of species can also be recorded at the intersection of the 2D meshed surfaces with each cell.
When using the discharge power control option, an internal feedback process is regulating the cathode voltage based on the instantaneous discharge power, such that the setpoint value is achieved and maintained. Cathode voltage and currents flowing to each physical surface are also recorded, and are used to assess if a simulation has reached a steady state.
Special virtual surfaces called *membranes* can also be included in the simulation model such that energy and angular distributions of particles flowing through them are recorded.
All these outputs are written either as text files, or as GMSH compatible files (*.pos*). The latter can be plainly opened in GMSH or post-processed using a module of the simulation code (RIG-VM) which enables data extraction on geometrical entities such as lines, planes or cylinders, combination of different output physical parameters[9], or compilation of parameters over several time steps.

1.2.3 Direct Simulation Monte Carlo simulations of neutral atoms transport

1.2.3.1 Introduction

The Direct Simulation Monte Carlo (DSMC) module, similarly to the PICMC module, solves the Boltzmann equation but with a restriction to neutral particles. Therefore the Lorentz force term $\mathbf{F}_{Lorentz}$ disappears in equation 1.11.
As we are interested in modelling the transport of neutral niobium atoms sputtered from the cathode and moving towards the substrate, we assume that PICMC plasma simulations and DSMC simulations can be decoupled in the following way: modelling of charged particles in the plasma is used to extract the quantitative niobium sputtering profile from PICMC simulations, while DSMC simulations take this profile as input and only model the transport of neutral species. It means that ionisation of neutral niobium atoms is neglected due to the low ionisation degree of typical glow discharges and to the low densities of sputtered niobium atoms in the plasma compared to those of argon process gas atoms. The decoupling of PICMC and DSMC simulations is needed because typical time scales for plasma modelling are much smaller than the ones for neutral atom transport. Indeed, while a plasma simulation can reach a steady state within a few tens of microseconds, stabilisation of neutral sputtered atoms fluxes on the physical surfaces usually requires a few milliseconds of DSMC computation due to the low energy of sputtered atoms (a few eV, see section 1.1.2), depending on the process pressure and the collisions with gas atoms, and on the distance from cathode to substrate. Such times would be impossible to reach with PICMC simulations.

In the following sections, we first introduce the typical inputs required for DSMC simulations including definition of neutral species with their volume collision reactions, quantitative sputtering profile on the cathode as a source of sputtered particles and numerical time-

[9] For instance, velocity and density of particles can be combined to create 3D flux data

constraints related to the Monte Carlo method. Then, we describe the outputs of interest for the present study such as deposition profiles on physical elements and energy/angular distributions of deposited atoms.

1.2.3.2 DSMC module inputs

Similarly to the PICMC module, DSMC simulations require the definition of species, in our case argon and niobium, with their respective volume collision reactions as inputs. With the introduction of niobium as a species of interest colliding with argon process gas atoms and the disappearance of charged particles, DSMC simulations only keep reaction 1 from table 1.2, which describes momentum transfer between neutral argon atoms. In addition, niobium-argon and niobium-niobium interatomic collisions are described with a Born-Mayer potential V(r) following the expression given in [59]:

$$V(r) = (A_1 A_2)^{0.5} \exp\left[-\left(\frac{b_1 + b_2}{2}\right) r\right], \tag{1.19}$$

where r is the internuclear separation, A_i and b_i are Born-Mayer parameters for atoms of niobium and argon given in [59]. The Monte Carlo method using the Born-Mayer potential V(r) of equation 1.19 to compute interatomic collisions has been described in [60].

Transport simulations using the DSMC module can be run as standalones or as the logical step following a plasma simulation. In the former case, an arbitrary sputtering profile has to be defined at the cathode surface while in the latter, outputs from the plasma simulation are directly defining the sputtering profile [atoms/m^2/s]. To do so, a surface reaction modelling sputtering under ion bombardment is introduced in the plasma simulation, such that the sputtering profile computed in the plasma simulation becomes a direct input for the DSMC module. The formula chosen to model physical sputtering is the one derived by Yamamura (see section 1.1.2, figure 1.7), which links sputtering yields for different ion-target elements to the normal-incidence bombarding ion energy. The Matlab script giving the sputtering yield expression used in the plasma simulation is listed in Appendix A. This formula is preferred to other physical sputtering modelling tools such as SRIM, SDTrimSP or TRIDYN [61], because it does not require assumptions on target voltage and subsequent bombarding ion energy, and thus derives quantitative and self-consistent spatially-resolved sputtering profiles based on bombarding ion fluxes simulated by the PICMC module. For cases beyond this thesis work such as non-normal incidence ion bombardment or compound targets, the chosen approach would have to be reconsidered and modified.
The energy and angular distributions of sputtered atoms are user-defined such that they match the theory presented in section 1.1.2. A Thompson energy distribution is usually chosen (equation 1.9 with $m = 0$), and the angular distribution can be defined as power cosine or heart-shaped. Aside from sputtering source definition, other physical surfaces are defined as collecting all sputtered atoms impinging on them (*sticking factor* = 1).

In DSMC simulations, we usually keep the same cell resolution as in their corresponding prior PICMC simulations, such that deposition profile data is spatially well resolved. As was discussed in section 1.2.2.2, cell hopping has to be avoided for proper collision handling by the Monte Carlo method. By considering niobium neutral atoms of energy E = 10 eV, of mass M = 1.542x10^{-25} kg, and a typical mesh size Δx = 1 mm, the non-cell hopping constraint $\Delta t \times v < \Delta x$ requires in this worst case scenario that Δt < 2.2x10^{-7} s. In the DSMC simulations presented in this work, we will therefore choose Δt = 1x10^{-7} s.

1.2.3.3 DSMC module outputs

DSMC simulations share common output types with PICMC simulations, but applied to neutral particles. The first most interesting output for our applications is the *deposition* flux profile of sputtered particles [atoms/m^2/s] onto the substrate, since it can be converted to an estimated deposition rate profile. This conversion is given for niobium thin film deposition in equation 1.20:

$$\begin{aligned}
\text{Deposition flux}\,[atoms/m^2/s] &= \frac{\text{Number of deposited Nb atoms}}{\text{Surface}\,[m^2] \times \text{Deposition time}\,[s]} \\
&= \frac{\rho_{Nb}\,[g/m^3] \times N_A \times \text{Volume}\,[m^3]}{M_{Nb}\,[g/mol] \times \text{Surface}\,[m^2] \times \text{Deposition Time}\,[s]} \\
&= \frac{\rho_{Nb} N_A}{M_{Nb}} \times \text{Deposition rate}\,[m/s] \\
\Rightarrow \text{Deposition rate}\,[m/s] &= \frac{M_{Nb}}{\rho_{Nb} N_A} \times \text{Deposition flux}\,[atoms/m^2/s] \\
&= 1.8002 \times 10^{-29} \times \text{Deposition flux}\,[atoms/m^2/s],
\end{aligned}$$

where $\rho_{Nb} = 8.57 \times 10^6\,[g/m^3]$ is the niobium density, $M_{Nb} = 92.9064\,[g/mol]$ is the niobium molar mass [10] and $N_A = 6.022 \times 10^{23}$ [molecules/mol] is the Avogadro number.

In more practical units:

$$\text{Deposition rate}\,[\mu m/s] = 1.8002 \times 10^{-23} \times \text{Deposition flux}\,[atoms/m^2/s]. \tag{1.20}$$

Equation 1.20 assumes that grown thin films have the density of their bulk material which is not necessarily the case for porous films, as will be discussed in section 4.2.4.3.
The second most interesting output can be provided if virtual sampling surfaces (*membranes*) are used in the model. In this case, energy and angular distributions of sputtered atoms passing through them can be recorded, similarly to charged particles in the PICMC module. If such membranes are placed just above a surface to be coated, the recorded energy and angular

[10] Values taken from reference [22]

histograms can provide inputs for thin film growth simulations. The topic of film morphology simulation will be discussed in chapter 4, section 4.2.

1.2.4 CERN infrastructure for High Performance Computing

The CERN infrastructure for High Performance Computing (HPC) has greatly evolved over the years of this PhD study thanks to the outstanding commitment of the CERN IT Department. Starting from a small cluster dedicated to our application, it has been merged into a much larger framework involving many fields of applications and groups at CERN. It is now composed of 104 *legacy* Quanta 16 core / 128 GB RAM Intel®Xeon®E5-2650 v2 @2.60 GHz CPUs with a low latency GB Ethernet data interconnect, and 144 Intel ®Broadwell 20 core (40 cores with HyperThreading) / 128 GB RAM E5-2630v4 @2.20 GHz CPUs with Infiniband interconnect. Both clusters are part of the same HPC batch facility running with CERN CentOS 7 [11] Linux distribution. They use SLURM[12] as a job scheduler and several *Message Passing Interface* (MPI) implementations are offered. The PICMC/DSMC simulation code is run using MVAPICH2 2.2[13].
A 17 TB disk space enables temporary storage of simulation data, while long term storage is achieved with the CERN EOS Open Storage[14] infrastructure.

1.3 Thesis goals

In this introductory chapter, we have presented the concept of DC glow discharge plasmas and their use for thin film coatings, with a focus on niobium-on-copper deposition for SRF applications. Since large and complex RF cavity geometries along with diversity of coating configurations result in expensive and time-consuming experimental R&D phases, the need for numerical simulations was motivated. Therefore, the choice of a Particle-in-Cell Monte Carlo/ Direct Simulation Monte Carlo code[4] was justified, and its features were described.

The aim of the present work is to benchmark the chosen numerical code against experimental results such that the validity of each simulation step can be assessed and used to develop an *ab initio* methodology for RF cavity coating modelling, from plasma ignition to deposition of sputtered atoms on the cavity surface, and of the resulting thin film morphology.
This is the first time that such a task is undertaken at CERN, and, to our knowledge, elsewhere.

Following the outline presented in figure 1, chapter 2 will first focus on the validation of PICMC plasma simulations. Then, chapter 3 will expand plasma simulation results to the study of DSMC neutral atom transport simulations. Finally, chapter 4 will apply the validated methodology to real case studies.

[11] http://linux.web.cern.ch/linux/centos7/
[12] https://slurm.schedmd.com/
[13] http://mvapich.cse.ohio-state.edu/
[14] http://eos.web.cern.ch/

2 Plasma simulations: validation in a coaxial cylindrical source

In this chapter, we focus on the numerical validation of two physical parameters which have a strong influence on the plasma behaviour: the ion-induced secondary electron emission (IISEE) yield γ_{IISEE} related to the argon ion bombardment on the niobium target, and the initial energy distribution function of the secondary emitted electrons from this niobium cathode. γ_{IISEE} is also known in DC plasma discharge theory as Townsend's second ionisation coefficient, and its influence on gas breakdown was discussed in section 1.1.1.2.
An accurate modelling of IISEE is required to predict the viability of plasma sputtering sources in terms of plasma ignition for given process parameters, and also in terms of macroscopic parameters such as discharge current and voltage. Moreover, accurate plasma modelling is of utmost importance since the plasma behaviour defines the target erosion profile and its corresponding sputtering profile, which is critical for the coating characteristics.

In section 2.1, we first describe the experimental system specifically developed to benchmark plasma simulations. Then, as reliable data for IISEE are often difficult to find for the range of ion energies commonly found in sub-keV plasma discharges such as the present ones (see section 1.1.1.4), we numerically determine in section 2.2 suitable IISEE parameters by comparing simulated macroscopic outputs (discharge voltage and current) with their experimental counterparts for different DC plasma regimes (diode and magnetron) and different process pressures. Simulated local plasma parameters (electron density and energy, electric potential) are then compared with the experimental ones by means of Langmuir probe measurements. An article summarizing these results is currently under preparation. At last, in section 2.3, we discuss the validity of simulation mesh size Δx and time step Δt in 2D simulations corresponding to an horizontal slice of the full system, both in diode and magnetron.

2.1 Experimental system

2.1.1 Description

An experimental system was specifically developed to validate simulation results. As shown in figure 2.1, it consists in a 1.1 m vertical cylindrical vacuum chamber of 200 mm diameter. A 2.8 mm diameter copper cable insulated with kapton is wound around the main chamber on a 990 mm length to provide a solenoidal axial magnetic field when magnetron operation is required. The solenoid is powered by a Delta Elektronika SM 60-100 DC power supply. Pumping is ensured by a turbomolecular pump (Pfeiffer TMU 071 P, 60 [l/s] volume flow rate for N_2) backed up with a primary pump. The system base pressure as measured with a Penning gauge (Pfeiffer PKR 261) is in the 10^{-7}-10^{-6} mbar range in the main chamber without bake-out. A glass viewport is mounted at the bottom of the main chamber such that the plasma discharge can be visually monitored.

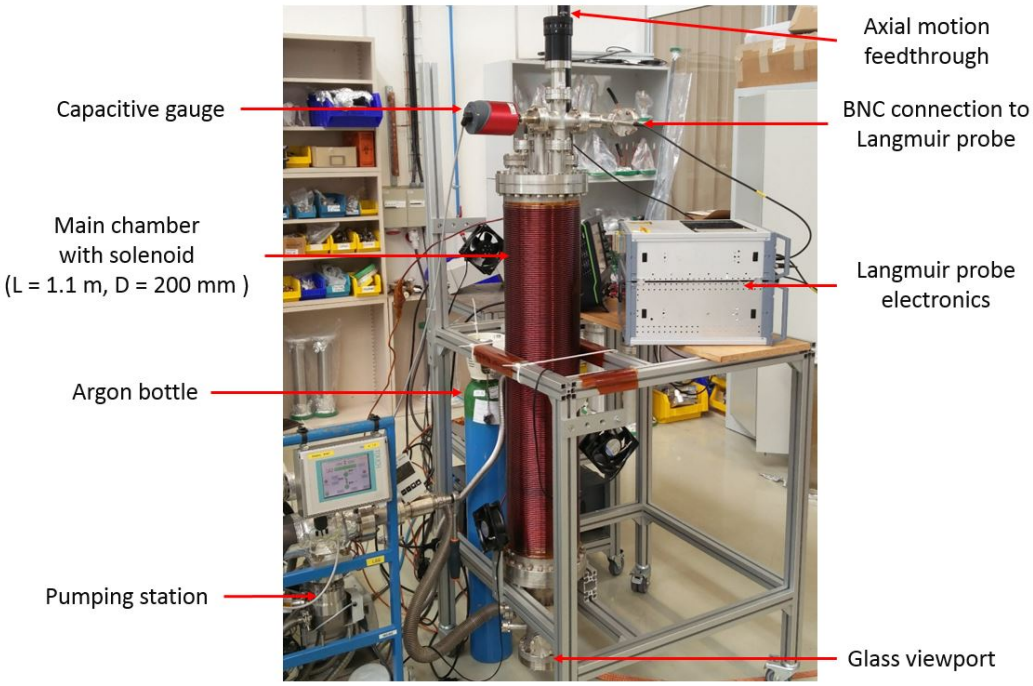

Figure 2.1 – Global view of the experimental setup with constitutive elements.

The layout of the vacuum system is depicted in figure 2.2. A VAT variable leak valve is connected between the argon injection line and the main chamber, and two capacitive diaphragm gauges (Pfeiffer CMR 364 and CMR 374) are located on top of the chamber and in front of the injection line valve. To precisely control the argon pressure in the chamber during plasma operation, the right angle valve connecting the pumping system to the main chamber is partially closed during argon injection, and the variable leak valve is adjusted to have a stable argon pressure measured by both capacitive gauges.

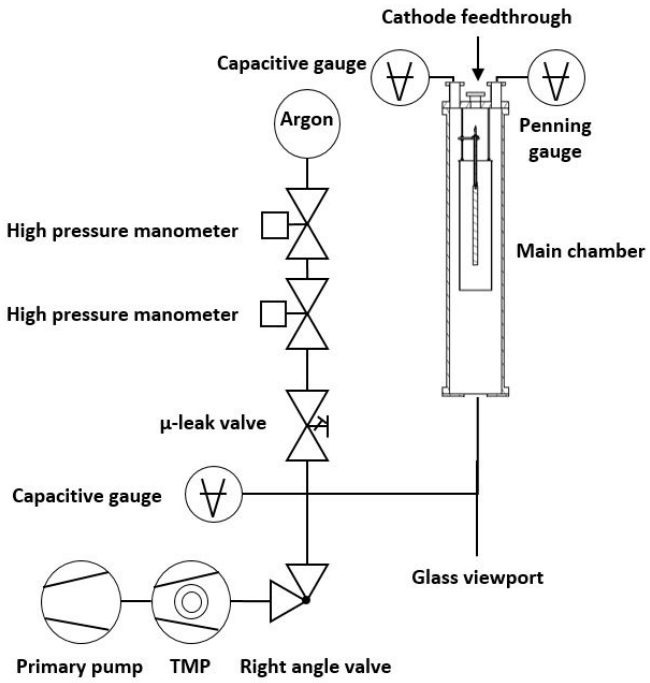

Figure 2.2 – Layout of the vacuum system.

Inside the main chamber, a niobium rod cathode (18 mm diameter, 303 mm length) is coaxially mounted inside a stainless steel anode (125 mm average diameter, 500 mm length) as shown in figure 2.3. This anode is made of two half shells creating an octagon when assembled together, such that an azimuthal symmetry close to that of a cylinder is kept. This peculiar shape is chosen to enable an easy fixation on one of the anode planar faces of a metal sample used in chapter 3 for *ex situ* thin film thickness analysis. In addition, the octagonal shape allows a better alignment of a vertically moved Langmuir probe, whose design will be described in section 2.1.2.

The average cathode-anode gap distance of 51.5 mm is chosen equal to the one between cavity and cathode in the HIE-ISOLDE coating assembly [10]. The anode is grounded through fixation threads attached to the main chamber top flange. During plasma operation, a negative bias voltage is applied on the cathode by using a MDX 500 Advanced Energy power supply unit regulating the discharge power. This unit can deliver up to 1000V - 0.5 A, with an accuracy of 0.2% of the full rated output, which was verified by voltage and current probes, such that discharge voltage and current values are directly read from the power supply display.

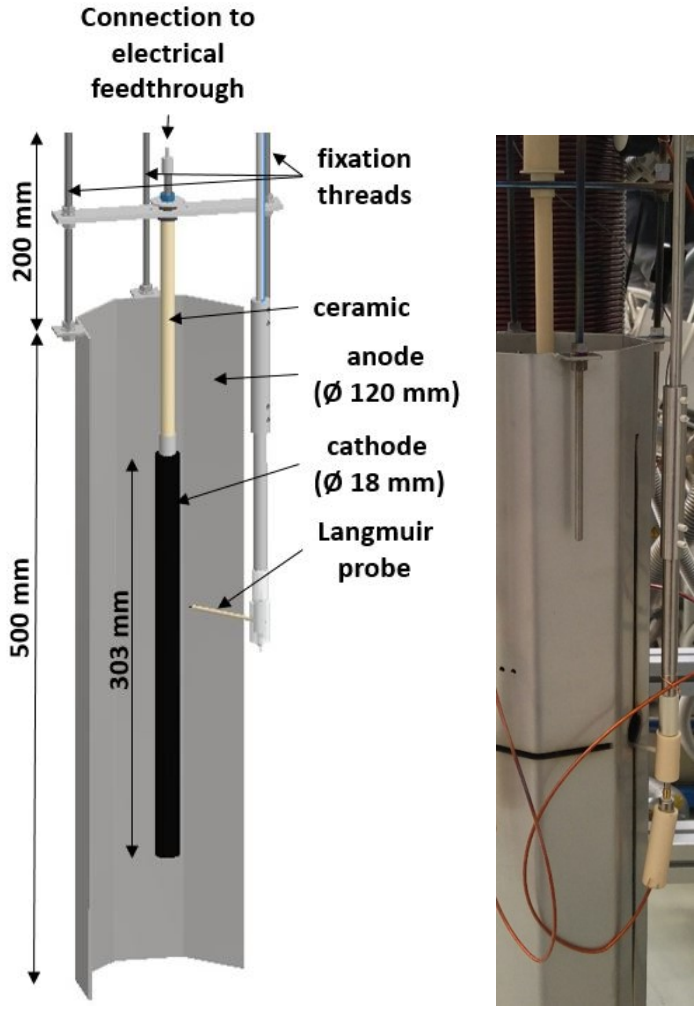

(a) (b)

Figure 2.3 – (a) Schematic cutview and (b) picture of the experimental setup showing the peculiar octagonal shape of the anode, which allows easy mounting of to-be coated sample on one of the 8 vertical walls. The grounded stainless steel anode is attached to the top flange using fixation threads, and the discharge power is applied on the niobium cathode. The whole assembly is inserted in the vertical vacuum chamber with an external solenoid winding, as shown in figure 2.1.

2.1.2 Langmuir probe

2.1.2.1 Theory

Langmuir probes are one of the earliest plasma diagnostics. Introduced by Mott-Smith and Langmuir in 1926[62], a Langmuir probe consists of a metal electrode which can draw a current I according to its bias voltage V when inserted in a plasma. Local plasma parameters such as electron density n_e, electron temperature T_e, floating potential V_f and plasma potential V_0 can be deduced from the analysis of such I(V) curves. Langmuir probe are more straightforward to implement in experimental systems than optical diagnostics, and can provide local plasma parameters estimates rather than integrated ones. Their main disadvantages are their perturbing effect on the plasma at their vicinity and the difficulty of I(V) characteristics analysis.

A typical Langmuir probe characteristic curve I(V) is drawn in figure 2.4. When a negative voltage V_a is applied to such a probe immersed in a plasma volume, the drawn current is negative (by convention) and only ions are collected (ion collection region, $V_a \ll V_f$). By increasing V_a, less ions and more electrons are collected until the floating potential V_f is reached for I = 0. Further increasing the probe voltage V_a, the probe current I increases exponentially with a slope related to the inverse of the electron temperature T_e. The plasma potential V_0 is reached and corresponds to an inflexion of the I(V) characteristic. Finally, for $V_a \gg V_0$, only electrons are collected.

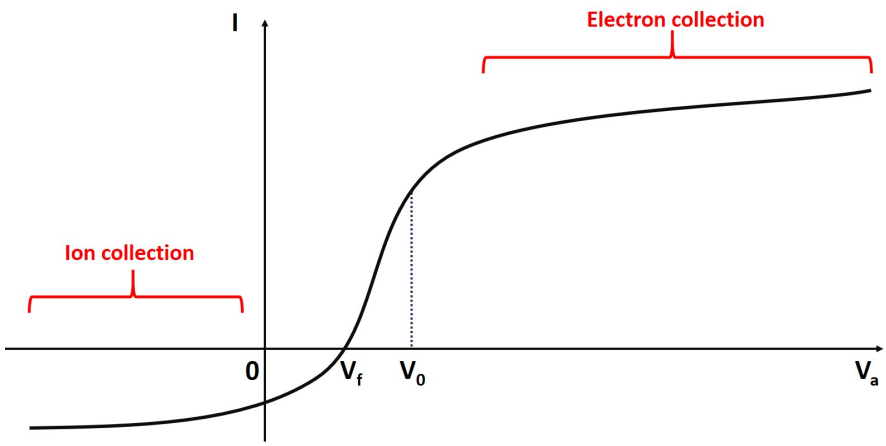

Figure 2.4 – Typical Langmuir probe I(V) characteristic, with indication of floating potential V_f and plasma potential V_0.

Several theories have been developed over the years to extract plasma parameters from the analysis of Langmuir probe I(V) characteristics. They rely on different assumptions depending on the probe geometry (planar, spherical or cylindrical) and size. For instance, Bohm first derived the ion current as $I = \alpha n_e e A_p v_B$, where α is the so-called pre-sheath density drop coefficient [63], A_p is the probe geometrical surface and $v_B = (eT_e/m_i)^{1/2}$ is the ion-sound velocity or Bohm velocity. This relation, frequently referred to as Bohm relation, neglects

sheath expansion which may happen when the probe is strongly negatively biased. Therefore its applicability is limited to cases where the dimension of the probe is much larger than the plasma Debye length [14, p. 191]. Furthermore, the value of the pre-sheath density drop, which is equal to 0.5 for collisionless plasmas, strongly depends upon the ion-neutral collision frequency and thus on the process gas pressure, further reducing the applicability of the Bohm relation to real applications such as those presented here. More complex theories have been developed to better describe ion collection, such as the Orbital Motion Limit (OML), the Allen-Boyd-Reynolds (ABR) or the Bernstein-Rabinowitz-Laframboise (BRL) models, for which a review can be found for example in [64]. A further complication is the use of magnetic fields in most conditions of practical relevance such as magnetron coating applications, which is not taken into account in the Bohm expression. As of today, no theory fully describes Langmuir probe I(V) characteristics in the presence of a magnetic field. It is generally assumed that the probe collection surface has to be modified from its geometrical expression A_p into its projection on the plane perpendicular to the field when the two following criteria are verified [14, p. 199]:

- the electron gyroradius $r_L = v_\perp/\Omega_c$ is smaller than the probe radius r_p, where $v_\perp$ is the electron velocity component orthogonal to the magnetic field **B**, and Ω_c is the cyclotron angular frequency
- the electron diffusion across the magnetic field is negligible with respect to the electron diffusion along the field lines, and the ion diffusion is not limited by the magnetic field.

In the present chapter, we will analyse Langmuir probe I(V) characteristics with the recent theory described in [65]. This choice is motivated by the following considerations. First, this newly-developed theory can be applied to cylindrical probes such as those used here, and it models the whole I(V) curve including the non-saturation of the ion current for negative bias voltages due to the sheath expansion. Furthermore, by describing the quasi-neutral pre-sheath and sheath regions with a unique equation, values of electron densities computed following the procedure of [65] depend weakly on the ion-neutral collision frequency in the pressure regimes of interest here, within an error of ~ 20% (P. Guittienne, private communications). Finally, this analysis of the I(V) characteristic focuses on the region between floating potential V_f and plasma potential V_0 in which measured currents are much larger than in the ion collection region, thus improving the signal-to-noise ratio of the collected current and reducing the error in electron density estimates compared with the previously mentioned other theories. The methodology of analysis will be described in details in section 2.1.2.3.

2.1.2.2 Experimental design

The Langmuir probe specifically developed in the course of this thesis, as shown in figure 2.3, is mounted on a 405 mm stroke linear vertical motion vacuum feedthrough. This allows axially resolved local plasma density, electron temperature and plasma potential measurements, to

provide an experimental comparison with simulation results. As seen in figure 2.5, the probe assembly consists of a 1 mm diameter tungsten wire (probe radius r_{probe} = 0.5 mm) inserted in a 1.6 mm inner diameter, 3 mm outer diameter alumina ceramic tubing attached to a vertical rod outside of the anode and connected to a vacuum compatible coaxial cable insulated with kapton. A slit in the anode allows the probe vertical motion inside the plasma region. The effective tungsten tip length immersed in the plasma is L_{probe} = 2 mm and the middle of the tip is located at 27 mm ± 1.5 mm from the cathode axis depending on the vertical position of the probe.

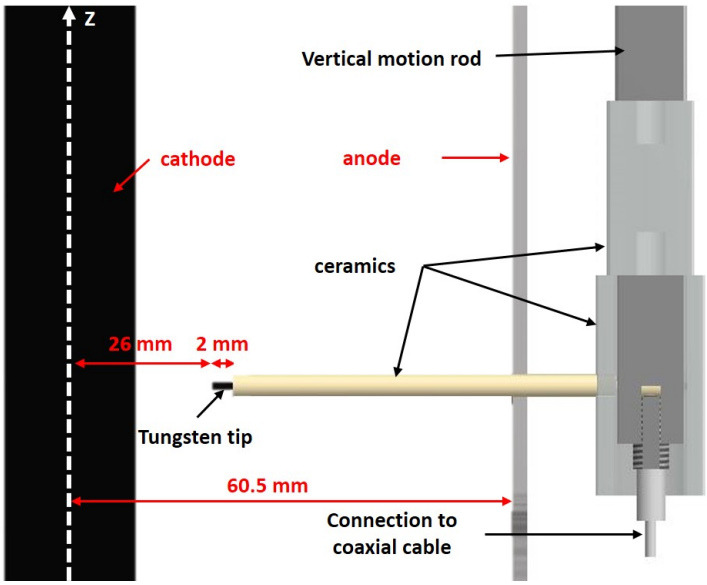

Figure 2.5 – Schematics of the Langmuir probe assembly. Zoomed view in figure 2.3(a). The white dashed line represents the vertical axis of the vacuum chamber.

2.1.2.3 Methodology for Langmuir probe data analysis

The probe is operated in sweeping mode by applying a triangular voltage V_a to the probe tip between -40 V and +3 V at a sweeping frequency f = 13.1 Hz. Both V_a and the current I drawn by the probe are recorded by an oscilloscope, with typical curves shown in figure 2.6.

These temporal traces are then plotted as a current density/voltage J(V) characteristic, as seen in figure 2.7 (black curve), by dividing the probe current I with the probe surface A_p.

In this chapter, J(V) characteristics are analysed according to the procedure suggested in [65, Appendix B.4]. First, the plasma potential V_0 [V] is estimated as the voltage corresponding to the maximum of the first derivative of the J(V) characteristic (see figure 2.7). Then, the electron temperature T_e [eV] is estimated as $T_e = J_0/k_0$, where J_0 [A.m^{-2}] and k_0 [A.m^{-2}.V^{-1}] are respectively the current density and the slope of the J(V) characteristics at the plasma potential. This estimate assumes that the ion thermal velocity $u_{thi} = \sqrt{\frac{qT_i}{m_i}}$ is neglected with

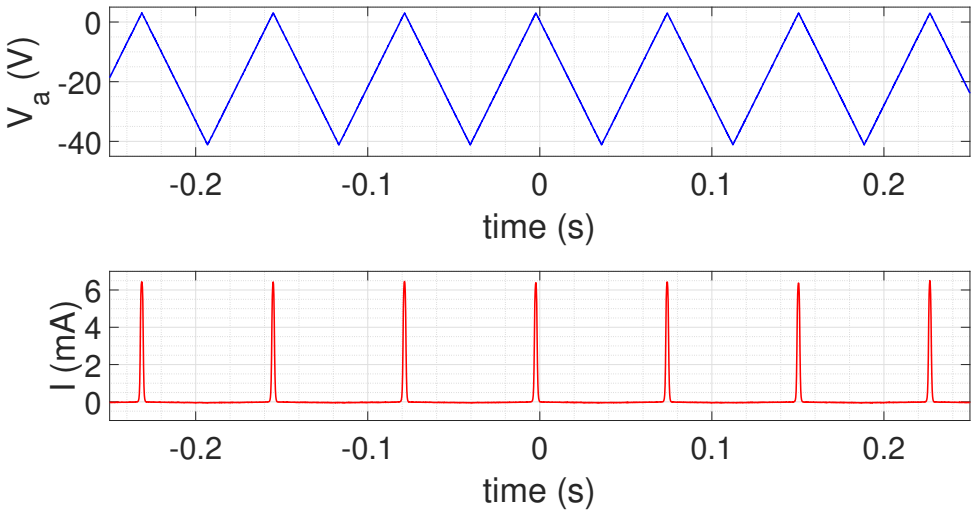

Figure 2.6 – Sweeping voltage V_a [V] applied to the Langmuir probe (top) and corresponding current (bottom) as recorded on the oscilloscope. P_{Ar}= 0.3 mbar, axial position in front of the cathode middle.

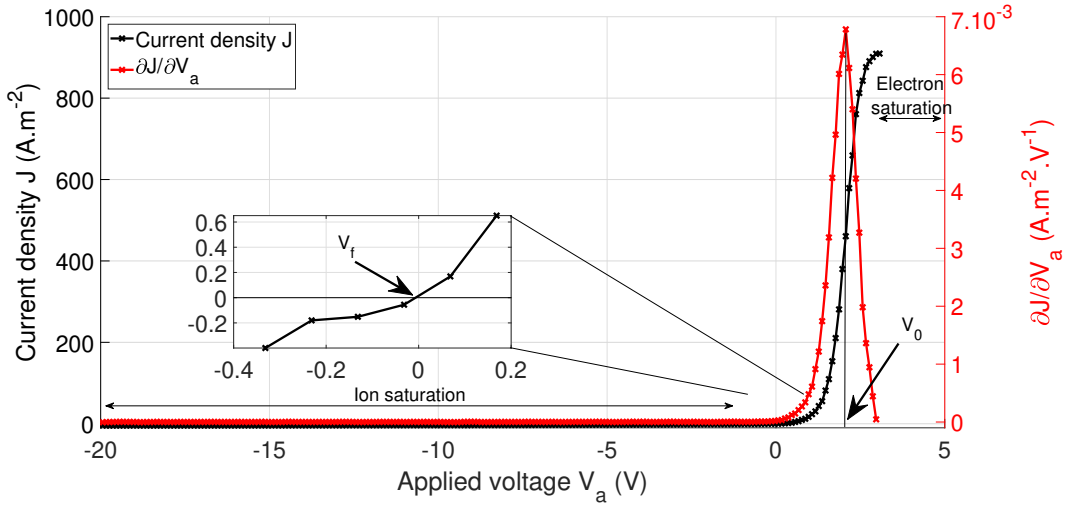

Figure 2.7 – Langmuir probe current density/voltage characteristic (black line with crosses) corresponding to the I/V temporal traces of figure 2.6, and its first derivative with respect to the probe applied voltage (red line with crosses), with indications of plasma potential V_0 and floating potential V_f, ion and electron saturation regions. Inset shows a zoom in the neighbourhood of the floating potential V_f. P_{Ar}= 0.3 mbar, axial position in front of the cathode middle.

respect to the electron thermal velocity $u_{the} = \sqrt{\frac{qT_e}{m_e}}$, where q [C] is the elementary charge, T_i [eV] is the ion temperature, m_i $[kg]$ and m_e $[kg]$ are the ion and electron masses respectively. The plasma density n_0 [m^{-3}] is estimated as $n_0 = \exp(1/2)J_0/qu_{the}$, and the floating potential

V_f [V] is estimated as the voltage for which the current density is equal to zero. These four values are used as initial guesses and the J(V) characteristic is fitted with a four-parameter fit from V_f to V_0 with the approximated expression of the current density collected by a cylindrical probe $J_{approx}(V_a)$ [A.m^{-2}] given in [65, Eq. B12]:

$$J_{approx}(V_a) = q u_{the} n_0 e^{-\frac{1}{2}-\frac{V_0}{T_e}} \left[e^{\frac{V_a}{T_e}} - e^{\frac{V_f}{T_e}} \right], \tag{2.1}$$

thus providing final values for T_e, V_0, n_0 and V_f.

2.2 Validation of ion-induced secondary electron emission parameters

2.2.1 Introduction

A description of ion-induced secondary electron emission (IISEE) was given in section 1.1.1.4. Empirical formulas found in the literature [21, 19, 16, 13] report yields γ_{IISEE} between 0.12 and 0.16 for potential emission of electrons by argon ion bombardment on niobium.
In the diode configuration, the exact initial energy distribution of the electrons is of little importance since electrons are radially accelerated by the electric field away from the cathode to several hundreds eV through the cathode sheath. This distribution plays a role in the magnetron case since the magnetic field can induce electron recollection on the cathode surface [21, 66].
Therefore, as a first step, γ_{IISEE} is numerically determined with diode simulations by changing the working pressure and matching simulated global plasma parameters (discharge current I and voltage V) with the experimental ones, while assuming a uniform initial electron energy distribution in the [0-5] eV interval and a cosine angular distribution. Simulated local plasma parameters (n_e, T_e, V_0) are compared with experimental ones measured with a Langmuir probe.
Then, by using the value for γ_{IISEE} determined in diode simulations, the approach described in [67] is applied to magnetron simulations by approximating the energy distribution of the secondary electrons as a Gaussian centred on $\frac{1}{2}(E_i - 2\phi) = 3.68$ eV with a cut-off energy $E_{\text{cut-off}}$ at $E_i - 2\phi = 7.36$ eV, where E_i is the argon ionization energy (15.76 eV), and ϕ is the niobium target work function (4.2 eV)[1]. The chosen parameters are again validated by comparing simulated discharge current and voltage with the experimental values, while varying the process pressure. Comparison of local plasma parameters extracted from the simulations and measured with the Langmuir probe is also given.

[1] According to [67], f(E, μ, σ) = $\frac{1}{\sigma\sqrt{2\pi}} exp\left(\frac{-(E-\mu)^2}{2\sigma^2}\right)$, where the mean $\mu = E_{\text{cut-off}}/2$ and the standard deviation $\sigma = E_{\text{cut-off}}/6$.

While the reason for choosing the IISEE parameters as the key to reliable plasma modelling was discussed at the beginning of this chapter, the accuracy of volume reactions and their collision cross-sections is also important. We do not tackle this question directly in the present work because argon discharge reactions implemented in the code library rely on trusted bibliographical references (see section 1.2.2.3). Nonetheless, the present study will show a match of macroscopic discharge parameters while changing the argon process gas pressure in DC diode and magnetron regimes, such that volume reactions are indirectly validated in this pressure change.

2.2.2 Simulation model and parameters

Plasma simulations are performed on a high performance computing (HPC) cluster installed at CERN (see section 1.2.4) with the Particle-in-Cell Monte Carlo (PIC-MC) parallel code developed at the Fraunhofer IST [4] and presented in section 1.2. The simulation geometry is designed with Autodesk Inventor Professional 2015 [68] in order to represent the 1.1 m experimental chamber in a slightly simplified way compared with the CAD view of figure 2.3(a). The simulation model is shown in figure 2.8, and includes cathode, anode, insulating ceramic and surrounding vacuum chamber while omitting Langmuir probe and small elements such as nuts, threads or connectors not relevant for the simulation. Surface meshing is obtained with the open source software GMSH [58], also used for 3D visualisation of simulations results. In this model, anode and chamber are defined as grounded elements, insulating ceramic as floating, and the negative bias voltage on the cathode is adjusted throughout the simulation run by a control loop ensuring power regulation. A summary of the numerical and physical parameters is presented in Table 2.1. To compare one-to-one simulation results with experiments, a constant power of 20 Watts is used in all simulations. Larger powers would generate larger currents and plasma densities, which in turn would result in unreasonable numerical constraints in terms of time step and mesh size. The Cartesian simulation volume mesh is refined inside the anode of 500 mm height (see figure 2.3(a)) where the plasma is denser, and made coarser outside of it. The scaling factor representing the number of argon simulation particles with respect to real particles is adjusted for each pressure to obtain approximately ten argon numerical particles in each 1 mm^3 cell in the refined mesh region. This ensures proper collision statistics.
Volume reactions involving argon atoms, ions, and electrons were described in section 1.2.2.3. Surface reactions are such that electrons and argon ions impinging on all surfaces are collected, with the emission of one neutral argon atom and electrons according to γ_{IISEE} with a cosine angular distribution for each collected ion. The use of these IISEE parameters for all surfaces assumes that ion-bombarded surfaces are either made of niobium (cathode) or covered with a niobium thin film, which becomes true in the experimental system after some time of plasma operation and subsequent niobium sputtering.

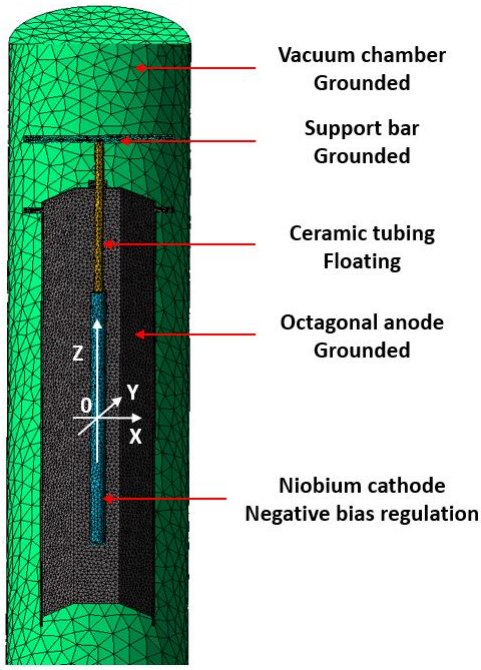

Figure 2.8 – Simulation model with surface mesh obtained with the GMSH software. Physical elements are listed with their applied electric potentials. The Cartesian reference system is shown with its origin O corresponding to the cathode center in XYZ.

Table 2.1 – Physical and numerical simulation parameters.

Domain size in XYZ [mm^3]	210x210x1100	
Mesh size inside the anode [mm^3]	1x1x1	
Species	Ar, Ar$^+$, e$^-$	
Discharge power [W]	20	
Time step [s]	5x10^{-12}	
CPU used per run (cores)	112	
Number of Ar superparticles per cell	10	
Scale factor Ar$^+$, e$^-$	1x10^5	
Initial density Ar$^+$, e$^-$ [m^{-3}]	5x10^{12}	
Simulation time	several weeks/months	
	Diode	Magnetron
Peak magnetic field [Gauss]	0	160
Ar pressure [mbar]	0.2, 0.3, 0.4	[3, 5, 7, 9]x10^{-2}
γ_{IISEE}	varied	0.13
IISE energy distribution	uniform in [0-5] eV	Gaussian
IISE angular distribution	cosine	cosine
Electron capture probability on physical surfaces	100 %	100 %

2.2.3 DC diode: numerical assessment of ion-induced secondary electron emission yield

2.2.3.1 Numerical assessment of γ_{IISEE} by comparison of discharge global parameters between simulations and experiments

Three simulations are performed with different γ_{IISEE} at P_{Ar} = 0.3 mbar. Table 2.2 presents the experimental discharge voltage and current at this pressure, along with the simulated ones as a function of γ_{IISEE}. It shows that increasing γ_{IISEE} in the simulations leads to a discharge

Table 2.2 – Comparison of simulated voltages and currents at different secondary electron yields γ_{IISEE} with experimental values in diode for P_{Ar} = 0.3 mbar, P_{dis} = 20 W.

		Voltage [V]	Current [mA]
Experiment		400	51
Simulation[1]	γ_{IISEE}		
	0.10	454	44
	0.12	418	48
	0.13	399	50

[1] Values are given for stable simulation current and voltage at t_{sim} = 7.5 μs.

voltage decrease (respectively a current increase) since it entails more electrons emitted from the cathode surface sourcing the plasma region. Moreover, a value of γ_{IISEE} = 0.13 provides simulated current and voltage fitting the experimental values for this given pressure.

To validate this value for γ_{IISEE}, we change the working pressure to verify whether the simulated discharge current and voltage match the experimental values. Indeed, a change of working pressure induces variations of discharge I/V values through a change of the number of collision reactions. By selecting γ_{IISEE} = 0.13, we perform two other plasma simulations at P_{Ar} = 0.2 mbar and P_{Ar} = 0.4 mbar. The choice of 0.2 mbar as the lowest pressure is justified by the voltage saturation of the power supply at 1000 V with a power setpoint P_{dis} = 20 W for pressures lower than 0.15 mbar. P_{Ar} = 0.2 mbar also corresponds to the pressure used in the coating process of the HIE-ISOLDE cavity [10]. The highest pressure of 0.4 mbar is selected as an upper limit for viability of the diode coating process. Indeed, due to a large number of scattering collisions between sputtered niobium and argon atoms, a pressure increase leads to high niobium redeposition on the cathode and very low deposition rates [12].

Figure 2.9 presents the time evolution of the simulated cathode voltage for the three pressures.

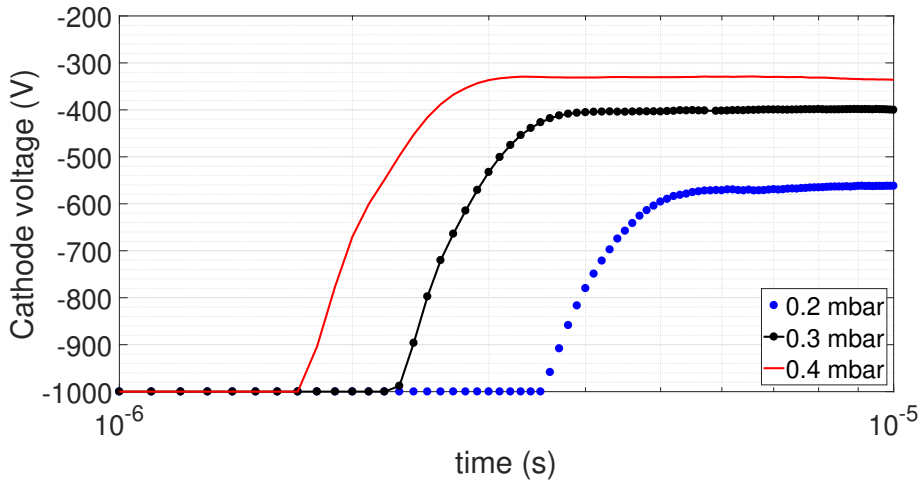

Figure 2.9 – Time evolution of the simulated cathode voltage in diode at different pressures for γ_{IISEE} = 0.13, P_{dis} = 20 W.

It shows that a higher process pressure results in a shorter ignition time, and that stable cathode voltages are reached after ~ 6 μs. Table 2.3 compares stable simulated I/V values taken from figure 2.9 with the experimental ones for the three pressures in DC diode.

Table 2.3 – Comparison of experimental and simulated voltages and currents in diode at different pressures for γ_{IISEE} = 0.13, P_{dis} = 20 W.

Pressure [mbar]	Voltage [V]		Current [mA]	
	Measurement[1]	Simulation[2]	Measurement[1]	Simulation[2]
0.2	557.9 ± 25.4	562.2 ± 0.2	37.3 ± 1.5	35.6 ± 0.03
0.3	400.4 ± 7.7	399.3 ± 0.6	51 ± 1.3	50 ± 0.2
0.4	339.9 ± 6.7	335.5 ± 0.4	60.1 ± 1.6	59.5 ± 0.2

[1] Error is ± the standard deviation σ over 7 different measurements.
[2] Error is $\pm\sigma$ over 0.5 μs at 10 μs converged simulation run.

It shows that the trend and the absolute values of the simulated currents and voltages match the experimental ones within their respective error bars. This confirms that the value of γ_{IISEE} = 0.13 is a suitable choice. The validity of this value is further confirmed by a loss of plasma sustainability for both simulation and experiment at P = 0.05 mbar, with voltages saturating at 1000V and weak currents of respectively 1.2 mA and 2 mA being delivered, both failing to reach the power setpoint of 20 Watts. This match is especially interesting for the design of future sputtering sources, since plasma sustainability at given process pressures could be predicted.

2.2.3.2 Comparison of local plasma parameters between simulations and experiments

Local plasma parameters can be extracted from each diode simulation listed in table 2.3, including electron and ion densities, mean energies of particles and electric potential. A view of the 3D electron density distribution is shown in figure 2.10(a) for P_{Ar} = 0.3 mbar, along with a photograph in figure 2.10(b) of the diode plasma taken through the viewport located at the bottom of the vacuum chamber.

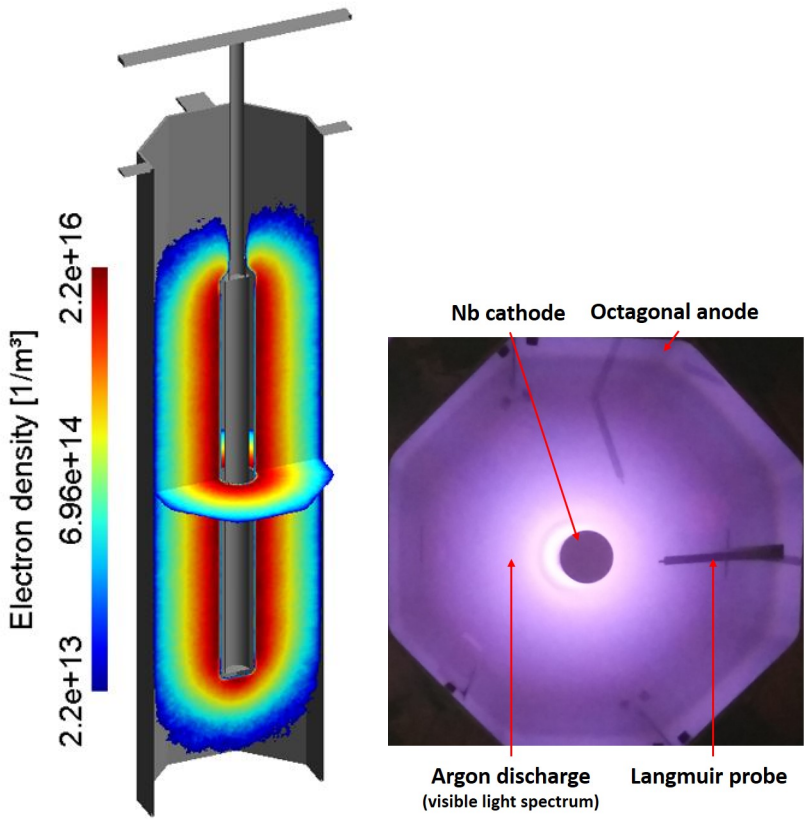

(a) (b)

Figure 2.10 – (a) Electron density [m^{-3}] displayed in the vertical and horizontal cutplanes at P = 0.3 mbar, diode, γ_{IISEE} = 0.13, t_{sim} = 10 μs, P_{dis} = 20 W (b) Picture of the diode argon plasma taken from a viewport below the chamber.

From 3D simulation profiles such as the one of figure 2.10(a), radial and axial profiles can be extracted so that local plasma parameters can be compared for the three pressures. The comparison uses profiles at the same simulation time t_{sim} = 10 μs, when discharge currents and voltages are stable. Radial profiles represent azimuthally-averaged values in the horizontal XY plane passing through the center of the cathode (see figure 2.8), in the cathode and anode discharge gap (9 - 60.5 mm). Axial plots are obtained similarly from azimuthally averaged values over a cylinder of 27 mm ± 1 mm radius around the cathode axis Z, axially centred on

the cathode. Figure 2.11 presents the electron density and energy radial and axial profiles, and electric potential radial profile for the three pressures.

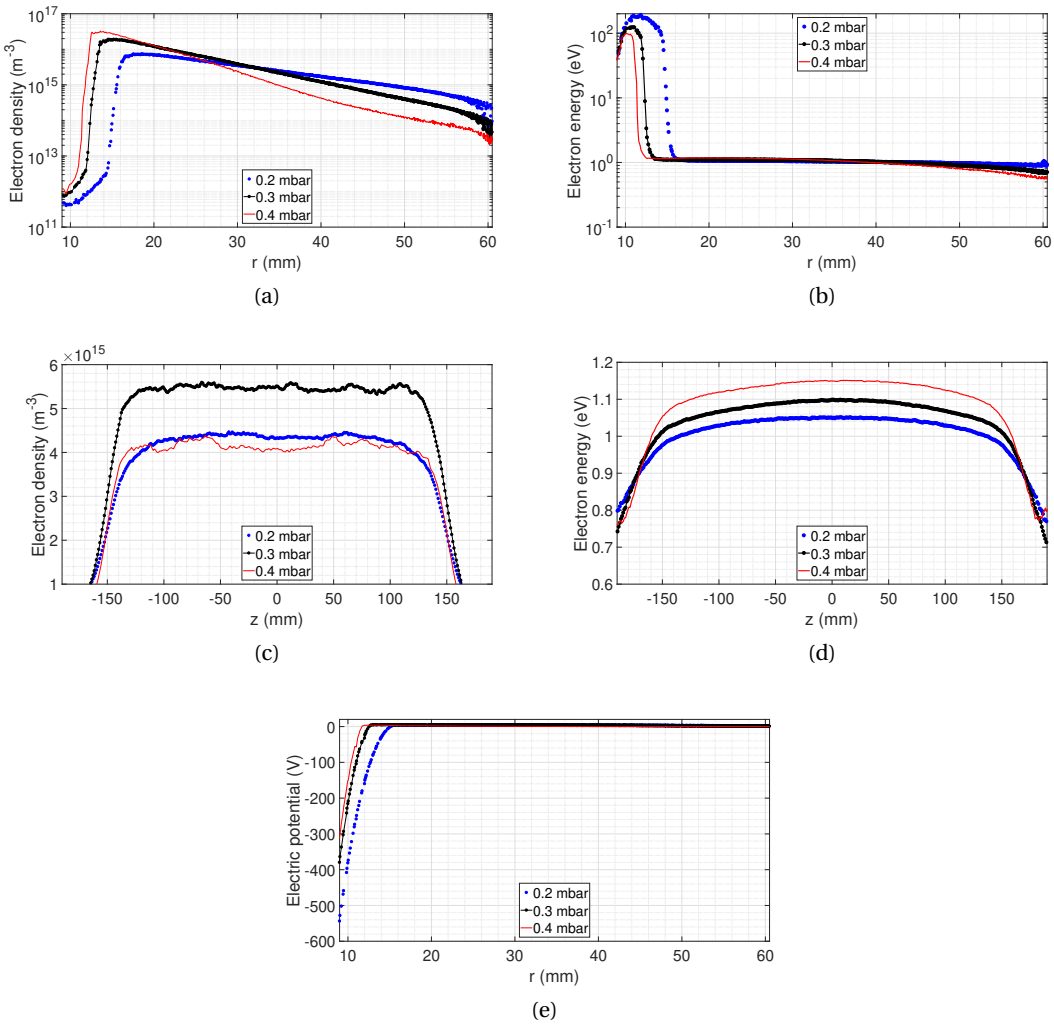

Figure 2.11 – Simulation results in diode configuration for the three process pressures at P_{dis} = 20 W: radial profiles at t_{sim} = 10 μs of (a) electron density [m^{-3}] and (b) electron energy [eV] in logarithmic scale in the XY plane of figure 2.8; Axial profiles of (c) electron density [m^{-3}] and (d) electron energy [eV] at 27 mm radius (e) Radial profile of the electric potential [V] in the XY plane of figure 2.8.

Increasing the pressure leads to a shift of the radial density peak position (figure 2.11(a)), along with a cathode sheath width reduction (figure 2.11(e)). Indeed, a higher pressure means that electrons accelerated through the cathode sheath experience more collisions with neutral argon particles, hence losing their energy in ionization reactions closer to the cathode (figure 2.11(b)).

Langmuir probe measurements are taken at the three pressures in the vertical axis direction, according to the probe configuration described in section 2.1.2. The probe surface used to convert the probe current into current density is the geometrical surface of the probe tip $A_p = 2\pi r_{probe} L_{probe} + \pi r_{probe}^2$. Similarly to the simulation results of figure 2.11, experimental plasma parameters taken at 27 mm radius from the cathode axis are almost pressure independent in the studied pressure range. Therefore, we only present in figure 2.12 the comparison of simulated and experimental plasma density, electron energy and plasma potential at P = 0.3 mbar.

We use a synthetic diagnostic to compare simulations and experiments, where simulated values are extracted from a cylinder of radius 27 mm ± 2.5 mm such that they match the probe spatial resolution. As such, average of the simulated results is presented with error bars corresponding to the spread in values over the 5 mm radius averaging[2]. Analysis of the J(V) probe characteristics yields the electron temperature T_e [eV], which is converted into electron energy E_e [eV] for comparison with the simulated profile of figure 2.12(b). This conversion assumes a Maxwellian energy distribution for the electrons, i.e. E_e [eV] = $\frac{3}{2}T_e$ [eV]. Experimental values extracted from the four-parameter fit (see 2.1.2) are displayed with experimental error bars taking into account probe surface uncertainty and estimations of errors on the determination of initial V_0, n_0 and E_e (converted from T_e) before the final four-parameter fit.

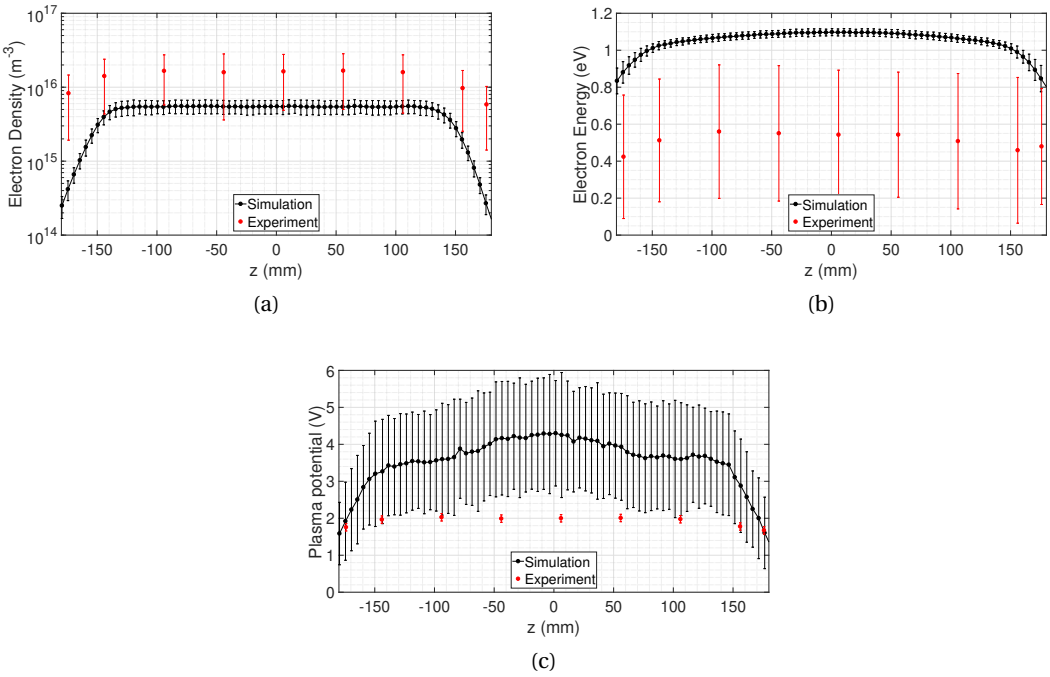

Figure 2.12 – Diode - Comparison at P = 0.3 mbar, P_{dis} = 20 W of simulation and Langmuir probe profiles of (a) Axial electron density n_e [m^{-3}] (b) Axial electron energy E_e [eV] (c) Axial plasma potential V_0 [V].

[2] $\pm 3\sigma$, where σ is the standard deviation over all values for the same axial position.

Figure 2.12 shows that experimental electron density (respectively electron energy, plasma potential) is about the double (respectively about the half) of its simulated equivalent in the central axial region (z ∈ [-150; 150] mm). The discrepancy between simulation and experiment can be partly explained by plasma perturbations induced when the probe voltage V_a is positively swept above the floating potential V_f. Indeed, electron peak currents collected by the probe are of ~ 6 mA, such as seen in figure 2.6, compared to a global discharge current of ~ 51 mA (see table 2.3 for P_{Ar} = 0.3 mbar). This means that for positive probe voltages V_a, electrons are collected from the plasma region much beyond the local probe region. By looking at figure 2.7, it means that for a given positive voltage V_a above V_f, the electron current is overestimated. This results in a plasma density n_e overestimate along with plasma potential V_0 and electron temperature T_e underestimates. This could also explain why the plasma density decay observed in the simulation profile for z < -150 mm and z > 150 mm is not well reproduced in the measurements, since the probe collects electrons from a large plasma region independently of its position. With this reasoning, real plasma parameters without probe perturbation would go in the direction of the simulated ones. It is worth mentioning that the probe perturbation does not impact the values given in table 2.3, since those are taken when the probe is electrically floating and axially positioned at the anode extremity.

2.2.4 DC magnetron: validation of ion-induced secondary electron energy distribution function

As explained in section 2.2.1, accurate magnetron discharge modelling depends on the use of a proper secondary electron initial energy distribution in addition to an accurate value of γ_{IISEE}. This is due to partial electron recollection on the cathode under the influence of the magnetic field, depending on the initial angle and energy of the secondary electrons. Such a recollection induces fewer electrons sourcing the plasma, and as such influences discharge currents and voltages.
To validate the use of a Gaussian initial secondary electron energy distribution described in [67], magnetron simulations are performed at different pressures with γ_{IISEE} = 0.13 according to the result of the previous section 2.2.3. The magnetic field mapping used as input for the simulations and corresponding to the experimental field is first described. Then, comparison of simulated discharge I/V values with experimental ones is shown. Finally, local plasma parameters extracted from the plasma simulations are compared with their experimental counterparts measured with the Langmuir probe described in section 2.1.2.

2.2.4.1 Solenoidal magnetic field mapping

Magnetron simulations require a mapping of the magnetic field as an input for the plasma simulation code (see 1.2.2.4). It can be either computed by the boundary element method (BEM) module of the PIC-MC code in the case of permanent magnet assemblies, or imported as a 3D mapping text file from an external source. Since the magnetic field is generated by a solenoid in the present setup, we choose the latter option. Thus, the magnetic field is

computed by using the magnetostatic module of the Opera commercial simulation software [69]. The solenoid model consists in a 990 mm tube of 220 mm inner diameter, 225.6 mm outer diameter. It corresponds to the experimental solenoid described in section 2.1.1. The solenoid model is displayed in figure 2.13 (red tube) along with the color mapping of the computed magnetic field for a simulation current density j = 4.648 A.mm^{-2}.

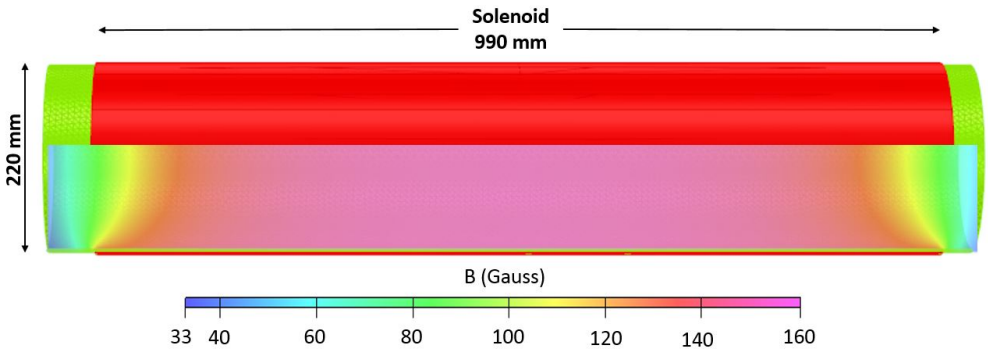

Figure 2.13 – Solenoid (red) and chamber (green) as modelled in Opera, with the computed magnetic field B (Gauss) overlaid for a simulation current density j = 4.648 A.mm^{-2}.

The simulated axial component of the magnetic field corresponding to a simulation current density of j = 0.581 A.mm^{-2} is found to match the experimental value measured on the solenoid axis with a gaussmeter and generated by a current I_{coil} = 10 A, as seen with the blue curves of figure 2.14. A linear scaling of the simulation current density and of the experimental I_{coil} at respectively j = 2.324 A.mm^{-2} and I_{coil} = 40 A shows a consistent agreement between simulation and measurement (red curves of figure 2.14).

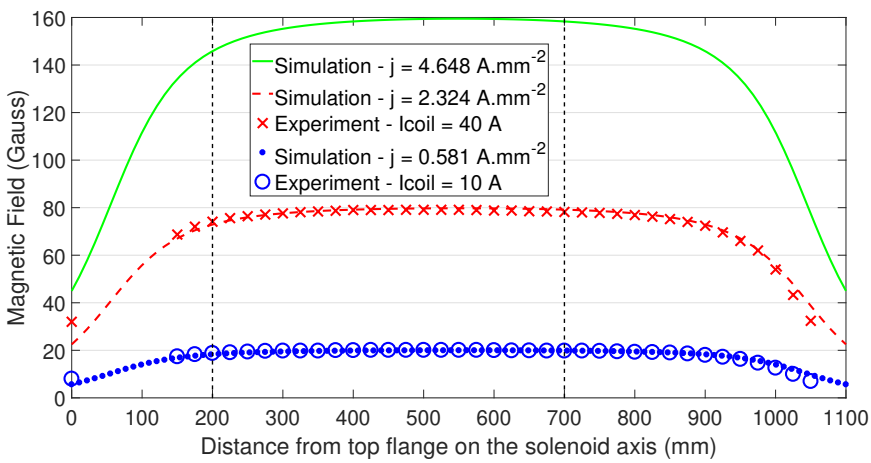

Figure 2.14 – Comparison of the axial component B_z of the solenoidal magnetic field computed with the Opera software and its value experimentally measured at different solenoid currents on the solenoid axis. Black vertical dashed lines at 200 mm and 700 mm represent respectively the octagonal anode top and bottom locations.

Therefore, the simulated field generated with j = 4.648 A.mm^{-2} (whose axial component is plotted with a green straight line in figure 2.14) is selected for the magnetron simulations presented in this section as an accurate 3D representation of the experimental field generated with a current I_{coil} = 80 A (not measured). The axial positioning of the anode at 200 - 700 mm below the main chamber top flange is chosen such that the anode lies in the uniform field region (B ~ 160 Gauss) thanks to the fixation threads (see figure 2.3), thus minimising edge effects on the plasma due to non-uniformity of the magnetic field.

2.2.4.2 Comparison of simulated and experimental discharge voltage and current

Four magnetron simulations are performed with their respective process pressures listed in table 2.1. The choice of these pressures is made as a trade-off between minimum pressure to obtain a sustainable plasma and upper limit pressure for viability of the magnetron coating process (same criterion as for the diode study). Other physical and numerical parameters are unchanged compared with the diode simulations.

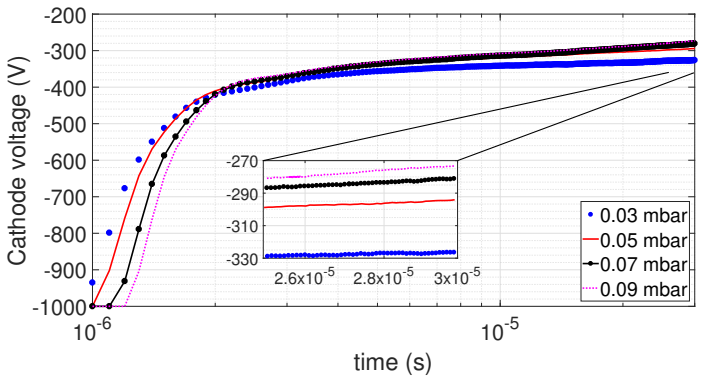

Figure 2.15 – Time evolution of the simulated cathode voltage in magnetron at different pressures, 160 Gauss, P_{dis} = 20 W.

Table 2.4 – Comparison of experimental and simulated voltages and currents in magnetron at different pressures, 160 Gauss, P_{dis} = 20 W.

Pressure [mbar]	Voltage [V]		Current [mA]	
	Measurement[1]	Simulation[2]	Measurement[1]	Simulation[2]
0.03	292.6 ± 3.4	326.4 ± 0.1	69.3 ± 1	61.3 ± 0.1
0.05	267.6 ± 1.6	294.3 ± 0.3	76.4 ± 1	68 ± 0.1
0.07	253.3 ± 2	281.2 ± 0.2	80.6 ± 1.1	71.2 ± 0.1
0.09	243.7 ± 2.7	273.5 ± 0.4	83.6 ± 1.5	73.2 ± 0.2

[1] Error is $\pm\sigma$ over 7 different measurements.
[2] Error is $\pm\sigma$ over 0.5 μs at 30 μs simulation time.

Figure 2.15 shows the time evolution of the simulated cathode voltage for the four pressures, while table 2.4 compares the experimental and simulated currents and voltages for the four different pressures. As before, experimental values are read from the power supply display, while simulated values are taken from figure 2.15 at t_{sim} = 30 μs. It can be seen in table 2.4 that the simulation trend matches the experimental one, such that increasing the pressure leads to a current increase and a voltage decrease. However, discrepancies of ~ 25-35 Volts can be noticed between measurement and simulation for the same pressure. This can be partly attributed to longer simulation stabilization times in the magnetron configuration than in the diode case, meaning that voltage convergence exhibits an exponential decay behaviour with a large characteristic time, as seen in figure 2.15. Therefore, simulation values given at 30 μs are slightly overestimating voltages (and thus underestimating currents) by ~ 10%.

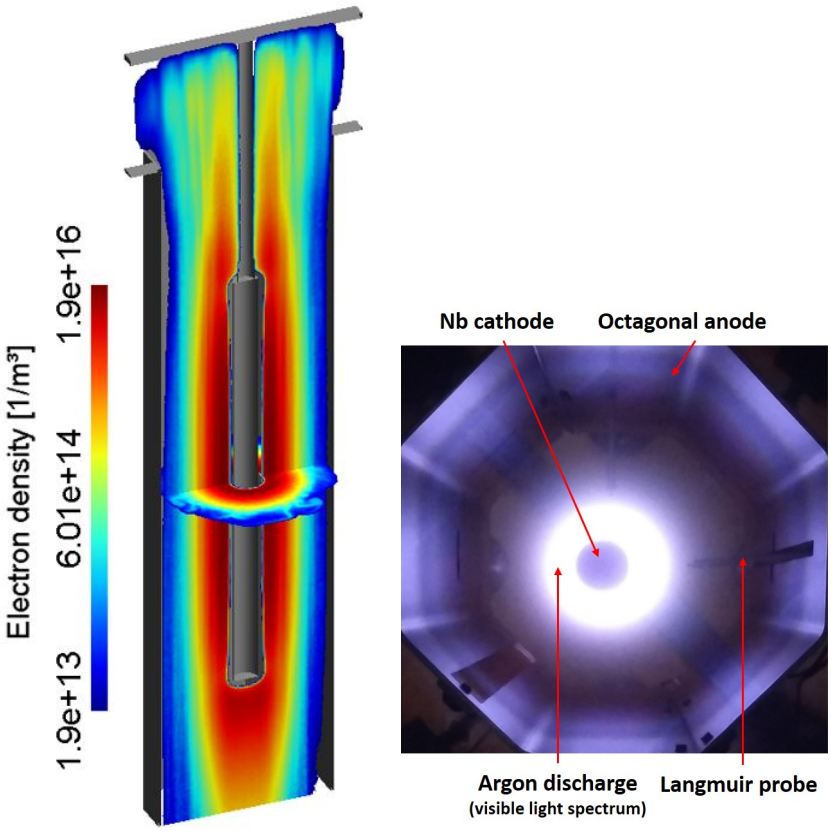

(a) (b)

Figure 2.16 – (a) Electron density [m^{-3}] displayed in the vertical and horizontal cutplanes at P = 0.05 mbar, magnetron, γ_{IISEE} = 0.13, Gaussian electron energy distribution, t_{sim} = 30 μs (b) Picture of the magnetron argon plasma taken from a viewport at the bottom of the chamber.

This slow convergence of the magnetron simulations can be explained by the drift of the charged species outside of the cathode-anode region, which can be seen in figure 2.16(a) showing electron density losses at the anode ends, leading to a large effective plasma volume and longer computation times along with longer physical times needed to reach a steady-state.

This phenomenon of electron end-losses was described in [70] for such a configuration, and is usually avoided in coating systems such as planar or post-magnetrons. In these latter, electron drift is limited by magnetic field lines returning to the cathode (in balanced magnetron) or by negatively biased electrostatic reflectors at the anode ends.
Plasma simulations should accurately model discharge voltages and currents such that sputtering profiles can be obtained and used for neutral atom transport simulations and quantitative prediction of thin film thickness. As such, and as a trade-off between reasonable computational time and required physical accuracy, the achieved agreement between simulated and experimental discharge current and voltage values meets the precision required for the present validation.

2.2.4.3 Comparison of local plasma parameters between simulations and experiments

Similarly to the study performed in the diode configuration in section 2.2.3.2, local plasma parameters are extracted from the simulations. Figure 2.17 presents the electron density and energy radial and axial plots, and electric potential radial plot at the four pressures. Pressure-dependent variations of plotted quantities are less pronounced than for the diode profiles (figure 2.11), and the decay of plasma characteristics (n_e in figure 2.17(c), E_e in figure 2.17(d)) is smoother along the z-axis because of electron end-losses bringing the plasma outside of the axial cathode region. Electron energies are higher than in diode configuration due to lower working pressures.

Langmuir probe measurements are taken at the four pressures in the vertical axis direction, similarly to the ones described in section 2.2.3.2. For the magnetron discharge, the probe surface used to convert the probe current into current density is taken as the projection of the probe tip geometrical surface onto the plane perpendicular to the magnetic field: $A_p = 2r_{probe}L_{probe}$, according to the explanation given in section 2.1.2.1. Indeed, with B = 160 gauss and $E_e \sim 2$ eV according to simulated values of figure 2.17(d), the electron gyroradius $r_L \sim 0.3$ mm is smaller than the probe typical size. Experimental plasma parameters taken at 27 mm radius from the cathode axis are almost identical for $P_{Ar} \in [0.05; 0.07; 0.09]$ mbar. As such, we only compare experimental measurements with simulated parameters using the synthetic diagnostic described in section 2.2.3.2 for the extreme pressures P_{Ar} = 0.03 mbar and 0.09 mbar, as shown in figure 2.18. We do not show plasma potential comparison as the one of figure 2.12c in diode, since local instabilities of the electric potential are present in magnetron and would make comparison with the probe measurements difficult.

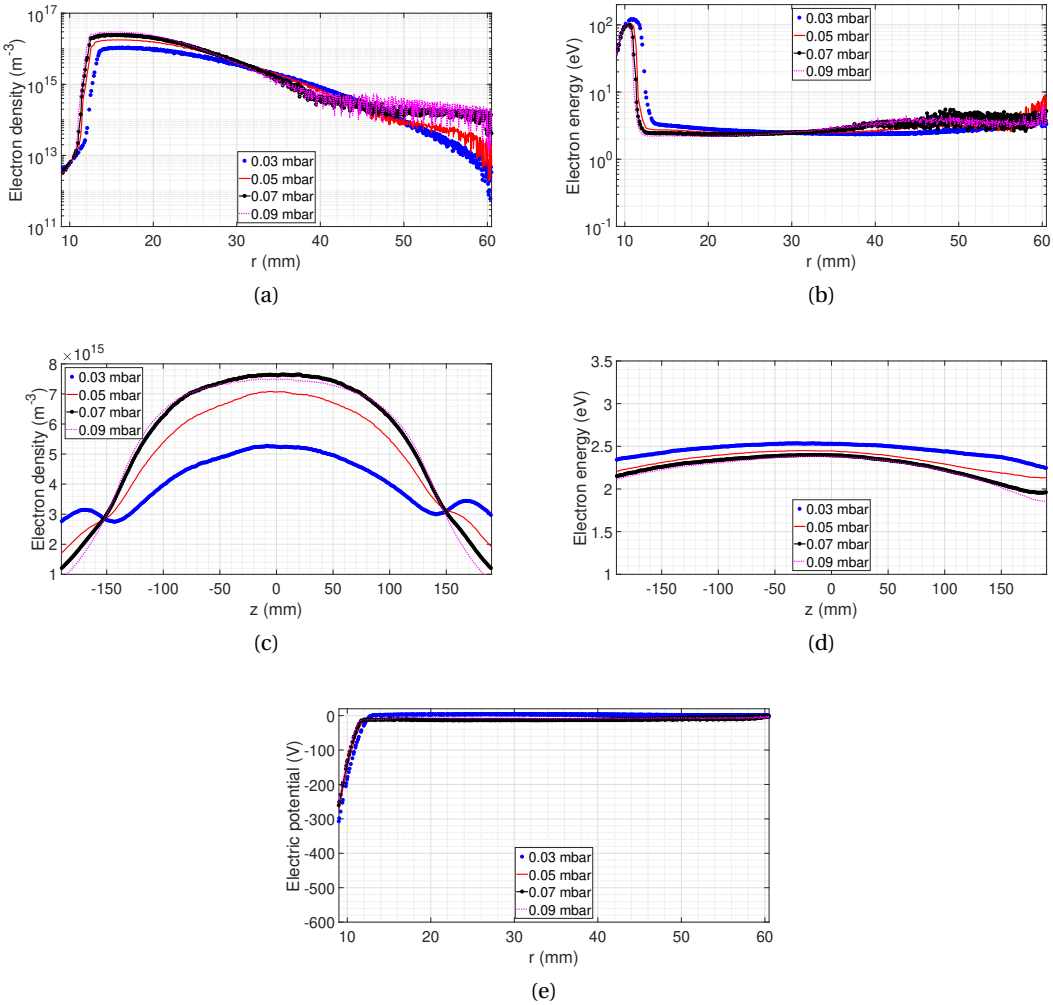

Figure 2.17 – Simulation results in magnetron configuration for the four process pressures at P_{dis} = 20 W: radial profiles at t_{sim} = 30 μs of (a) electron density [m^{-3}] and (b) electron energy [eV] in logarithmic scale in the XY plane of figure 2.8; axial profiles of (c) electron density [m^{-3}] and (d) electron energy [eV] at 27 mm radius (e) Radial profile of the electric potential [V] in the XY plane of figure 2.8.

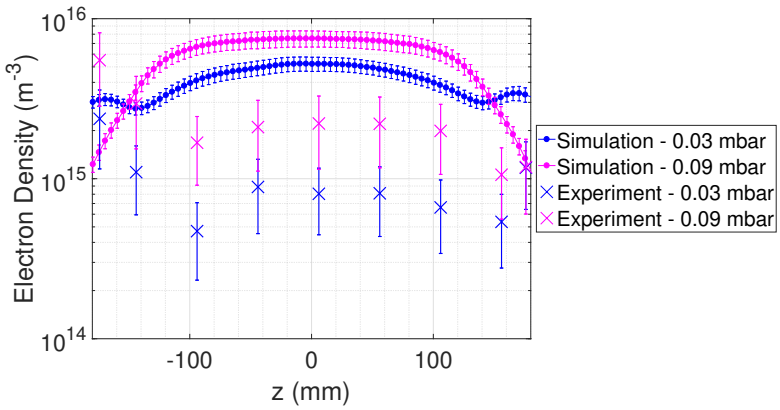

(a)

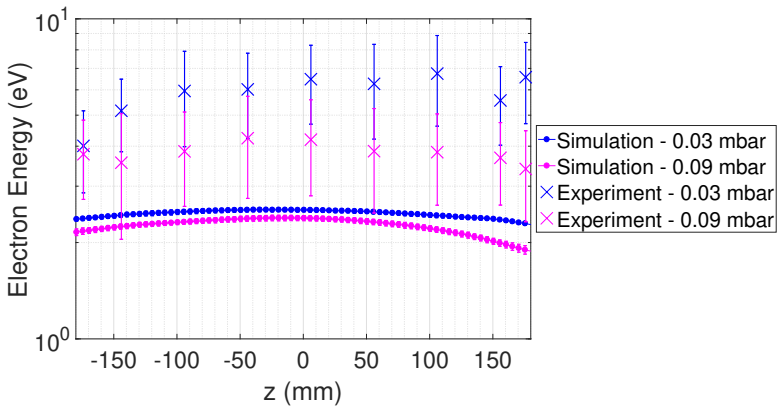

(b)

Figure 2.18 – Magnetron, P_{dis} = 20 W - Comparison of simulation and Langmuir probe profiles at P_{Ar} = 0.03 mbar and P_{Ar} = 0.09 mbar in semi-logarithmic scale of (a) Axial electron density n_e [m^{-3}] (b) Axial electron energy E_e [eV].

Figure 2.18(a) shows that simulated and experimental electron density profiles agree in shape at the exception of values for z < -100 mm. The experimental increase in density for these axial positions is consistently measured for all pressures, but remains unexplained. The simulated densities in the central axial region are 6.5 and 3.5 times higher than the experimental ones respectively for P_{Ar} = 0.03 mbar and P_{Ar} = 0.09 mbar, but the trend with pressure matches: a larger pressure results in a larger electron density in both simulation and experiment. The currents drawn by the probe are ten to twenty times smaller than the ones in diode and therefore do not disturb the plasma on a large scale. This may explain the reasonable agreement of measurements with simulations in magnetron despite the fact that the theory used for the analysis of Langmuir probe characteristics J(V) does not account for the presence of the magnetic field. Figure 2.18(b) also reveals a correspondence of relative electron energy profiles between simulation and experiment with a matching trend as a function of pressure, but simulated electron energies are 2.6 to 1.8 times lower than their experimental counterparts respectively for P_{Ar} = 0.03 mbar and P_{Ar} = 0.09 mbar.

2.2.5 Conclusion on 3D plasma simulations benchmarking

3D plasma simulations have been performed to numerically assess IISEE parameters suitable for accurate glow discharge modelling in both diode and magnetron configurations.
Absolute comparison of simulated profiles of local plasma parameters with experimental ones, such as those of electron density and electron temperature, has been challenging. Indeed, it was shown that Langmuir probe measurements induce local perturbations of the plasma discharge in the diode configuration at low discharge power. Furthermore, the theory used for Langmuir probe characteristics analysis relies on the assumption of a Maxwellian energy distribution for electrons, while simulation outputs provide electron energies averaged within each simulation cell. It was also explained that no theory can properly account for the presence of a magnetic field in Langmuir probe analysis. As such, possible reasons for discrepancies of local plasma parameters between simulations and experiments were given for both diode and magnetron configurations.
However, suitable IISEE yield and IISEE energy distribution function resulted in a match between simulated and experimental global discharge parameters (current and voltage) and paved the way towards accurate plasma modelling by using the PICMC method.

2.3 Discussion about time step and cell resolution in 2D simulations

2.3.1 Introduction

In this section, we study the influence of numerical parameters (cell resolution and time step) on the global and local discharge parameters. As explained in section 1.2.2.2, decreasing the values of these numerical parameters can be challenging both in terms of computational ressources and time, especially in the case of a large model such as the one of the present chapter. Therefore, we reduce here the model size of figure 2.8 to a horizontal slice of one cell height in Z while removing the gap between anode and vacuum chamber, as shown in figure 2.19.

This volume reduction requires that *periodic* boundary conditions are applied at the top and bottom ends of the model in the Z direction, which means that particles going out on one side are re-injected on the other. These boundary conditions thus imply an infinite model in the Z direction. Nonetheless, to keep physical parameters close to the 3D simulations, we linearly scale down the 3D discharge power setpoint of 20 W to 0.066 W to account for the cathode surface area of the 2D model, such that the power density is kept constant between 2D and 3D simulations.

First, we vary the mesh resolution Δx (= Δy) ∈ [0.1; 0.5; 1; 2] mm in the diode configuration at P_{Ar} = 0.3 mbar while keeping the time step Δt = 5x10^{-12} s. Then, we vary the mesh resolution in the same interval for two different Δt ∈ [2x10^{-11} ; 5x10^{-12}] s in the magnetron configuration at P_{Ar} = 3x10^{-2} mbar. Relevant numerical parameters are listed in table 2.5.

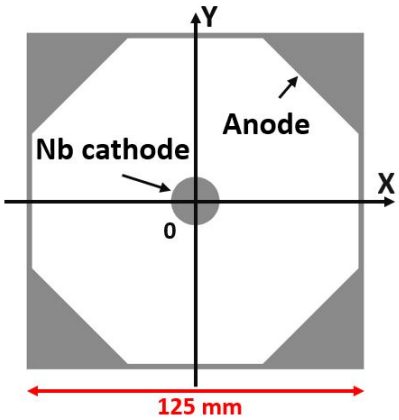

Figure 2.19 – Coaxial cylindrical system: 2D simulation model with physical elements and reference system. The model is one cell large in the Z direction, of 1 mm mesh size.

Table 2.5 – Physical and numerical parameters for the 2D simulations.

Domain size in XYZ [mm^3]			125x125x1		
Species			Ar, Ar$^+$, e$^-$		
Discharge power [W]			0.066		
Number of Ar superparticles per cell			10		
Scale factor Ar$^+$, e$^-$			1x10^5, unless mentioned otherwise		
Initial density Ar$^+$, e$^-$ [m^{-3}]			5x10^{12}		
γ_{IISEE}			0.13		
IISE energy distribution			Gaussian		
IISE angular distribution			cosine		
Electron capture probability on physical surfaces			100 %		
	P$_{Ar}$ [mbar]	Δt [s]	Δx [mm]	t$_{sim}$ [μs]	Computation time
Diode	0.3	5x10^{-12}	0.1	160	2 months
	0.3	5x10^{-12}	0.5	160	1 month
	0.3	5x10^{-12}	1	160	1 month
	0.3	5x10^{-12}	2	160	1 month
Magnetron B = 160 gauss	3x10^{-2}	2x10^{-11}	0.1	20	1 week
	3x10^{-2}	2x10^{-11}	0.5	400	1 week
	3x10^{-2}	2x10^{-11}	1	400	1 week
	3x10^{-2}	2x10^{-11}	2	280	1 week
Magnetron B = 160 gauss	3x10^{-2}	5x10^{-12}	0.1	400	2 months
	3x10^{-2}	5x10^{-12}	0.5	400	1 month
	3x10^{-2}	5x10^{-12}	1	400	1 month
	3x10^{-2}	5x10^{-12}	2	400	1 month

2.3.2 Variation of cell resolution in diode configuration with Δt = 5.10^{-12} s

The time evolution of the cathode voltage for the 2D diode simulations at different mesh sizes Δx and with Δt = 5x10^{-12} s is presented in figure 2.20.

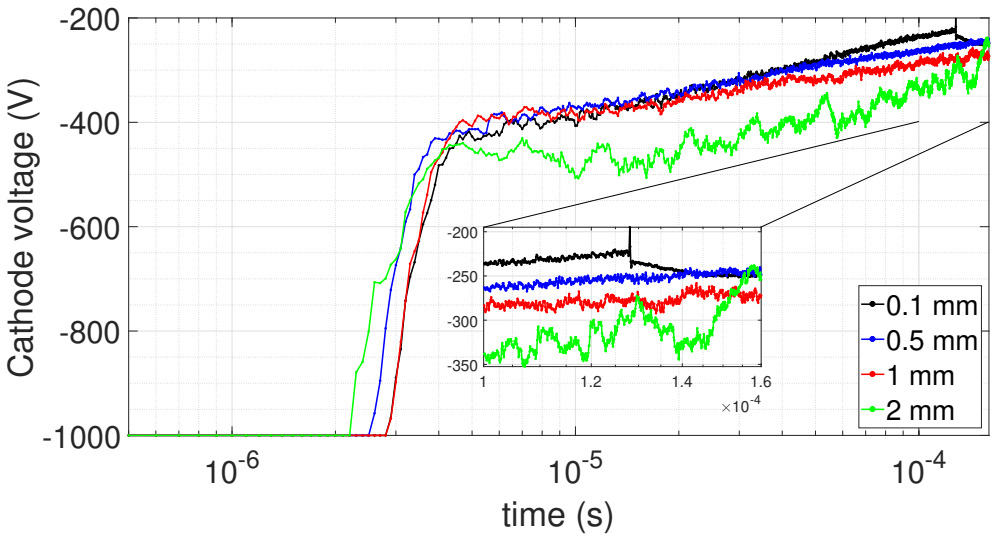

Figure 2.20 – 2D simulations, diode, P_{Ar} = 0.3 mbar, Δt = 5x10^{-12} s: cathode voltage evolution for different mesh sizes Δx. The jump of cathode voltage for Δx = 0.1 mm at t_{sim} ~ 1.3x10^{-4} s is due to a simulation restart with a scale factor for charged species modified from 10^5 to 10^4.

This figure shows that for all mesh sizes, the trend of the cathode voltage evolution is similar, and that stable values are reached around - 250 V, within a spread of ~ 30 V. The more negative voltage for Δx = 0.1 mm compared with the other cases is due to a too large scale factor for charged species. Indeed, when this factor is modified from 10^5 to 10^4 at t_{sim} ~ 1.3x10^{-4} s, the corresponding voltage curve (black) gets closer to the other ones. Furthermore, the voltage curve corresponding to Δx = 2 mm (green) is quite noisy and seems not to reach saturation compared with the others.

To explain these two observations, we compare in figure 2.21 the electron densities of the four simulations at t_{sim} = 160 μs. For a mesh size of Δx = 0.1 mm, a scale factor of 10^5 is too large since not enough charged superparticles are present within each cell for the computed electron densities displayed in figure 2.21, according to equation 1.18. Indeed, a density peak value of ~ 2x10^{17} [m^{-3}] corresponds to 20 superparticles per cell, and almost all cells contain less than this number. This results in poor collision statistics within each cell and explains why lowering the scale factor for this mesh size results in a convergence of the corresponding voltage curve of figure 2.20 (black) towards the ones corresponding to larger mesh sizes. In addition, figure 2.21(e) demonstrates that the coarse cell resolution for Δx = 2 mm, especially in the cathode sheath, can explain local plasma parameters inhomogeneities and hence the noisy voltage evolution of the green curve in figure 2.20.

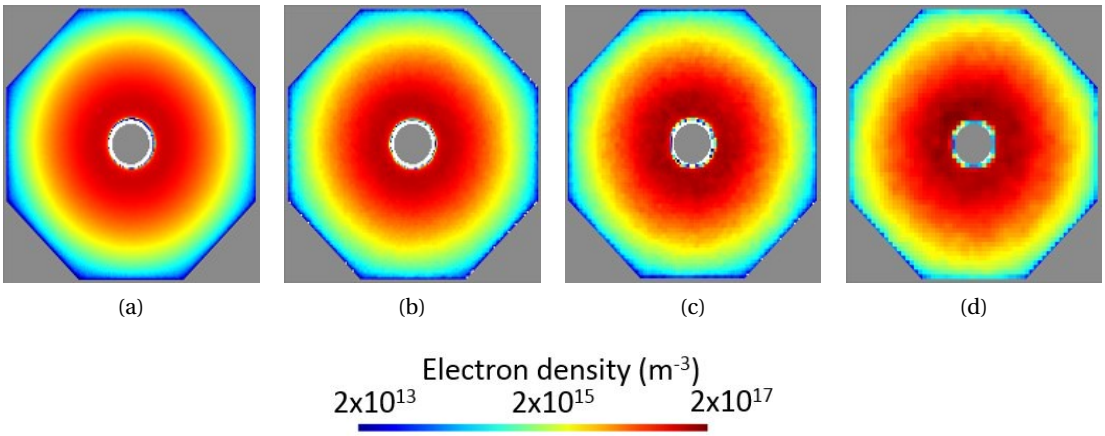

(e)

Figure 2.21 – 2D simulations, diode, P_{Ar} = 0.3 mbar, Δt = 5x10^{-12} s: electron density [m^{-3}] at t_{sim} = 160 μs for (a) Δx = 0.1 mm (b) Δx = 0.5 mm (c) Δx = 1 mm (d) Δx = 2 mm (e) Color code for electron density [m^{-3}].

By averaging such 2D plots over the azimuthal direction, we obtain the radial profiles of electron density, electron energy and electric potential, which are represented in figure 2.22.

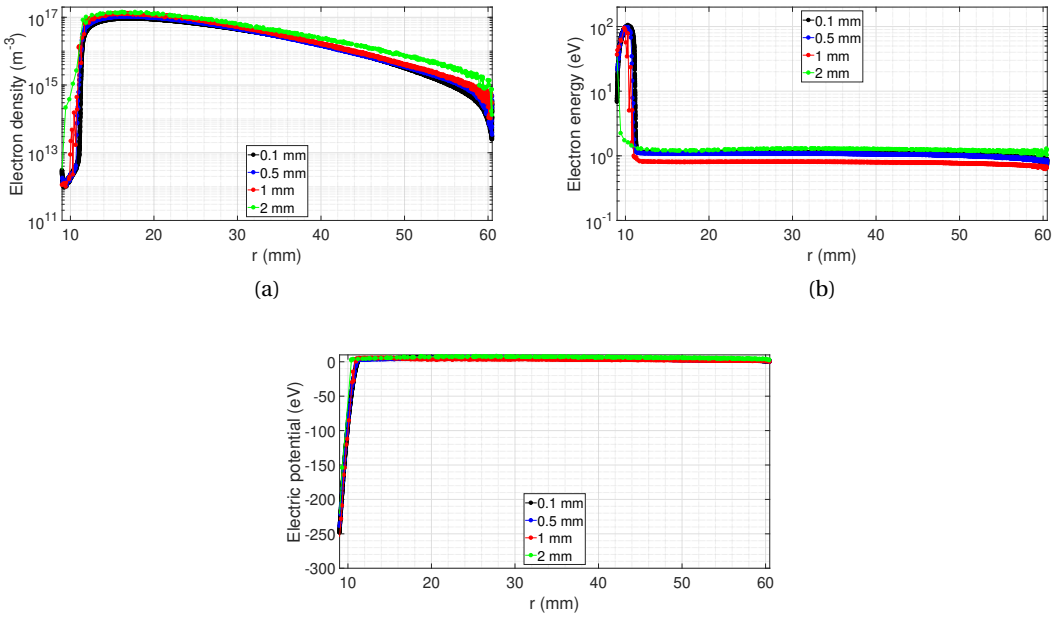

Figure 2.22 – 2D simulations, diode, P_{Ar} = 0.3 mbar, Δt = 5x10^{-12} s: radial profiles at t_{sim} = 160 μs of (a) Electron density [m^{-3}] (b) Electron energy [eV] (c) Electric potential [V].

Radial profiles of local plasma parameters are very similar for the different mesh sizes, at the exception of a lack of resolution in the cathode sheath for $\Delta x = 2$ mm (green). Furthermore, electron densities are ~ 5 times higher than in the 3D simulation at the same process pressure (see figure 2.11(a)), which can be explained by the infinite approximation of the 2D simulations that do not account for the 3D finite plasma volume. This approximation is responsible for larger simulation times needed to reach a converged cathode voltage in the 2D simulations compared with the 3D ones (see figure 2.9), and also explains why 2D voltages are less negative (~ -250 V) than in the 3D simulation (~ -400 V) for the same pressure $P_{Ar} = 0.3$ mbar.

2.3.3 Variation of cell resolution and time step in magnetron configuration

2.3.3.1 Magnetron with $\Delta t = 2.10^{-11}$ s

Similarly to the previous study in diode, we perform four magnetron simulations with different mesh sizes and with $\Delta t = 2\text{x}10^{-11}$ s. Time evolution of the cathode voltages is displayed in figure 2.23.

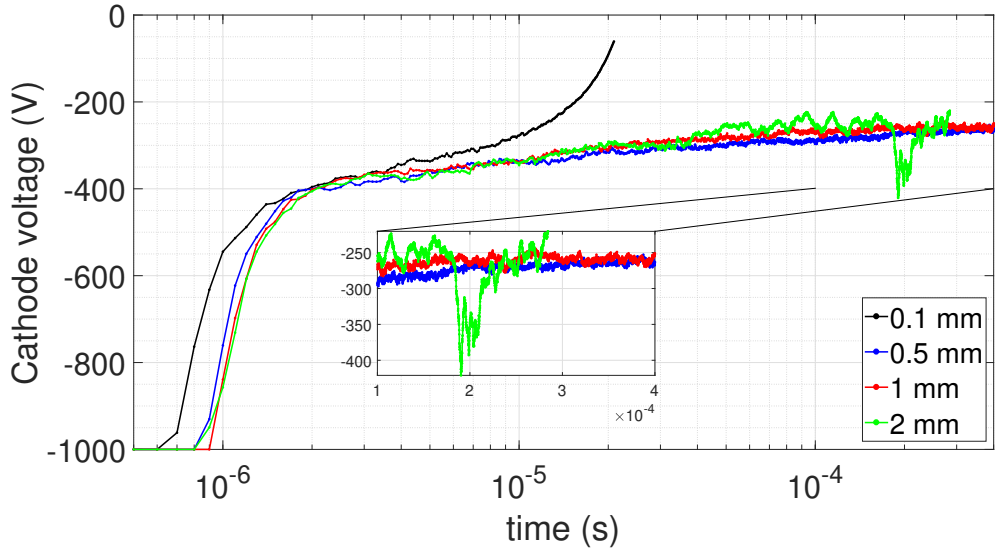

Figure 2.23 – 2D simulations, magnetron, B = 160 Gauss, $P_{Ar} = 0.03$ mbar, $\Delta t = 2\text{x}10^{-11}$ s: cathode voltage evolution for different mesh sizes Δx.

It can be seen that the blue curve ($\Delta x = 0.5$ mm) and the red curve ($\Delta x = 1$ mm) have an identical trend and converge to a stable voltage of ~ -260 V, within 20 V of each other. As observed in the diode simulations, the green curve ($\Delta x = 2$ mm) is quite noisy and unstable. Furthermore, the black curve ($\Delta x = 0.1$ mm) is rapidly diverging. This behaviour can partly be explained by a too large scale factor of 10^5 for charged species, which already resulted in a voltage underestimate in the diode case. In addition, electrons emitted from the cathode surface and accelerated to ~ 400 eV (corresponding to the cathode voltage before divergence)

would travel a distance d = 0.24 mm during a simulation time step $\Delta t = 2x10^{-11}$ s. This is larger than the mesh size $\Delta x = 0.1$ mm, and thus cell hopping can occur (see equation 1.14), further leading to poorly estimated collisions and cathode voltage divergence.

The electron densities are presented for the different mesh sizes and at different simulation times in figure 2.24.

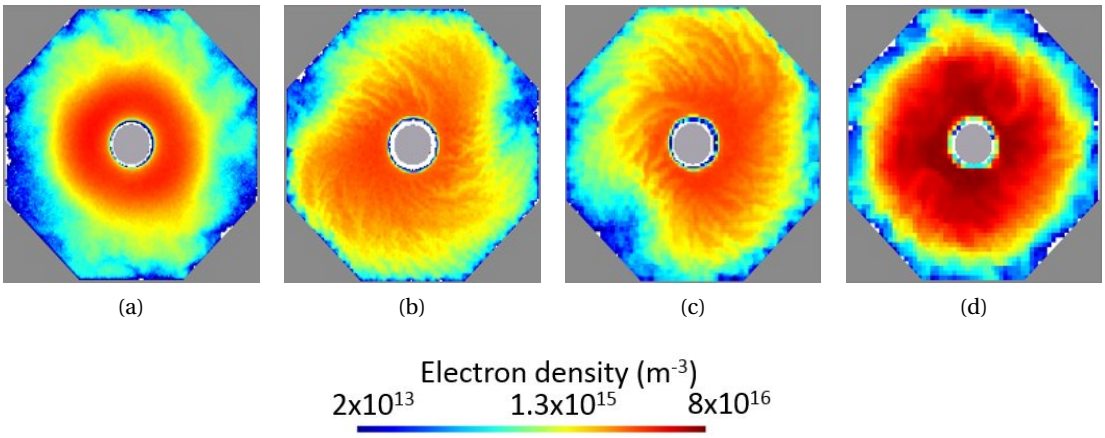

Figure 2.24 – 2D simulations, magnetron, B = 160 Gauss, P_{Ar} = 0.03 mbar, $\Delta t = 2x10^{-11}$ s: electron density [m^{-3}] for (a) $\Delta x = 0.1$ mm, $t_{sim} = 20\ \mu s$ (b) $\Delta x = 0.5$ mm, $t_{sim} = 400\ \mu s$ (c) $\Delta x = 1$ mm, $t_{sim} = 400\ \mu s$ (d) $\Delta x = 2$ mm, $t_{sim} = 280\ \mu s$ (e) Color code for electron density [m^{-3}].

This figure further confirms that no significant change occurs either in terms of plasma shape or electron density ranges between $\Delta x = 0.5$ mm (figure 2.24(b)) and $\Delta x = 1$ mm (figure 2.24(c)). The electron density profile corresponding to $\Delta x = 2$ mm (figure 2.24(d)) differs from the previous two in a lack of resolution in the cathode sheath and in an overestimate of electron densities, as it was already seen with the diode simulations. The profile corresponding to $\Delta x = 0.1$ mm (figure 2.24(a)) is hardly comparable with the others, as it is taken at $t_{sim} = 20\ \mu s$ because of the fast simulation divergence.
The radial profiles of the plasma parameters are shown in figure 2.25, and further confirm the similarity of the 0.5 and 1 mm mesh simulations, while the lack of cathode sheath resolution for $\Delta x = 2$ mm is further evidenced.

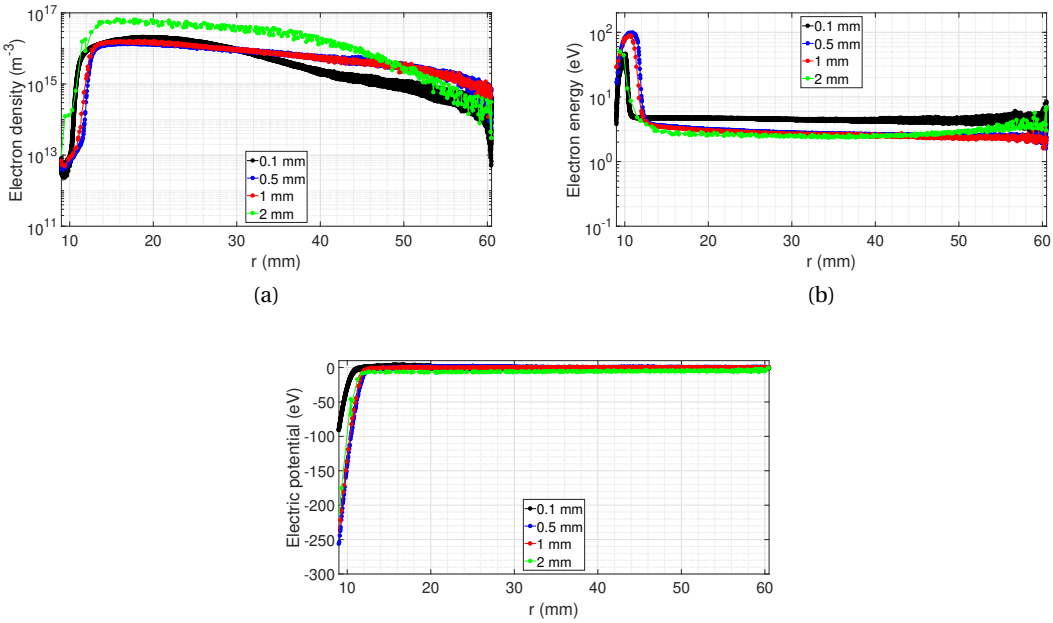

Figure 2.25 – 2D simulations, magnetron, B = 160 Gauss, P_{Ar} = 0.03 mbar, $\Delta t = 2\text{x}10^{-11}$ s: radial profiles of (a) Electron density [m^{-3}] (b) Electron energy [eV] (c) Electric potential [V]. Simulation times for each mesh size curve are the ones listed in the legend of figure 2.24.

2.3.3.2 Magnetron with $\Delta t = 5.10^{-12}$ s

The previous simulation time step is here reduced to $\Delta t = 5\text{x}10^{-12}$ s, and the cathode voltage time evolution for the four mesh sizes in magnetron is shown in figure 2.26.

While the green curve (Δx = 2 mm) is still noisy and unstable, the other three curves are similar and converge to a voltage value of ~ -260 V, within 10 V of each other. This voltage value is comparable to the one obtained in the previous section for Δx = 0.5 and 1 mm (see figure 2.23). Choosing $\Delta t = 5\text{x}10^{-12}$ s and reducing the scale factor for charged particles at $t_{sim} = 3.7\text{x}10^{-4}$ results in a convergence of the black curve (Δx = 0.1 mm). Therefore, the divergence observed for Δx = 0.1 mm in the previous section was indeed due to cell hopping, caused by too large simulation time step and scale factor for charged species.

Similarly to the previous sections, electron densities are displayed in figure 2.27, while radial profiles of plasma parameters are shown in figure 2.28. These two figures confirm that local plasma parameters for Δx = 0.1, 0.5 and 1 mm are in agreement, at the exception of a slight electron density underestimate of the two latter with respect to the former (figure 2.28(a)). They also reveal the lack of cathode sheath resolution for Δx = 2 mm, similarly to the previous sections. Finally, as for the diode case, peak electron densities are about twice higher than in the 3D simulations, which can be explained by the infinite assumption of 2D simulations.

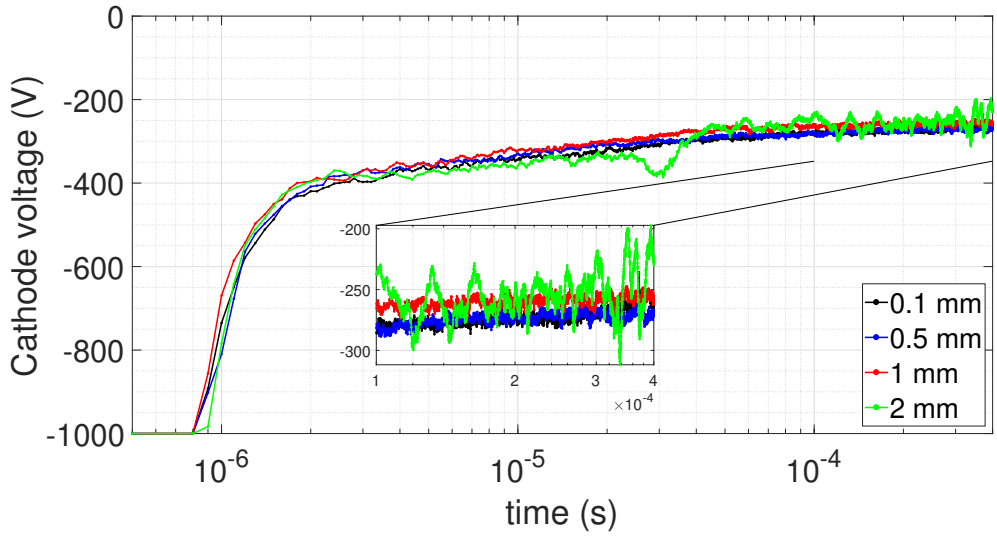

Figure 2.26 – 2D simulations, magnetron, B = 160 Gauss, P_{Ar} = 0.03 mbar, $\Delta t = 5\text{x}10^{-12}$ s: cathode voltage evolution for different mesh sizes Δx. The jump of cathode voltage for Δx = 0.1 mm at $t_{sim} \sim 3.7\text{x}10^{-4}$ s is due to a simulation restart with a scale factor for charged species modified from 10^5 to 10^4.

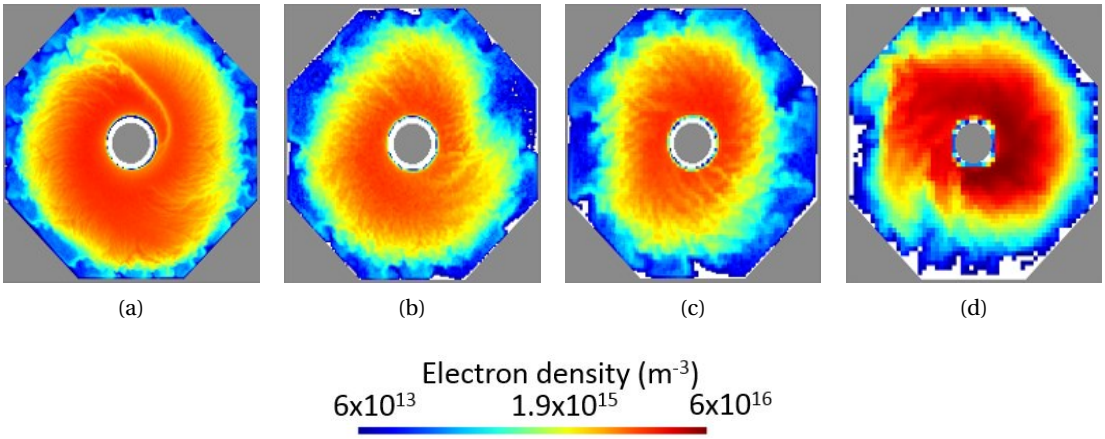

(e)

Figure 2.27 – 2D simulations, magnetron, B = 160 Gauss, P_{Ar} = 0.03 mbar, $\Delta t = 5\text{x}10^{-12}$ s: electron density [m^{-3}] at t_{sim} = 400 μs for (a) Δx = 0.1 mm (b) Δx = 0.5 mm (c) Δx = 1 mm (d) Δx = 2 mm (e) Color code for electron density [m^{-3}].

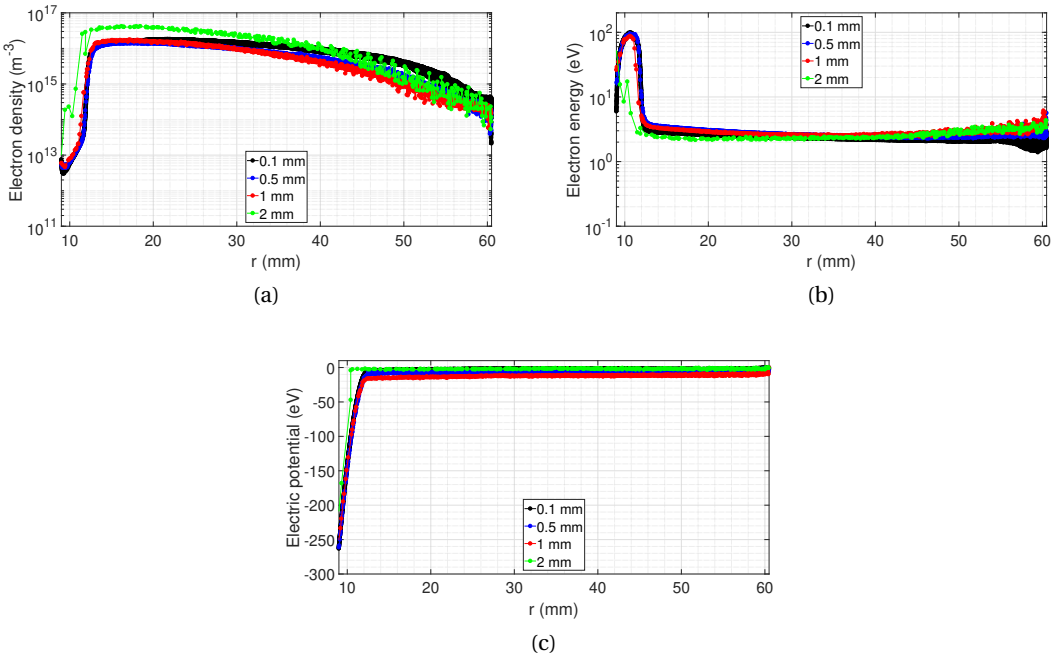

Figure 2.28 – 2D simulations, magnetron, B = 160 Gauss, P_{Ar} = 0.03 mbar, $\Delta t = 5x10^{-12}$ s: radial profiles at t_{sim} = 400 μs of (a) Electron density [m^{-3}] (b) Electron energy [eV] (c) Electric potential [V].

2.3.4 Conclusion on 2D simulations

2D simulations in a slice of the complete 3D model have been performed with periodic boundary conditions in both diode and magnetron configurations to study the influence of the mesh resolution and of the simulation time step on the global and local plasma parameters. 2D diode simulations have not evidenced significant differences in terms of global cathode voltage evolution and radial profiles of local plasma parameters for a simulation time step $\Delta t = 5x10^{-12}$ s and for mesh sizes of 0.1, 0.5 and 1 mm, while a mesh size of 2 mm resulted in a noisy and unstable cathode voltage evolution, which can be attributed to a lack of cathode sheath resolution. 2D magnetron simulations have shown that cell hopping can occur for a too large simulation time step $\Delta t = 2x10^{-11}$ s combined with a too small mesh size Δx = 0.1 mm, while an appropriate choice of time step ($\Delta t = 5x10^{-12}$ s) has revealed almost no differences in terms of global and local plasma parameters for mesh sizes spanning from 0.1 to 1 mm. Similarly to the diode simulations, a mesh size of 2 mm has demonstrated an unstable behaviour due to a lack of cathode sheath resolution, independently from the chosen simulation time step.
Finally, 2D diode and magnetron simulations have overestimated electron density peaks and underestimated cathode voltages compared with 3D simulations, which has been explained by the 2D assumption of an infinite axial plasma not accounting for end-losses.

2.4 Conclusion

This chapter has been focused on the assessment of physical and numerical parameters suited to proper DC plasma discharge modelling with the PICMC module of a numerical code [4].
3D simulation results have emphasized the importance of IISEE parameters on plasma discharge current and voltage, while showing that a yield γ_{IISEE} = 0.13 and a Gaussian energy distribution function are suited for modelling the secondary electron emission induced by argon ion bombardment on niobium. A Langmuir probe has been designed to measure local plasma parameters. However, the absolute comparison of measured local plasma parameters with the simulated ones has been difficult due to the perturbation of the low discharge power plasma induced by the probe operation and to the lack of a Langmuir probe theory fully accounting for the presence of a magnetic field.
2D simulations have revealed the importance of choosing appropriate numerical constraints in terms of simulation time steps and mesh sizes. Discharge voltage divergence or instability has been explained case by case, while a stable discharge voltage time evolution has been correlated to almost identical profiles of local plasma parameters for a simulation time step $\Delta t = 5x10^{-12}$ s and for a wide range of mesh sizes (from 0.1 mm to 1 mm) in both diode and magnetron configurations.
Finally, the large size and poor plasma confinement of the experimental system have resulted in long simulation computing times. Furthermore, the accessible ranges of process pressures in the current diode and magnetron configurations are characterised by low deposition rates. This motivates the change of sputtering source in the following chapter to validate DSMC simulations of sputtered atoms transport using PICMC plasma modelling results as inputs.

3 DSMC simulations: validation with a hollow cathode magnetron source

The previous chapter aimed at validating plasma simulations performed with a PICMC code by comparing the macroscopic and local simulation plasma parameters with the experimental ones. In this chapter, we focus on the validation of sputtered neutral atoms transport simulations using the Direct Simulation Monte Carlo (DSMC) module of the same numerical code[4], such that simulated profiles of sputtered niobium deposition rates can be compared with experimentally measured ones. The previously described niobium rod cathode is substituted with a compact hollow cathode magnetron (HCM) sputtering source. With this source, plasma confinement is enhanced and larger deposition rates are achieved due to lower working pressures while keeping reasonably low discharge power.

We first present in section 3.1 the new sputtering source configuration including description of its conceptual design and of its magnetic assembly. Then in section 3.2, plasma simulations operated at the same discharge power of 10 W but at four different pressures are used to extract quantitative niobium sputtering profiles from the cathode. These sputtering profiles are taken as inputs for DSMC simulations in section 3.3, for which deposition rates are finally compared with experimental data. The process pressure is taken here as the parameter of study, since collisions between sputtered atoms and process gas atoms are the key mechanism for accurate modelling of sputtered atoms transport.

This validation is an essential step towards building a trustworthy, *ab initio* methodology for the modelling of thin film coatings.

3.1 Experimental system

The coaxial cylindrical plasma source configuration used in the previous chapter was chosen for plasma simulation validation, but has some strong limitations for coating applications:

- In the DC diode configuration, working pressures are intrinsically high (10^{-1} mbar range) such that sputtered atoms experience many collisions with the process gas atoms. Therefore, the majority of sputtered atoms is redeposited on the cathode rather than onto the substrate, resulting in low deposition rates.
- In the DC magnetron configuration of chapter 2, electron end-losses at the anode extremities lead to a poor plasma confinement requiring large working pressures (10^{-2} mbar range) compared to classical magnetron operation (10^{-3} mbar range) resulting in limited deposition rates, similarly to the DC diode configuration. Furthermore, the need of modelling the full vacuum chamber geometry to properly account for the plasma end-losses induces long simulation times of the order of several weeks to months.

Validation of neutral atoms transport simulations requires comparisons of simulated deposition rates with experimental ones for the same parameters. To increase deposition rates and keep reasonably short experimental coating times (less than a day), the niobium rod cathode is replaced by a compact hollow cathode magnetron (HCM), which is characterized by low working pressures and high deposition rates even at low discharge power densities achievable by simulations.

3.1.1 Design of the hollow cathode magnetron source

The concept of the hollow cathode magnetron plasma source relies on the strong electron confinement obtained by combining traditional magnetron operation (see section 1.1.4) with an additional efficient electrostatic trap (hollow cathode effect, [14, Chapter 14.4]). Designs of HCM sources for planar coating applications have been described in [71, 72, 73].

Our design[1] is presented in details in figure 3.1 and differs from designs of [71, 72, 73] both in the magnet assembly and in its rotational symmetry, which is suited for coatings of cylindrical objects such as vacuum tubes or RF cavities. The side disks of the negatively biased cathode act as electrostatic mirrors for electrons, which follow cycloidal trajectories along the magnetic flux lines (see figure 3.1c) along with an azimuthal $\mathbf{E}\times\mathbf{B}$ drift motion around the cathode central cylinder, thus enhancing plasma confinement.

[1] The initial design of this specific source is from Guillaume Rosaz, CERN-TE/VSC/SCC. The author of this manuscript assisted the design with the numerical simulations and performed the experimental coatings presented thereafter.

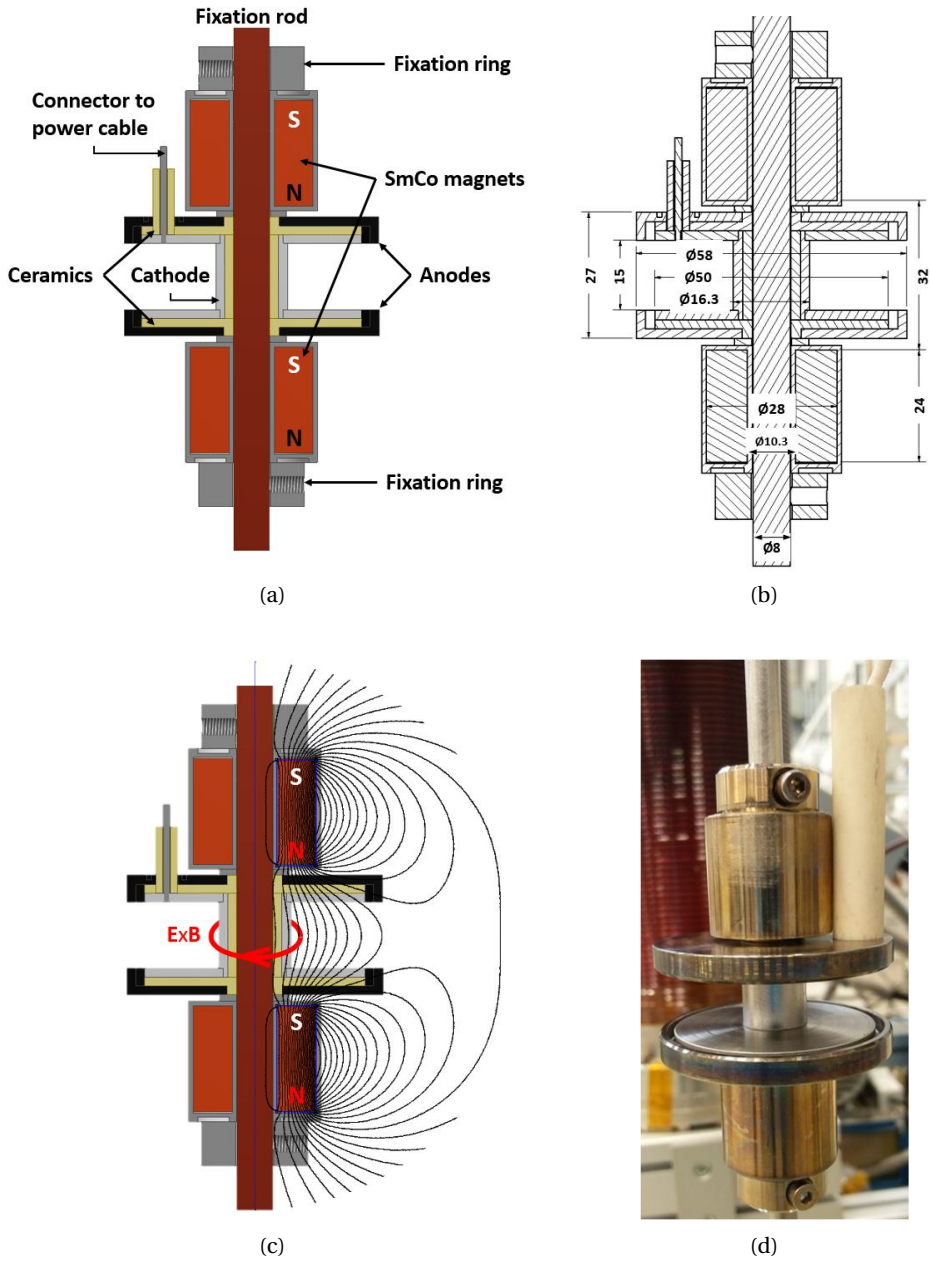

Figure 3.1 – Hollow cathode magnetron plasma source: (a) Design with elements (b) Schematics with relevant dimensions (in mm) (c) Overlaid magnetic flux lines (black) with magnets' poles and **E**×**B** drift drawn in perspective (d) Picture of the experimental source. Schematics are half-views with azimuthal symmetry around the vertical axis.

As seen in figure 3.2, the HCM plasma source replaces the niobium rod cathode from chapter 2 in the same experimental system (figure 2.3). It is attached to a stainless steel rod and vertically centred at mid-height inside the octagonal substrate. The cathode is insulated by ceramics (alumina Al_2O_3) from the grounded rod and from the anodes, and connected to a vacuum power feedthrough by a copper wire insulated with ceramic beads. Additionally, a metal sample is vertically attached on one face of the octagonal substrate for *ex-situ* X-Ray Fluorescence (XRF) thin film thickness profile measurements. Other elements of the experimental system previously described in chapter 2 including vacuum components, pressure gauges and plasma DC power supply are unchanged.

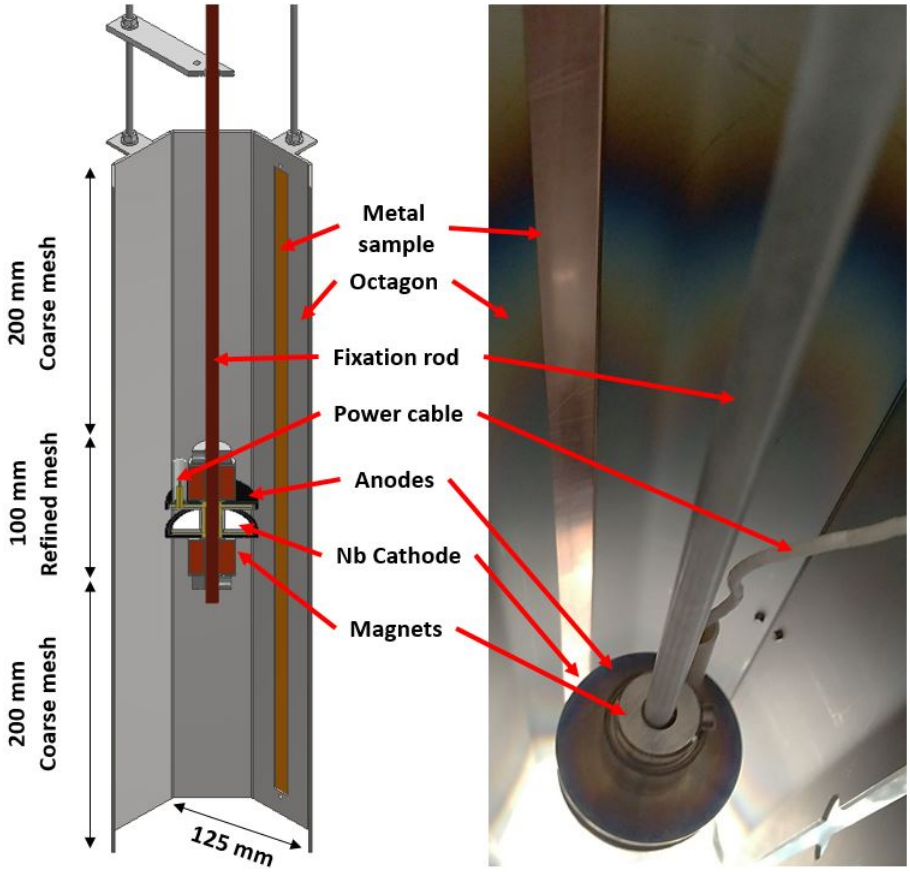

Figure 3.2 – Experimental system with hollow cathode magnetron sputtering source. Left: schematic half-view with axial regions of different volume mesh used in the simulations defined in table 3.2, Right: top view picture with metal sample and power cable insulated with ceramic beads.

3.1.2 Permanent magnet characterization

As a preliminary step before plasma simulations, the magnetic field created by the permanent magnet assembly is computed with the Boundary Element Method (BEM) module of the simulation code[45]. The boundary element method assumes that the magnetization of a permanent magnet is homogeneous, and is therefore replaced by an equivalent magnetic surface charge. As such, inputs to the magnetic simulation module are the geometry of the magnet assembly, the relative permeabilities μ_r of the different domains (vacuum and magnets) and the magnetic remanences B_r([T], equivalent to [N.A^{-1}.m^{-1}]) of the magnet poles. The relative permeability of an element is defined as $\mu_r = \frac{\mu}{\mu_0}$, where μ [N.A^{-2}] is the permeability of the element and μ_0 is the permeability of free space ($4\pi \times 10^{-7}$ [N.A^{-2}]), and the magnetic remanence B_r is the residual magnetic flux density left in a ferromagnetic material when no external magnetic field is applied.

The magnetic configuration described in figure 3.1c is composed of four rings of Samarium-Cobalt (SmCo) permanent magnets, which are assembled in two stacks of two magnets encapsulated in laser welded stainless steel cylindrical cases. Data sheets provided by the manufacturer do not include the relative permeability of the material, but SmCo magnets possess a linear B-H demagnetisation curve that implies $B_r = \mu H_c$, where H_c [A.m^{-1}] is the magnetic coercivity of the ferromagnet, or the intensity of the reverse magnetic field required to drive its magnetization to zero after saturation. It measures the ability of the ferromagnet to resist demagnetisation under an external magnetic field. Knowing B_r and H_c, μ_r can be computed, and these three intrinsic values are summarized in table 3.1 for the SmCo magnets used here (manufacturer denomination: Sm18/25-5 [74]).

Table 3.1 – Samarium/Cobalt Sm18/25-5 permanent magnet data.

B_r [T]	H_c [kA.m^{-1}]	μ_r
0.86 ± 0.03	664 ± 24	1.031 ± 0.073

Validation of the magnetic field simulated with the BEM module is achieved by comparing the radial profile of the computed axial magnetic flux component B_z with results from the FEMM software [75] and with experimental data measured with a gaussmeter as shown in figure 3.3. For simplicity of comparison, only one set of two encapsulated magnet rings is characterized instead of the full magnet assembly.

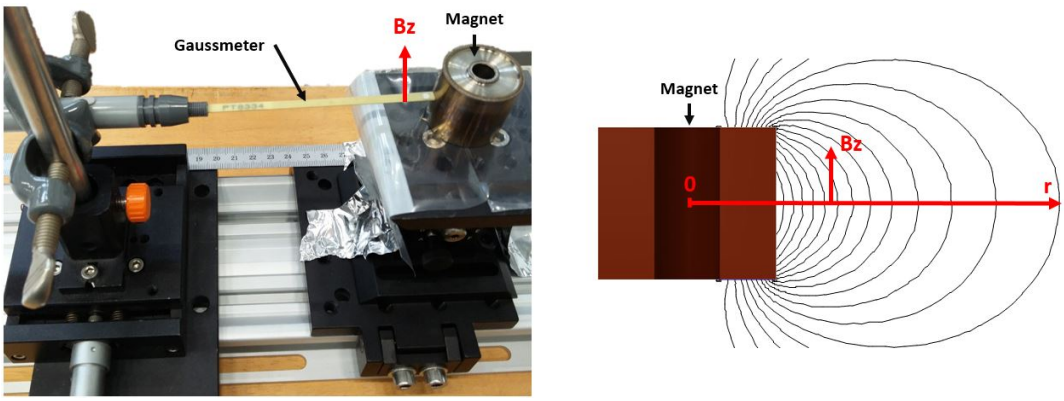

(a) (b)

Figure 3.3 – (a) Picture of the experimental configuration for radial measurement of the magnetic flux density axial component B_z with a Gaussmeter (b) Side view of the magnetic flux lines (black) simulated with FEMM axisymmetric model and horizontal red line corresponding to horizontal axis of figure 3.4.

Comparison of simulated and experimental B_z on the horizontal red line of figure 3.3(b) is presented in figure 3.4 as a function of the radial distance to the axis of the 30 mm diameter magnet. The experimental measurements start at a radius of 18 mm because the measuring element of the gaussmeter probe is 3 mm away from the probe physical edge.

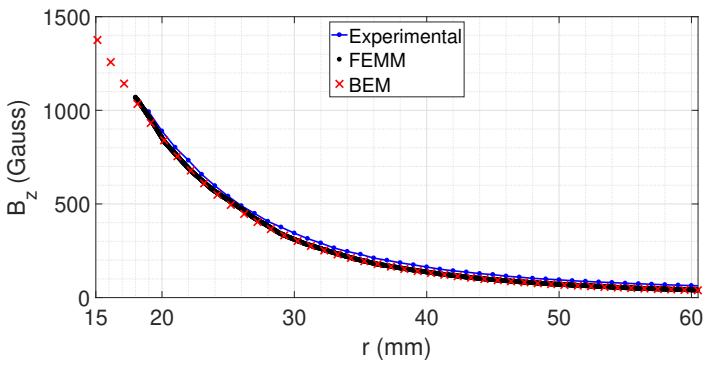

Figure 3.4 – Comparison of radial profiles of the magnetic flux density axial component B_z (Gauss) from BEM and FEMM simulations with experiment. Radial position corresponds to the distance from the axis of the 30 mm diameter magnet.

A good match is obtained between the two different simulation tools. The experimental measurement presents the same shape as the simulations, with a constant deviation of ~ 20 Gauss. This discrepancy is small compared with the measured maximum field value of 1066 Gauss at r = 18 mm, and can be attributed to both the positioning accuracy and instrumental error of the gaussmeter, and to the uncertainty of the magnetic remanence B_r given by the manufacturer and used in the simulations (see table 3.1). The magnetic field computed by the

BEM module can therefore be trusted to accurately model the experimental field within its measurement error. This validation has been done for a single component of the field, but the full 3D BEM computation of the magnetic field is taken as input in the plasma simulations.

3.2 Plasma simulations and sputtering profile extraction

3.2.1 Plasma simulations

Four plasma simulations are performed at the same discharge power $P_{discharge}$ = 10 W and at different pressures P_{Ar} = [2x10^{-3}, 5x10^{-3}, 1x10^{-2}, 5x10^{-2}] mbar. This range of pressure is chosen to validate the impact of sputtered atoms collisions with process gas atoms on thin film deposition rates in subsequent neutral atoms transport simulations (section 3.3). The simulation volume presented in chapter 2 is restricted here to the inside of the octagonal substrate (500 mm height, figure 3.2), as the plasma generated by the HCM source is confined in the central part of the substrate and does not exhibit axial electron end-losses such as those described in section 2.2.4. Simulation parameters are listed in table 3.2. Niobium ionization is neglected due to the low degree of ionization in the discharge combined with the low densities of sputtered niobium atoms compared with the density of process gas argon atoms. Volume reactions were described in section 1.2.2.3.

Table 3.2 – Physical and numerical simulation parameters for the Hollow Cathode Magnetron plasma modelling.

Domain size in XYZ [mm^3]	125 x 125 x 500
Mesh size in the cathode region [mm^3]	1 x 1 x 0.5
Mesh size in the rest of the domain [mm^3]	1 x 1 x 2
CPU used per run (cores)	96
Argon pressure [mbar]	[2x10^{-3}, 5x10^{-3}, 1x10^{-2}, 5x10^{-2}]
Scale factor Ar	[2x10^9, 4x10^9, 8x10^9, 4x10^{10}]
Species	Ar, Ar$^+$, e$^-$, Nb
Discharge power [W]	10
Time step [s]	5x10^{-12}
Scale factor Ar$^+$, e$^-$	10^5
Initial density Ar$^+$, e$^-$ [m^{-3}]	5x10^{12}
Simulation time	several weeks, depending on the pressure
Magnetic field	Computed by the BEM module
γ_{IISEE}	0.13
IISE energy distribution	Gaussian
IISE angular distribution	cosine
Electron capture probability on physical surfaces	100 %
Sputtering yield	According to Yamamura's analytical formula (Appendix A)

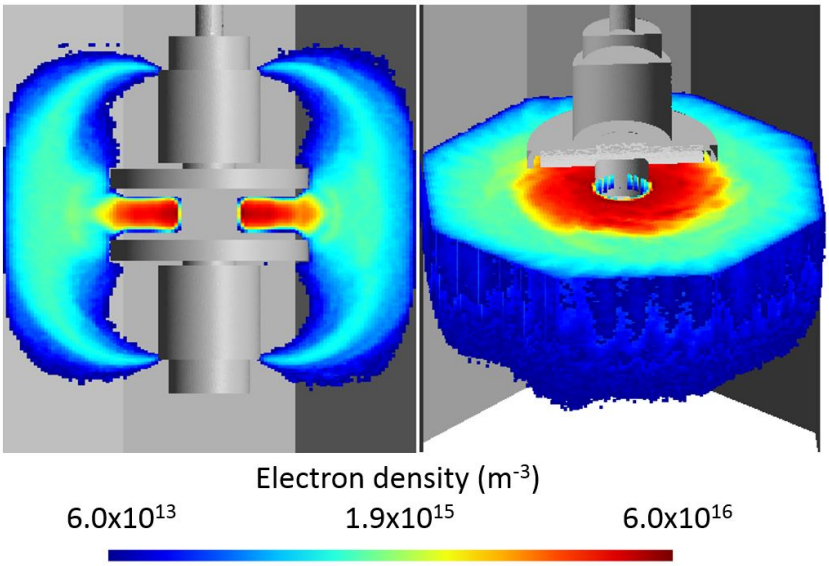

(a)

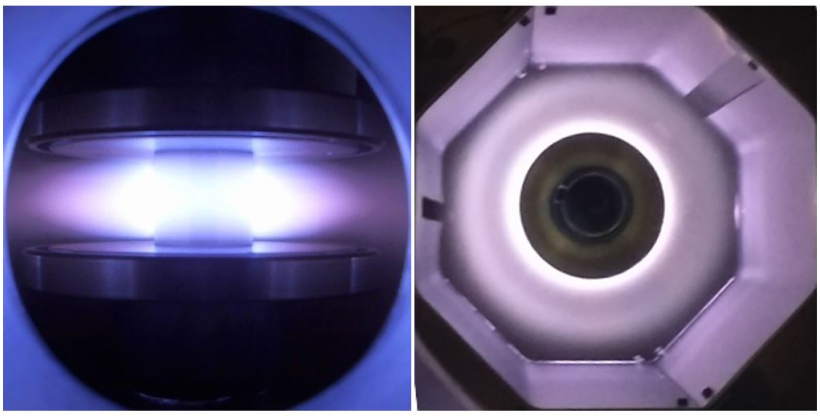

(b)

Figure 3.5 – (a) Cross-sections of simulated electron densities in the plasma source region of the simulation domain at P_{Ar} = 1x10^{-2} mbar, t_{sim} = 80 μs (b) Corresponding photographs of the plasma discharge from the cathode side (in a similar system featuring a side viewport) and from the chamber bottom viewport.

Examples of simulated electron densities at P_{Ar} = 1x10^{-2} mbar are shown in figure 3.5(a) along with photographs taken during the discharge in figure 3.5(b). Figure 3.5 confirms that the plasma is confined around the HCM source both experimentally and from simulations, thus justifying the simulation volume reduction to the inside of the octagonal substrate. The electron density displayed in figure 3.5(a) shows that electrons follow the magnetic flux lines represented in figure 3.1(c), while the maximum electron density lies in between the cathode disks which fulfill their role of electrostatic mirrors.

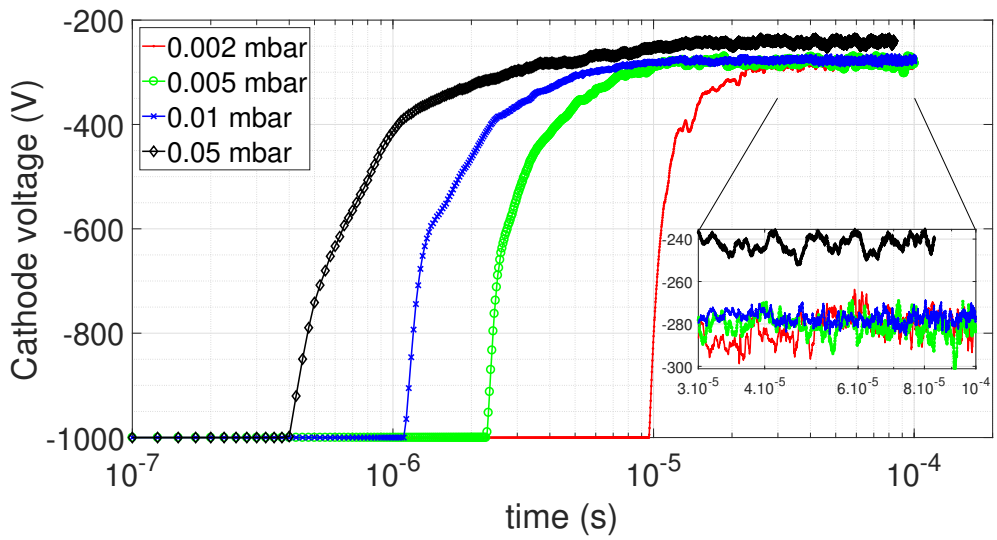

Figure 3.6 – Time evolution of simulated cathode voltage for all process pressures, with inset focused between t_{sim} = 30 μs and t_{sim} = 100 μs.

To assess the plasma simulation validity, we compare discharge voltages and currents between simulations and experiments as a function of the process pressure, as it was done in chapter 2. The evolution of the cathode voltage during each simulation is presented in figure 3.6. This figure shows that an increase in pressure induces a shorter plasma ignition time[2]. This trend with pressure stems from the fact that initial electrons experience more ionization collisions at higher pressure, leading to a faster gas breakdown. Yet, steady state simulated voltage values are very close to each other in the four cases, as can be seen in the inset of figure 3.6.

In table 3.3, we compare the simulated steady state discharge voltage and current to their experimental counterparts at the same discharge power P_{dis} = 10 W. Simulated values are time-averages of the curves presented in figure 3.6 between t_{sim} = 40 μs and t_{sim} = 80 μs, with their standard deviation computed over this time span. Experimental values are obtained from the power supply display for each coating after a few minutes of plasma discharge. At this time, after the initial transient due to the removal of the cathode oxide layer, values of current and voltage are stable for the entire coating process[3].

[2]Defined as the simulation time corresponding to the start of cathode voltage decrease, which is also equivalent to the simulation time at which the setpoint in discharge power is reached.

[3]Surface oxidation of the cathode due to air exposure before pump-down modifies its ion-induced secondary electron emission yield[76]. As such, stable I/V discharge values are experimentally reached once the cathode oxide layer has been removed by a few minutes of sputter cleaning, when the cathode surface is composed of pure niobium.

Table 3.3 – Comparison of experimental and simulated voltages and currents in the Hollow Cathode Magnetron system at different pressures and same discharge power P_{dis} = 10 W.

Pressure [mbar]	Voltage [V]		Current [mA]	
	Measurement[1]	Simulation[2]	Measurement[1]	Simulation[2]
2x10^{-3}	330 ± 10	280 ± 5.6	30 ± 1	35.7 ± 0.8
5x10^{-3}	282 ± 5	282 ± 4.9	38 ± 1	35.5 ± 0.6
1x10^{-2}	250 ± 5	277 ± 2.7	39 ± 1	36 ± 0.4
5x10^{-2}	204 ± 8	242 ± 3.5	52 ± 1	41.3 ± 0.6

[1] Taken from power supply display after a few minutes of plasma operation.
[2] Simulation values are time-averages and standard deviations of voltages shown in figure 3.6 between t_{sim} = 40 μs and t_{sim} = 80 μs, and of their equivalent simulated current.

Simulation and experiment values compared in table 3.3 are close to each other - within 40-50 Volts in the worst case at P_{Ar} = 2x10^{-3} mbar. However, the experimental trend presents a decreasing discharge voltage with an increasing pressure, while this trend is almost lost in the simulations. Indeed, the three lower pressure simulations have almost identical discharge I/V values, while the highest pressure simulation is overestimating the corresponding experimental discharge voltage by 38 V. Even though we have no definitive explanation for this loss of pressure influence in the simulations, it may be due to the following points:

- Electron densities in the high 10^{16} m^{-3} range such as visible in figure 3.5(a) may require a more refined mesh in the high density plasma region and in the cathode sheath in order to better resolve the electric potential fluctuations at the scale of the Debye length, yet at the expense of computation time. The presented simulations are stable in terms of discharge I/V values, but a lack of cathode sheath resolution could influence the absolute cathode voltage and currents. This possibility is further supported by the fact that when charged particle densities are low during the plasma ignition, the discharge breakdown time is correctly influenced by the argon pressure (figure 3.6) until high plasma densities are reached in the steady state (after 30 μs). A more refined mesh is not feasible in this configuration because of computational limitations.

- As mentioned in section 1.1.1.4, we do not include secondary electron emission under metastable argon atoms or photons bombardment on the cathode. As the HCM source is characterised by an enhanced plasma confinement, limiting the production of secondary electrons exclusively to ion bombardment in the simulations, as was done in the previous chapter, may lead to a misevaluation of experimental I/V discharge values.

- As the experimental cathode is not cooled, cathode heating caused by ion bombardment could result in local gas rarefaction at its vicinity, which in turn could influence the discharge voltage and current [77]. This would not be reproduced by the simulations in

which the cathode is assumed to be at room temperature, since its actual temperature is unknown. This effect could be accounted for by computing the neutral argon density in a DSMC simulation with the real cathode temperature as a first step, and by using this density profile in the plasma simulation as a second step. Experimental measurement of the cathode temperature with a thermocouple is not directly possible due to the cathode negative bias during operation. Indirect temperature measurements of the cathode with e.g. a pyrometer could be feasible, but would require proper calibration and a direct line of sight towards the cathode, which is not possible in the current experimental system.

- Each experimental coating at a given pressure lasted for several hours, as will be detailed in table 3.6. Subsequent erosion of the cathode surface could be responsible for I/V values not fully matched by simulations, as the local magnetic field at the cathode surface could slightly differ from one coating to the other and modify the local plasma density. This is not taken into account in the present simulations which assume an "ideal" cathode geometry, but will be further discussed in section C in another coating configuration.

3.2.2 Extraction of niobium sputtering profiles from the plasma simulations

Simulations of sputtered atoms transport with the Direct Simulation Monte Carlo (DSMC) module need as inputs both the spatially resolved profile of niobium atoms sputtered from the cathode and the production rate of these sputtered atoms. In each plasma simulation, a reaction describing niobium sputtering from the cathode surface under argon ion bombardment is implemented according to Yamamura's empirical formula [6] (section 1.1.2) and based on the Matlab script listed in Appendix A. This reaction quantitatively generates 3D sputtered niobium profiles based on the energy and number of bombarding ions directly in the plasma simulation and with a spatial resolution at the cathode surface, thus providing the required inputs for DSMC simulations. In order to remove time and space variations due to plasma inhomogeneities, spatial profiles and production rates for each plasma simulation are averaged over the same simulation time interval corresponding to stable discharge I/V values. As the plasma simulation at P_{Ar} = 5x10^{-2} mbar takes a significantly longer computational time than the other lower pressures due to its larger number of computed collisions, its niobium production rate is time-averaged between t_{sim} = 69 μs and t_{sim} = 84 μs, while for the other three pressures it is time-averaged between t_{sim} = 85 μs and t_{sim} = 100 μs. This change of time-averaging interval has no impact on the validity of results, since the inset of figure 3.6 showed that all simulations are stable in terms of discharge I/V after t_{sim} = 30 μs.
An example of 3D time-averaged sputtered niobium profile is shown in figure 3.7(a) for P_{Ar} = 1x10^{-2} mbar, and sputtering profiles on the cathode central cylinder and side disks averaged over the azimuthal direction are compared respectively in figure 3.7(b) and 3.7(c) for all simulated pressures.

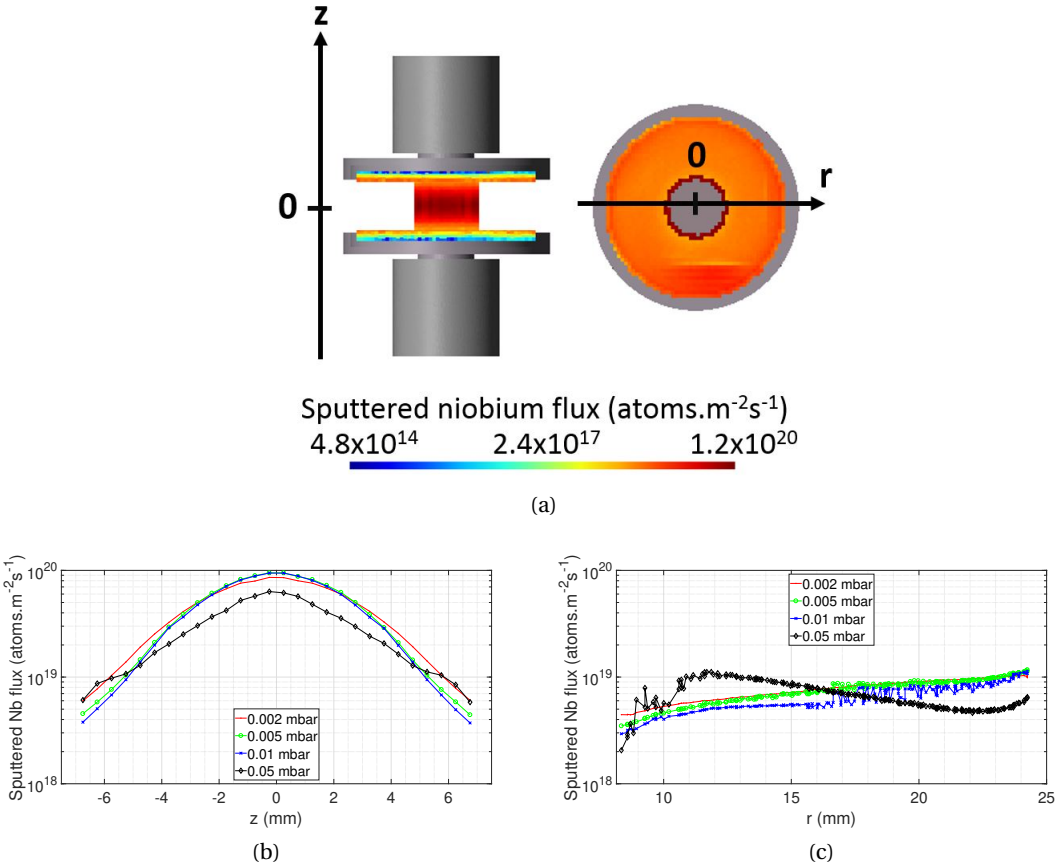

Figure 3.7 – (a) Example of a 3D view of the simulated sputtered niobium profile at P_{Ar} = 1x10^{-2} mbar, time-averaged between t_{sim} = 85 μs and t_{sim} = 100 μs. Left: side view of the sputtering profile on the central cylinder, right: top view of the sputtering profile on one side disk. Comparison of sputtered niobium profiles for all pressures averaged over azimuthal direction: (b) on the cathode central cylinder (c) on the cathode side disks.

Figures 3.7(b) and 3.7(c) show that for all pressures, most of the niobium emission occurs on the cathode central cylinder rather than on the side disks. As can be seen in figure 3.7b, the sputtering profile shape on the central cathode cylinder is almost independent from the pressure, while small variations in absolute values are noticeable. Figure 3.7c shows that at P_{Ar} = 5x10^{-2} mbar, the sputtered niobium profile shape on the cathode side disks differs from the ones at other pressures, but its absolute values are still one order of magnitude below the central cathode cylinder emission peak at the same pressure (figure 3.7(b)). 2D profiles shown in figures 3.7(b) and 3.7(c) are only presented here for the purpose of discussion, but DSMC simulations actually take the full 3D profiles such as the one of figure 3.7(a) as inputs. In addition to these 3D sputtered niobium profiles, the production rates of niobium atoms sputtered from the cathode are also given by each plasma simulation. Table 3.4 lists the time-averaged production rates of sputtered niobium atoms at the cathode for the four different pressures, without including re-deposition.

Table 3.4 – Time-averaged production rates of sputtered niobium atoms extracted from the plasma simulations at the four different pressures, without including re-deposition.

Pressure [mbar]	time-averaging simulation interval [μs]	Sputtered Nb production rate [sccm]
2x10^{-3}	85-100	0.1312
5x10^{-3}	85-100	0.1301
1x10^{-2}	85-100	0.1208
5x10^{-2}	69-84	0.0956

It can be seen in table 3.4 that the niobium production rate decreases when the pressure increases. It is most noticeable by comparing rates at P_{Ar} = 2x10^{-3} mbar and P_{Ar} = 5x10^{-2} mbar, since the production rate of the latter is ~ 27 % smaller than the one of the former. This was already visible in figure 3.7(b). Indeed, as pressure increases, the bombarding ion energy decreases due to lower cathode voltage and more collisions with the neutrals in the cathode sheath, thus decreasing the sputtering yield. This will be further discussed in section 4.1.1 and Appendix B.

3.3 Comparison of simulated and experimental deposition rates

3.3.1 Simulation model and parameters

Four DSMC neutral transport simulations corresponding to the four process pressures are performed with the numerical parameters listed in table 3.5. They only take into account neutral argon and niobium atoms, whose volume collision reactions were described in section 1.2.3. In addition, specular boundary conditions are defined at the octagonal substrate open ends, such that argon atoms are specularly reflected back into the simulation volume and process gas pressure is not depleted during the simulation. The initial angular distribution of sputtered niobium atoms is chosen as a power cosine law of exponent 0.5, based on the discussion of section 1.1.2. The impact of this parameter will be further studied in section 4.2.3. Other relevant simulation parameters such as domain size, mesh resolution and CPU usage per run are kept identical for each simulation case to those listed in table 3.2.

Table 3.5 – Physical and numerical simulation parameters for the HCM transport modelling.

Species	Ar, Nb
Time step [s]	10^{-7}
Scale factor Nb	$8x10^5$
Simulation time	~ a week
3D Nb sputtering flux profile	Taken from the plasma simulations
Nb sputtering rate [sccm]	Listed in table 3.4 according to pressure
Sputtered Nb energy distribution	Thompson with E_b = 7.59 eV
Sputtered Nb angular distribution	Undercosine with exponent 0.5

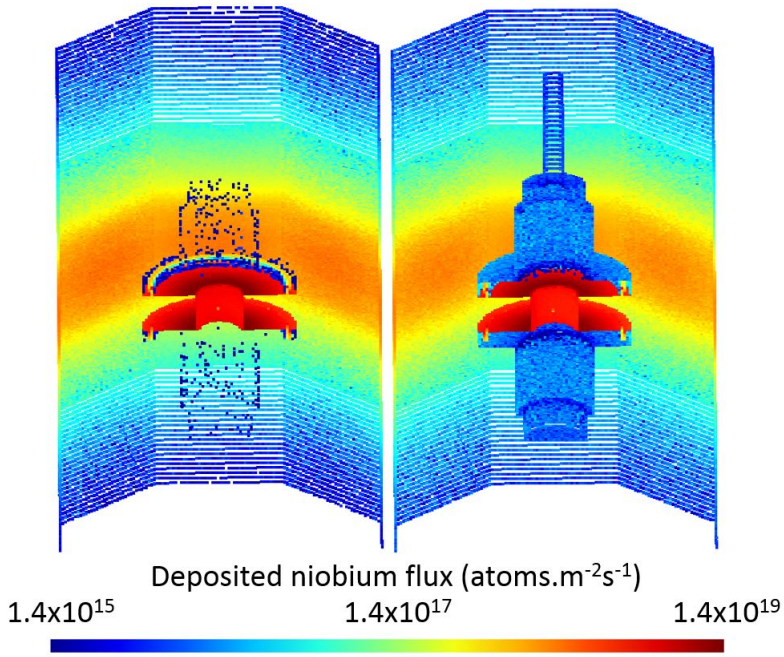

Figure 3.8 – 3D half-views of the simulated deposited niobium fluxes at P_{Ar} = $2x10^{-3}$ mbar (left) and $1x10^{-2}$ mbar (right), t_{sim} = 100 ms. The change of vertical mesh size resolution described in table 3.2 is visible.

Examples of simulated deposited niobium fluxes [atoms.m^{-2}.s^{-1}] are given for two different pressures in figure 3.8. The impact of the pressure is visible since at $2x10^{-3}$ mbar (left), fewer atoms are deposited on the magnet casings and on the fixation rod than at $1x10^{-2}$ mbar (right), due to fewer collisions with the process gas atoms. Figure 3.8 shows that redeposition on the cathode predominates over deposition onto the substrate independently of the pressure. This is rather due to the cathode geometry, as deposition fluxes on the cathode are in the 10^{19} atoms.m^{-2}.s^{-1} range for both pressure cases, which is one order of magnitude above deposition fluxes on the substrate.

For each simulation, 3D niobium deposition profiles such as the ones shown in figure 3.8 are time-averaged between t_{sim} = 80 ms and t_{sim} = 100 ms for data smoothing, once simulated deposition fluxes are stable on all elements. Then, each time-averaged simulated deposition flux is extracted at the location corresponding to the one of the experimental metal sample (see figure 3.2) and is converted to a deposition rate by using equation 1.20, which assumes that the deposited thin film has the same density as bulk niobium. The validity of this assumption as a function of film porosity is not questioned here, but will be discussed in section 4.2.4.3.

3.3.2 Experimental coatings

At first, copper strips were used as samples for the experimental deposition rate measurements, which consistently resulted in more or less pronounced film delamination. This was attributed to the poor quality of the raw copper sheet from which samples were cut, whose surface state could not be sufficiently improved by chemical cleaning[4]. Therefore, 316 LN stainless steel samples were chosen for the present study since the substrate material does not have an influence on the deposition rates. None of the coated stainless steel samples evidenced delamination. The coating parameters for each pressure are listed in table 3.6.

Table 3.6 – HCM: experimental coating parameters. StSt stands for stainless steel, and Cu stands for copper samples.

Coating number	Pressure [mbar]	Sample Material	Coating time [hours]	Delamination
1	$2x10^{-3}$	StSt	6	none
2	$5x10^{-3}$	Cu	6	extended
3	$5x10^{-3}$	Cu	6	mild
4	$5x10^{-3}$	StSt	6	none
5	$1x10^{-2}$	StSt	12	none
6	$5x10^{-2}$	StSt	18	none

In section 1.1.6.3, the accuracy of the X-Ray fluorescence (XRF) instrument for measurements of niobium thin film thicknesses on copper substrates was discussed and compared with Focused Ion Beam/Scanning Electron Microscopy measurements, yielding an instrumental uncertainty of the XRF device within ± 10 %. As we now use a routine calibrated for niobium films deposited on stainless steel substrates, the precision of XRF measurements has to be reassessed. Figure 3.9 compares deposition rate profiles measured by XRF of partially delaminated niobium films on copper (coatings n° 2 and 3 of table 3.6) and their equivalent on stainless steel (coating n° 4 of the same table) at P_{Ar} = $5x10^{-3}$ mbar.

[4]Chemical cleaning of copper elements for Ultra High Vacuum applications at CERN consists in degreasing the element by immersion in an ultrasonic bath filled with detergent, and in the removal of the oxide layer with hydrochloric acid before passivation with chromic acid. The piece is finally rinsed with demineralised water and sprayed with ethanol for faster drying under a flow of nitrogen or compressed air.

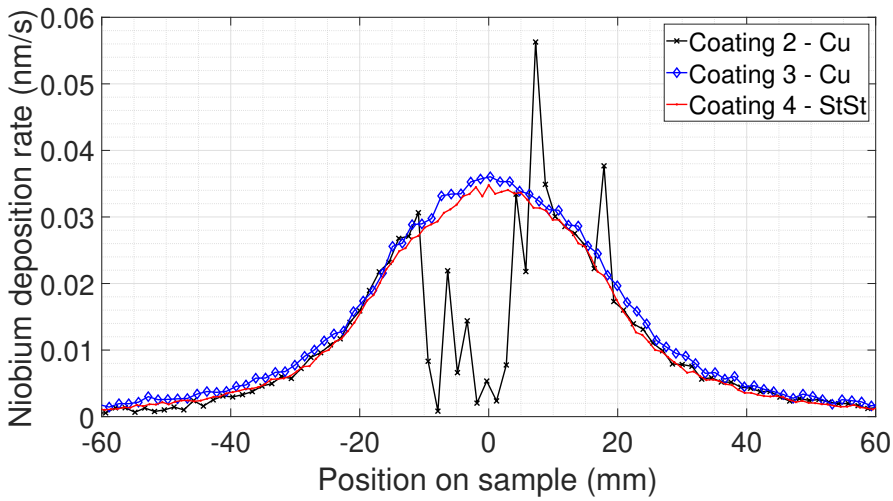

Figure 3.9 – Comparison of niobium deposition rates [nm.s^{-1}] on copper and stainless steel samples at P_{Ar} = 5x10^{-3} mbar. Coating numbers are referenced in table 3.6. The origin of the horizontal axis corresponds to the middle of the octagonal substrate in the vertical direction (see figure 3.2).

Figure 3.9 shows that deposition profiles measured for coating n° 3 (copper sample, mildly delaminated) and coating n° 4 (stainless steel sample, no delamination) match quite well, and are also in agreement with coating n° 2 (copper sample, extended delamination) outside of the central region dominated by thin film delamination (-10 to +20 mm). This agreement supports the use of XRF as a trustworthy thickness profile measurement tool for niobium thin films deposited on stainless steel.

As listed in table 3.6, the experimental coating times are increased with the process pressure because of the atom transmission efficiency decrease with pressure, such that measured peak thicknesses for all coatings are in the [700-1000] nm range. In this range, the XRF accuracy was compared to SEM measurements in section 1.1.6.3. Therefore, we choose to compare simulated and experimental deposition rate profiles rather than absolute thickness profiles, such that experimental deposition rates are absolute thickness profiles divided by their respective total coating time. Deposition rates are directly comparable between simulations and experiments. Indeed, the simulated ones are converted from deposition fluxes assuming a bulk density of the grown film, while experimental ones measured by XRF rely on routines calibrated on bulk material samples.

3.3.3 Comparison of simulated and experimental deposition rates

Figure 3.10 compares the experimental and simulated deposition rates at the four pressures studied here.

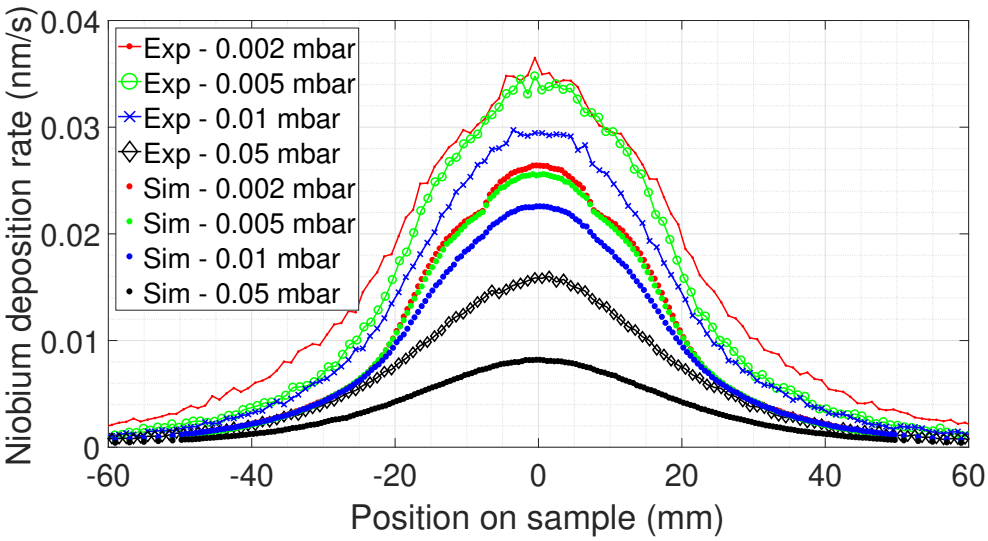

Figure 3.10 – Comparison of experimental and simulated niobium deposition rates [nm.s^{-1}] on stainless steel substrates. The origin of the horizontal axis corresponds to the middle of the octagonal substrate in the vertical direction (see figure 3.2).

It shows that simulated rates follow the same trend with pressure as observed in the experiments: a lower pressure results in less collisions between niobium and argon atoms and a higher deposition rate. From the lowest to the highest pressure, the simulated profiles underestimate the experimental ones by respectively 27.7, 26.5, 24 and 49 %.

To compare deposition rate profile shapes for each pressure, each experimental curve from figure 3.10 is rescaled such that its maximum fits its simulation counterpart[5]. Figure 3.11 show these rescaled experimental deposition rates with the simulated deposition rates from figure 3.10 for each pressure.

[5]In practice, each experimental curve of figure 3.10 is multiplied by $\alpha = \frac{\text{max(simulated deposition rate)}}{\text{max(experimental deposition rate)}}$.

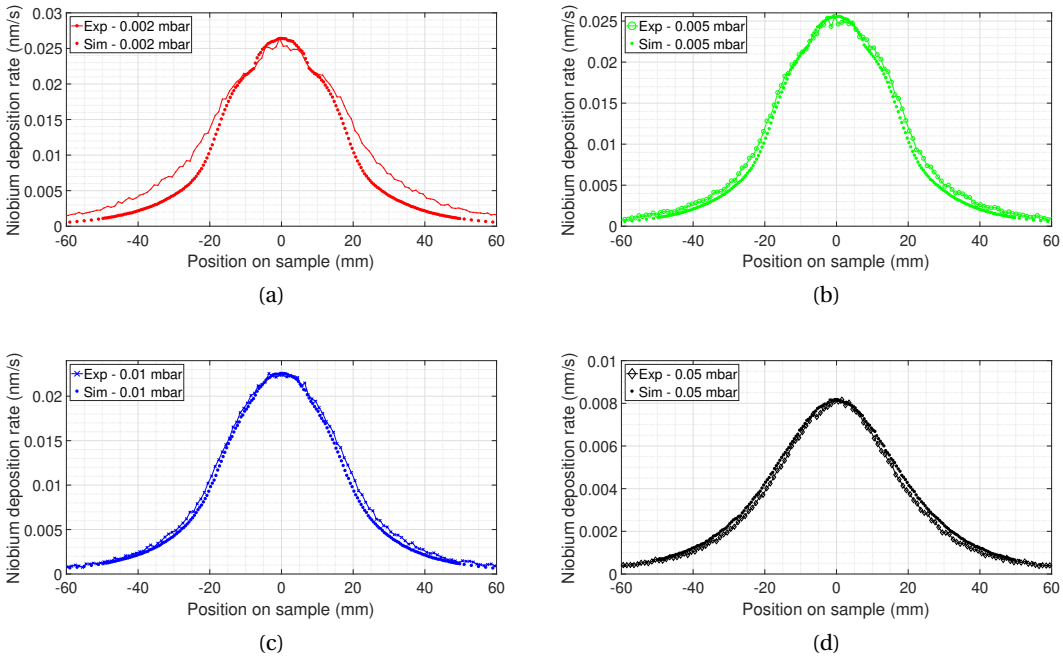

Figure 3.11 – Simulated deposition rates from figure 3.10 with experimental ones rescaled to their respective simulation maximum value. The origin of the position axis corresponds to the middle of the octagonal substrate in the vertical direction. (a) P_{Ar} = 2x10^{-3} mbar (b) P_{Ar} = 5x10^{-3} mbar (c) P_{Ar} = 1x10^{-2} mbar (d) P_{Ar} = 5x10^{-2} mbar.

A discrepancy of profile shape is observed in figure 3.11(a) at P_{Ar} = 2x10^{-3} mbar for which the full width at half maximum (FWHM) of the rescaled experimental profile is larger by ~ 18 % than the simulated one, while shapes at the three other pressures show a good agreement between simulation and experiment. One could also argue that the inflexions in the simulated profiles at ± 7.5 mm at P_{Ar} = 2x10^{-3} mbar and P_{Ar} = 5x10^{-3} mbar are also visible in the experimental profiles. These inflexions are due to the low number of niobium-argon collisions at these two low pressures, such that niobium trajectories are almost ballistic and niobium deposition rate profile shapes are dominated by the system geometry.

Some hypotheses can be suggested to explain the discrepancy between experimental and simulated absolute deposition rates:

- Table 3.3 showed discrepancies between simulated and experimental discharge currents and voltages, which can respectively lead to errors in the sputtering yields and sputtering rates taken from the plasma simulations.
- Although the gas pressure in the experimental chamber is monitored both at the injection point and at the chamber extremity, possible local gas rarefaction effects in the experiments which were mentioned in the discussion of section 3.2.1 could also influence the transport of sputtered niobium atoms from cathode to substrate.

- At last, pressure regulation and cathode centering in the horizontal plane for each experimental coating could slightly deviate from the *ideal case* simulation parameters in terms of nominal pressure and geometry, which would influence the experimental deposition rate profile.

Despite differences in absolute values of 25 % to 50 %, numerical simulations are successful in reproducing the experimental relative deposition rate shapes as a function of pressure. This demonstrates the validity and usefulness of the simulation approach, especially for a complex sputtering source design.

3.4 Conclusions

In this chapter, plasma modelling based on the results of chapter 2 was extended to the simulation of sputtered neutral atoms transport, such that simulated deposition rate profiles could be compared with experiments.
The plasma modelling validity was assessed by comparing simulated discharge currents and voltages with experimental ones, and discrepancies with the experimental values were discussed. Quantitative 3D sputtered niobium profiles were extracted from the plasma simulations and used as inputs for the DSMC module, from which simulated deposition rate profiles on the substrate were obtained. They consistently reproduced the shape and trend with pressure of their experimental counterparts, while underestimating the absolute experimental thickness values by ~ 30%, up to ~ 50% in the worst case.
The predictability of relative experimental profiles is promising for Nb/Cu cavity coating applications because differences of thickness at different substrate positions could be anticipated and mitigated by refining sputtering source design and process parameters. Furthermore, an error in absolute thickness estimate of 50 % in the worst case could be overcome by tuning the experimental coating time, and as such is not deemed as a problem for future applications.

4 Case studies

In the previous chapters, the PICMC/DSMC simulation code has been benchmarked against results from an experimental testbench whose main purpose was the validation of plasma and sputtered atoms transport simulation parameters. The aim of this benchmarking was to gain confidence in simulation results when applied to real coating systems.

In this chapter, we present two cases of application of the simulation code. The first one involves a planar magnetron system for which the scaling of simulation results at low power to realistic experimental coating powers is discussed in terms of target erosion profile and absolute thin film thickness profile accuracy. In the second one, a radiofrequency elliptical cavity is taken as an illustration of the *ab initio* methodology: validity of predicted results in terms of plasma and transport simulations as a function of sputtered atoms initial angular distribution is shown, along with first steps towards thin film morphology simulations using the NASCAM software [5].

4.1 Scalability of simulation results with discharge power

4.1.1 Introduction

Up to this point, simulations and experiments were compared at the same low discharge power (~ 10-20 Watts) for benchmarking purposes. However, coating processes applied to SRF cavities usually require much larger powers (~ a few kW) to achieve higher deposition rates. As these large powers are not directly accessible by simulations because of numerical limitations, the purpose of this section is to question and study the extrapolation of low power simulation results in terms of **target erosion** and **absolute thin film thickness profiles** to realistic coating powers.

During plasma operation, the cathode erosion rate can be written as :

$$
\begin{aligned}
\text{Erosion rate}\,[\mu m/s] &= \alpha[m^2\mu m] \times \text{Sputtered atoms flux}\,[atoms/m^2/s] \\
&= \alpha \times Y(E_{ion}) \times ion_{flux}[ions/m^2/s] \\
&= \frac{\alpha}{eA} \times Y(E_{ion}) \times I_{ions}[A] \\
&= \frac{\alpha}{eA} \times Y(E_{ion}) \times \frac{I_{dis}[A]}{1+\gamma_{IISEE}} \\
&= \frac{\alpha}{eA} \times \frac{1}{1+\gamma_{IISEE}} \times Y(E_{ion}) \times \frac{P_{dis}[W]}{V_{dis}[V]} \\
&\simeq \frac{\alpha}{eA} \times \frac{1}{1+\gamma_{IISEE}} \times \frac{Y(V_{dis}[V])}{V_{dis}[V]} \times P_{dis}[W],
\end{aligned}
\tag{4.1}
$$

where $\alpha = \frac{M_{Nb}}{\rho_{Nb} N_A} = 1.8002 \times 10^{-23}$ [m$^2\mu m$] is a conversion factor (see equation 1.20), $e = 1.6022 \times 10^{-19}$ [C] is the elementary charge, A [m^2] is the current collection surface, $Y(E_{ion})$ is the sputtering yield which depends on the ion energy E_{ion}, I_{dis} is the discharge current and γ_{IISEE} is the ion-induced secondary electron emission yield. The expressions of the second and fourth lines are consistent with our assumptions that only ions are responsible for sputtering and for secondary electron emission respectively.

The ion energy E_{ion} is replaced with the discharge voltage V_{dis} in the last line, which assumes a collisionless cathode sheath typical of low pressure discharges ($< 10^{-2}$ mbar), and neglects the initial ion velocity at the entrance of the cathode sheath with respect to the energy gained in the sheath. This simplification is made here with the sole purpose of introducing an error estimate for the power upscaling before its actual verification. Ion energy distributions on the cathode were theoretically and experimentally analysed depending on the cathode voltage and working pressure in [78, 79, 80], and showed that an accurate description is more complex when ion collisions with neutrals are taken into account in the cathode fall. Nonetheless, we expect that by changing the discharge power (and hence the discharge voltage) while keeping the same working pressure, the real sputtering yield $Y(E_{ion})$ would be lower than its estimate at the cathode voltage but would stay almost independent from the discharge power. This approximation has no impact on the present work since the sputtering yields are self-consistently computed in the plasma simulations based on the impinging ion energies. A summary of the real simulated $Y(E_{ion})$ for all simulations of this work compared with their equivalent $Y(V_{dis})$ is shown in Annex B.

It can be seen from equation 4.1 that increasing the discharge power modifies the erosion rate through a change of A, $Y(V_{dis})$ and V_{dis}. Erosion rate profiles from a low power simulation could be extrapolated to high power coatings provided that some approximations are made, which are reviewed in the following.

The change of ion collection surface A can be neglected when for both simulation and experiment the cathode surface is fully bombarded by ions in the *abnormal* glow discharge operation. This regime used for coating applications implies that the increase in power stems from an increase in current density while keeping constant the bombarded cathode surface

(see section 1.1.1.2).
Under this approximation, the ratio between a high power (HP) real process erosion rate and the equivalent low power (LP) simulation is :

$$\frac{\text{Erosion rate (HP)}}{\text{Erosion rate (LP)}} = \frac{Y(V_{HP})}{V_{HP}} \times \frac{V_{LP}}{Y(V_{LP})} \times \frac{P_{HP}}{P_{LP}}. \tag{4.2}$$

When the coating time t is taken into account, equation 4.2 allows computing the ratio of erosions as:

$$\frac{\text{Erosion (HP)}}{\text{Erosion (LP)}} = \frac{Y(V_{HP})}{V_{HP}} \times \frac{V_{LP}}{Y(V_{LP})} \times \frac{P_{HP}\,t_{HP}}{P_{LP}\,t_{LP}}. \tag{4.3}$$

As can be seen in figure 4.1, the ratio of the sputtering yield over the ion energy varies weakly with the ion energy in the 200-1000 eV range. It exhibits a maximum of 1.28×10^{-3} at $E_{ion} = 333$ eV, and a minimum of 1.01×10^{-3} at $E_{ion} = 1000$ eV for argon ion bombardment on niobium.

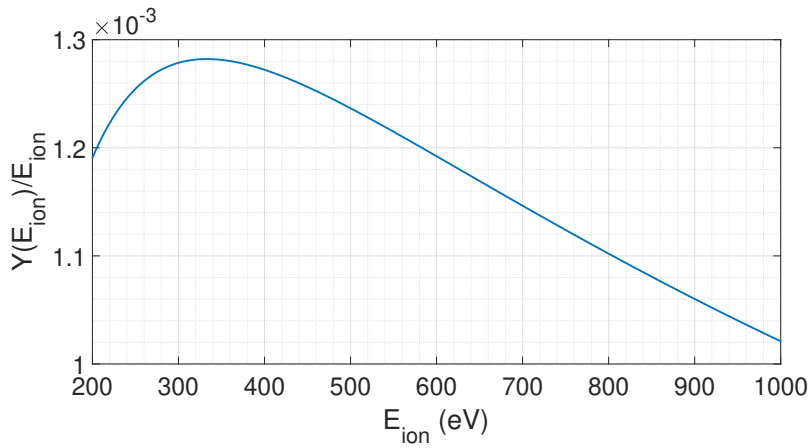

Figure 4.1 – Ratio of sputtering yield divided by ion energy as a function of ion energy, according to Yamamura's formula for argon ion bombardment on niobium. See section 1.1.2.

Therefore, by assuming that only the experimental discharge power is known *a priori*, we can use the low power simulation erosion rate to predict the experimental one with a linear scaling in power and a worst case scenario error of ~ 30%, as according to the modified version of equation 4.3:

$$\frac{\text{Erosion (HP)}}{\text{Erosion (LP)}} \sim \frac{P_{HP}\,t_{HP}}{P_{LP}\,t_{LP}}. \tag{4.4}$$

At last, the validity of the coating profile predicted by the linear scaling of the low power simulation erosion profile relies on the assumption that no gas rarefaction induced by thermal effects occurs in the high power discharge.
To verify equation 4.4, a planar magnetron source is used in the following to produce several coatings at different powers while keeping the product *Power* × *Coating time* constant. Provided that our assumptions are correct, cathode erosion and thickness profiles for the different coating powers should be comparable. Contrarily to the plasma sources presented in the previous chapters, this source is water-cooled during operation, which allows high power processes without excessive target heating and subsequent gas rarefaction. First, the system configuration including geometry and magnet assembly is described. Then, cathode erosion profiles and niobium thin film thickness profiles on copper samples are experimentally measured for different discharge powers and compared with low power simulation results.

4.1.2 Experimental system: planar magnetron

4.1.2.1 Geometry

The experimental setup consists in a 430 mm high, 150 mm diameter vacuum chamber. The planar magnetron source is mounted at its bottom as shown in figure 4.2(a), and is made of three planar magnetron sources tilted by 15° with respect to the horizontal plane. During operation, only one of the three water-cooled sources is used, while the other two are covered by grounded disks and their magnets are removed. The cathode consists of a 50 mm diameter, 2 mm thick niobium disk onto which a grounded guard ring anode of 46 mm inner diameter is mounted with a gap of 0.5 mm. A copper strip of 80 mm length, 10 mm width and 1 mm thickness is positioned at 50 mm above the cathode disk for *ex situ* thin film thickness measurements, as can be seen in figure 4.2.

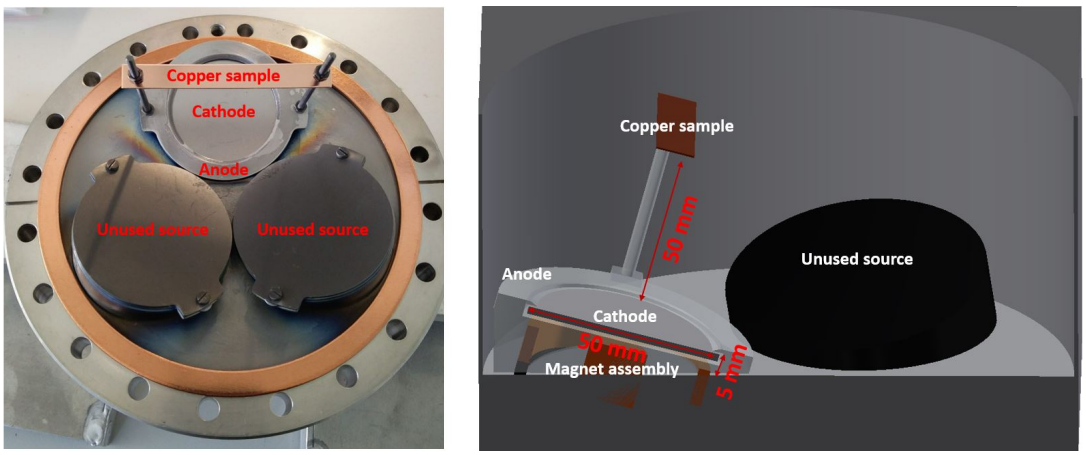

(a) (b)

Figure 4.2 – (a) Picture of the triple planar magnetron system before coating (b) Schematic half view of the system with its main elements and dimensions.

4.1.2.2 Permanent magnet characterization

The magnet assembly positioned at 5 mm below the cathode surface provides a balanced magnetic configuration described in figure 4.3. The inner and outer magnet rings are made of Samarium-Cobalt (see characteristics in table 4.1), while the yoke is made of iron.

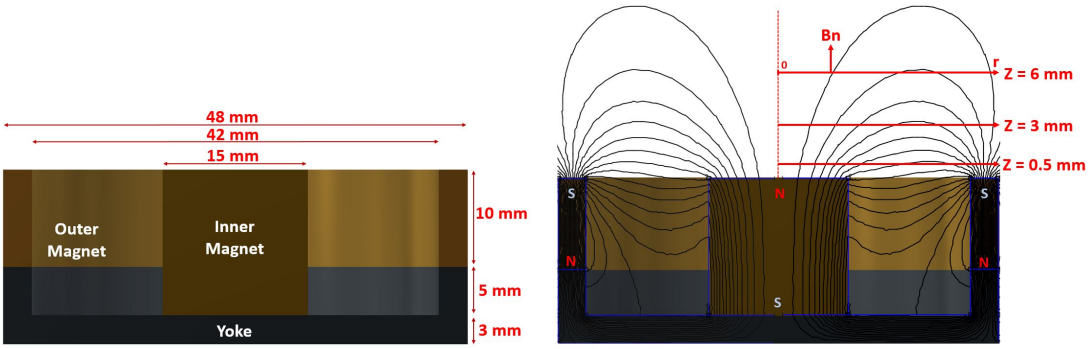

(a) (b)

Figure 4.3 – (a) Schematics of the triple planar magnetron system magnet assembly (b) Overlaid magnetic flux lines computed with FEMM, and radial axis r with indicative (not to scale) heights Z above the magnet assembly surface for analysis of figure 4.4.

Table 4.1 – Samarium/Cobalt permanent magnet data.

B_r [T]	H_c [kA.m^{-1}]	μ_r
0.90 ± 0.03	692 ± 24	1.0345

The normal component of the magnetic flux density B_n is measured radially with the same procedure described in section 3.1.2. It is compared with simulation results using the FEMM software and the BEM module of the PICMC code by extracting data from the three red lines drawn in figure 4.3(b) at 0.5, 3, and 6 mm above the magnet assembly, from its axis to its outer radius. This comparison is presented in figure 4.4 and shows a good agreement for the 3 and 6 mm height cases, while the 0.5 mm curves show a slight discrepancy. As the cathode surface is located at 5 mm above the magnet surface, the discrepancy of simulation and experiment for the 0.5 mm curve is not influencing the plasma volume. As such, the BEM magnetic field simulation provides an accurate input for the plasma simulation. Similarly to the methodology of chapter 3, comparison of simulated and experimental magnetic field has been done for one of its components, but the full 3D BEM mapping of the magnetic field is used in the plasma simulation.

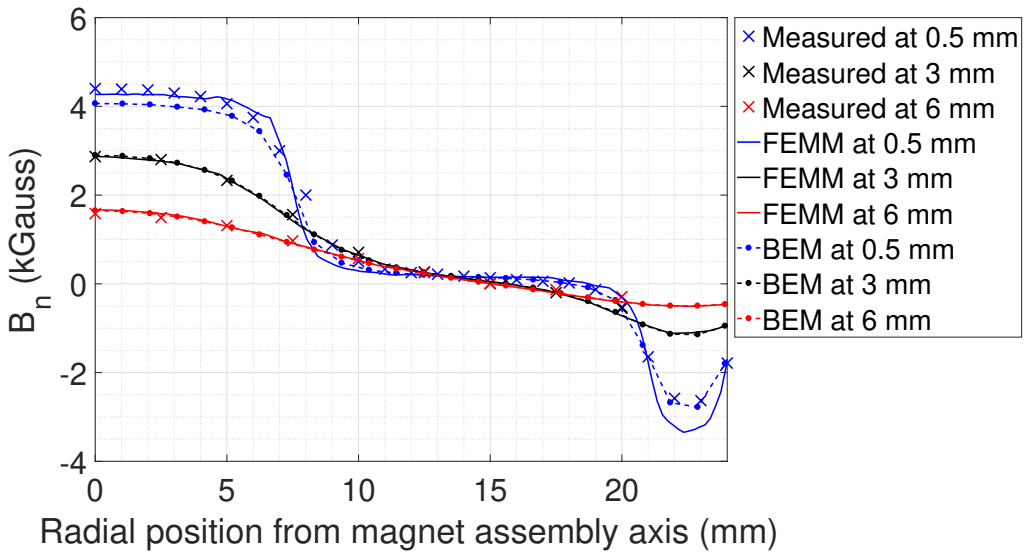

Figure 4.4 – Comparison of measured normal component of the magnetic flux density B_n[kGauss] with FEMM and BEM simulations for the triple planar magnetron system at three different heights above the magnet assembly (shown in figure 4.3(b)).

4.1.2.3 Simulation and experiment parameters

A simulation of the plasma discharge is performed at 10 Watts of power and used to study the scalability in power of cathode erosion profiles measured for experimental discharge powers of 10, 100 and 250 Watts. The absolute niobium sputtering profile is extracted from the PICMC plasma simulation and used as input for the DSMC transport simulation for thin film thickness profile analysis. The simulation domain is reduced to a height of 80 mm to shorten the simulation time, and the mesh size is refined in the plasma region above the cathode, as shown in table 4.2 in which the relevant simulation parameters are listed. Simulation and experiments are consistently performed with argon as the process gas at a pressure P_{Ar} = 8×10^{-3} mbar.
For the three experiments, the product *Power*×*coating time* is fixed at 7500 Watts × minutes.

Table 4.2 – Triple planar magnetron: physical and numerical plasma and neutral transport simulation parameters.

Domain size [mm^3]	152 x 152 x 102
Mesh size above the target [mm^3]	0.33 x 0.33 x 0.5
CPU used per run (cores)	144
Argon pressure [mbar]	$8x10^{-3}$
Scale factor Ar	$5x10^8$
PICMC plasma simulation	
Species	Ar, Ar^+, e^-, Nb
Discharge power [W]	10
Time step [s]	$5x10^{-12}$
Scale factor Ar^+, e^-	10^4
Initial density Ar^+, e^- [m^{-3}]	$5x10^{12}$
Simulation time	~ 2 months
Magnetic field	Computed by the BEM module
γ_{IISEE}	0.13
IISE energy distribution	Gaussian
IISE angular distribution	cosine
Electron capture probability on physical surfaces	100 %
Sputtering yield	According to Yamamura's analytical formula
DSMC transport simulation	
Species	Ar, Nb
Time step [s]	10^{-7}
Scale factor Nb	10^5
Simulation time	~ a week
Nb sputtering flux profile	Taken from the plasma simulation
Nb sputtering rate [sccm]	0.148, time-averaged between 10 and 15 μs
Sputtered Nb energy distribution	Thompson with E_b = 7.59 eV
Sputtered Nb angular distribution	undercosine with exponent 0.5

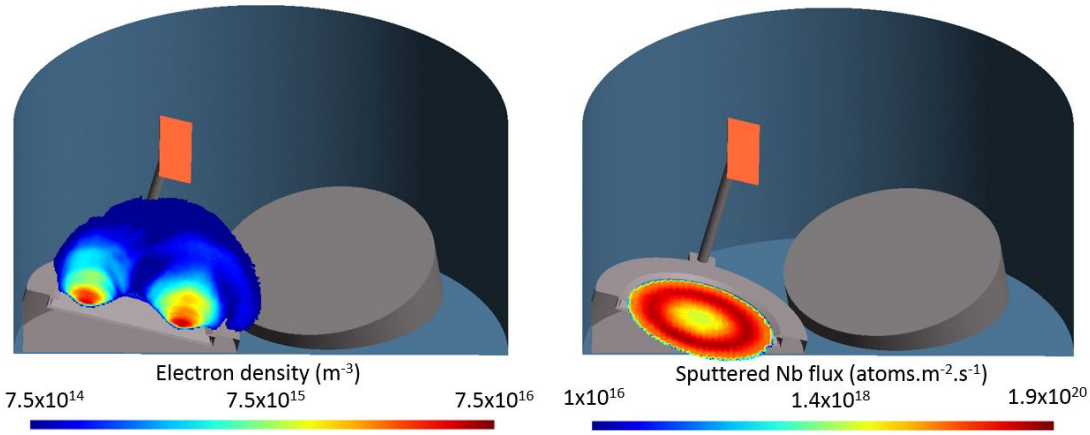

(a) (b)

Figure 4.5 – P = 10 W, $P_{Ar} = 8\times10^{-3}$ mbar, t = 15 μs: (a) Half view of the simulated electron density distribution [m^{-3}] (b) Sputtered niobium flux on the cathode disk surface [$atoms.m^{-2}.s^{-1}$].

The simulated electron density at t = 15 μs is displayed in figure 4.5(a) and the corresponding sputtered niobium flux is shown in figure 4.5(b).
Values of discharge voltage and current for the steady state[1] simulation at 10 Watt and the three experimental discharge powers are given in table 4.3. They show a discrepancy of ~ 60 V between simulation and experiment at 10 W. It can also be seen that while increasing the experimental discharge power, the voltage only slightly varies but the current largely increases, which is characteristic of the *abnormal glow* regime.

Table 4.3 – Discharge voltage and current for 10 W simulation and three experiments at different powers.

	Simulation[1]	Experiment[2]		
	10 W	10 W	100 W	250 W
Voltage [V]	310	250	330	380
Current [mA]	32	41	300	650
Coating time [minutes]		750	75	30

[1] I/V values averaged between 10 and 15 μs of stable simulation. Standard deviation is ± 6 V, ± 0.6 mA.
[2] Values given for conditioned cathode (oxide layer removed) after some minutes of coating, can vary within ± 10 V.

[1] Defined by stable discharge current and voltage.

4.1.3 Scalability of erosion and thin film thickness profiles

In this section, simulated and experimental erosion profiles on the cathode and thin film thickness profiles on the copper sample are compared as a function of discharge power.

4.1.3.1 Scalability of target erosion profile

New niobium targets machined from the same niobium sheet are used for each coating. A reference mark is engraved on their side such that their surface height deviation can be measured on 18 equally spaced diameters before and after each coating with respect to the same referential system described in figure 4.6. A Zeiss O-Inspect 863 measurement instrument is used[2] to measure the height using its optical confocal white light sensor [81]. The measurement reproducibility has been assessed to be within 1 μm, while its vertical error is 2.5 μm, yielding a total experimental uncertainty of ~ 4 μm. Each cathode is consistently positioned with its reference mark facing the closest chamber point, while the plane of reference before and after the coating is defined and measured with three points on the cathode disk edge. We assume that these points are not eroded during the coating process because they are protected by the anode guard ring (see figures 4.2b and 4.6).

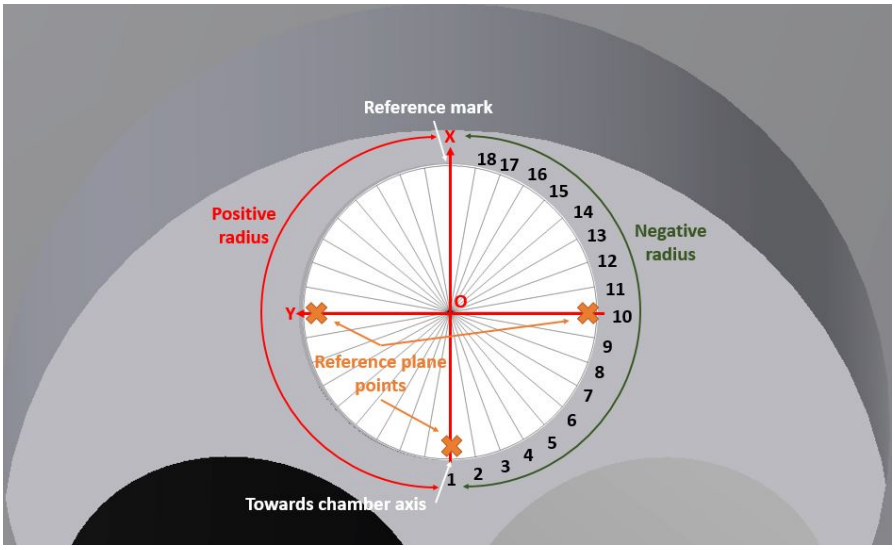

Figure 4.6 – Schematic view of the 18 diameters measured on the cathode surface within their reference system (same as figure 4.7) with indication of the three points defining the reference plane and of the adopted convention for radius sign.

3D plots of the cathode surface are presented in figure 4.7 for each coating power. They show the cathode surface height as measured before (reference) and after coating, and after coating with subtraction of the reference. It can be seen that this correction allows compensating for the initial cathode surface deformation.

[2] Courtesy of Didier Glaude, CERN-EN/MME/MM.

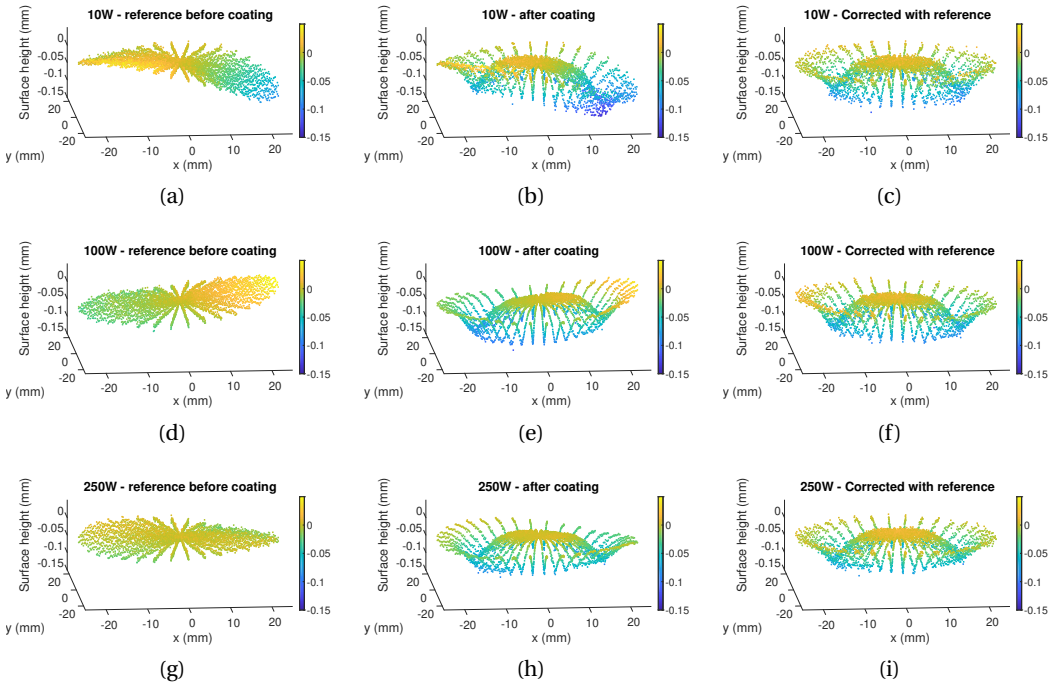

Figure 4.7 – 3D experimental cathode surface height (mm) - left column: as measured before coating, middle column : as measured after coating, right column : after coating with reference subtraction (a)(b)(c) 10 W - 750 min (d)(e)(f) 100 W - 75 min (g)(h)(i) 250 W - 30 min.

To better visualise and compare the experimental erosion profiles with the simulation, the XY coordinates of the 3D plots presented in figure 4.7 are converted to radial positions with sign convention as defined in figure 4.6. Then, the average and the standard deviation of the surface height over the eighteen measured diameters are computed for each radial position. In parallel, the simulated sputtered niobium flux obtained from the 10 W discharge and shown in figure 4.5(b) is averaged between t_{sim} = 10 μs and t_{sim} = 15 μs of steady state plasma simulation and converted to an erosion rate profile according to the first line of equation 4.1. The absolute erosion profile is obtained by multiplying the erosion rate with the experimental coating time for the same discharge power (10 W - 750 min). Then, the Cartesian coordinates are converted to radial positions following the same convention as for the experiment. At last, the simulation points are spatially down-sampled such that average and standard deviation are obtained over each radius bin of 47 points.
Comparison of experimental radial erosion profiles with simulation are given with their respective error bars in figure 4.8.

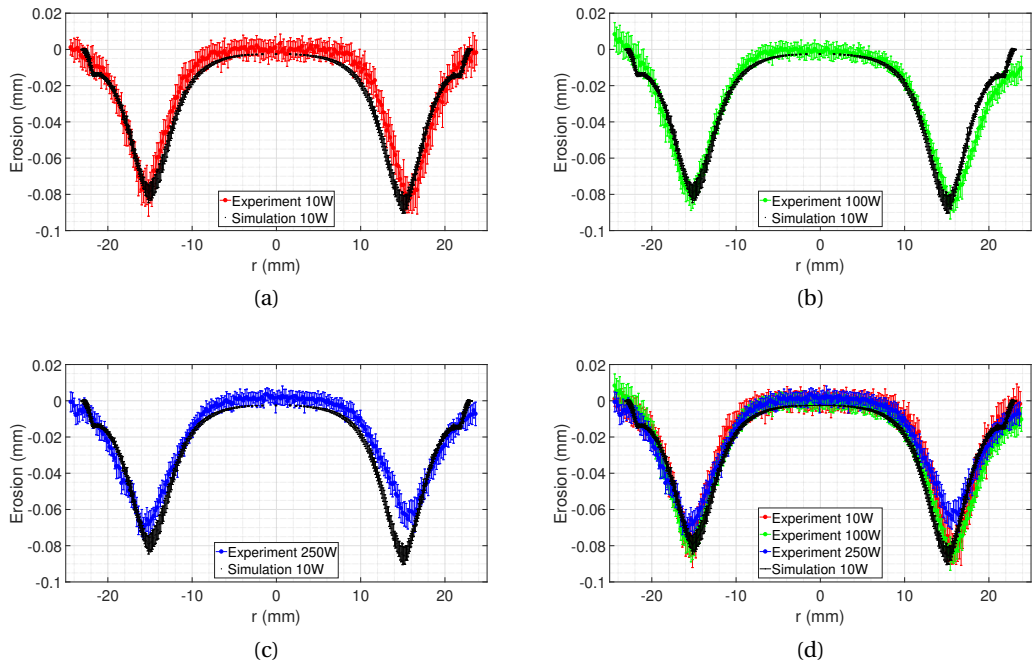

Figure 4.8 – Comparison of simulated erosion profile at 10 W with (a) experimental at 10 W (b) experimental at 100 W (c) experimental at 250 W. (d) Summary of experimental and simulated erosion profiles for different discharge powers, with *Power* × *Coating time* constant. Error bars are ± the standard deviation.

Figure 4.8(a) displays a good agreement between simulation and experiment at the same power of 10 W. Figure 4.8(d) shows that all experimental erosion profiles are almost identical to each other within their experimental uncertainty, even though a slight radial tilt of the 100 W curve and a small asymmetry of the erosion peaks at 250 W are visible respectively in figures 4.8(b) and 4.8(c). In the latter, while the left parts (negative radii) of the experimental and simulated erosion profiles are matching within their respective error bars, the right parts (positive radii) are in disagreement due to the experimental asymmetry. It is therefore difficult to assess if this mismatch is caused by the influence of the experimental higher power or rather by an experimental mishap. Furthermore, the simulated profile at 10 W agrees with the experimental ones at different powers, although the simulated slope inflexion at the cathode edges at ± 22 mm is not clearly visible on the latter ones because of the instrument accuracy. The simulated erosion profile presented in figure 4.8 does not take into account redeposition of niobium on the cathode. The transport simulation used in the next section for comparison of thickness profiles on copper samples shows that redeposition on the cathode can be neglected with respect to the erosion, as can be seen in figure 4.9. Indeed, redeposition thickness is at least one order of magnitude below the erosion level everywhere apart from the extreme edges of the cathode disk where both become negligible. Furthermore, the erosion of the new cathodes is at most of 80 μm at the end of each coating, as seen on figure 4.8d. Therefore, it has a negligible impact on the validity of plasma and neutral transport simulations of this

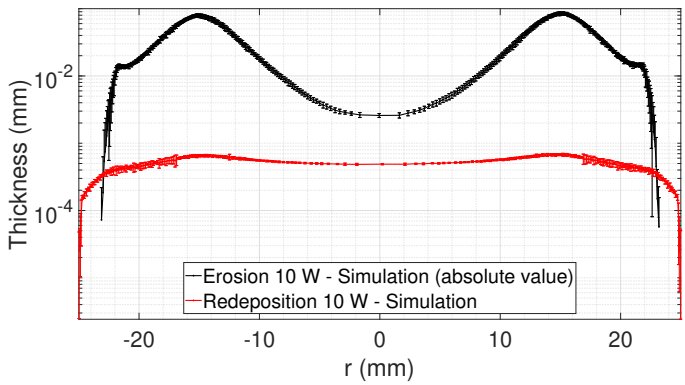

Figure 4.9 – Comparison of simulated erosion (plotted as positive values) and redeposition profiles on the cathode, semi-logarithmic scale.

study, as its magnitude is less than four times the mesh size used in the simulation (see table 4.2).
Therefore, it is confirmed that experimental erosion profiles obtained for realistic discharge powers can be fully described with a low power simulation by scaling the simulation coating time to match the experimental product *Power* × *Coating time*, and provided that the simulation is in the *abnormal* glow discharge regime (see assumptions of section 4.1.1).

4.1.3.2 Scalability of thin film thickness profiles

A DSMC transport simulation is performed with the parameters listed in table 4.2 by using the sputtering flux profile averaged between t_{sim} = 10 μs and t_{sim} = 15 μs of steady state plasma simulation. The niobium deposition flux on the copper sample is averaged between 30 and 40 ms of the DSMC transport simulation, once niobium deposition fluxes are stable on all surfaces, and converted to an absolute thickness profile using equation 1.20 and taking into account the coating time. Each experimental thickness profile is measured with the same XRF device as used in section 3.3. Comparison of the experimental profiles with the simulated one is presented in figure 4.10. It shows a reasonable consistency between all experimental thickness profiles (within ~ 10 % of each other) at the exception of an asymmetrical thickness decay at x larger than 25 mm in the 250 W case, which could be explained by a start of film delamination observed by visual inspection. Furthermore, the simulation profile is at most overestimating the experimental ones by 15 %. This is below the worst case scenario error of ~ 30% based on the assumptions made in section 4.1.1 which led to equation 4.4.

As such, the use of low power simulations to estimate experimental thickness profiles obtained with realistic discharge power coatings is validated.

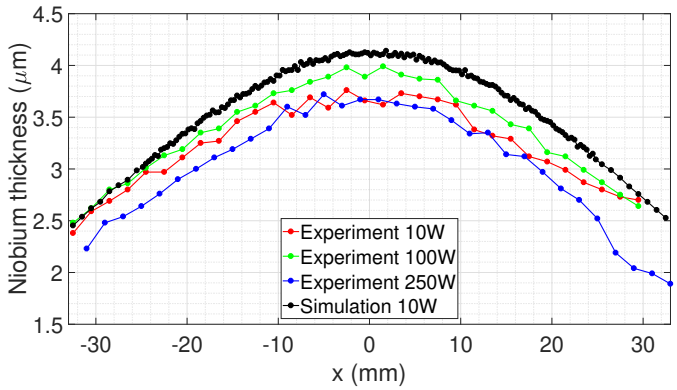

Figure 4.10 – Comparison of experimental and simulated thickness profiles $[\mu m]$ on the 80 mm long copper sample.

4.2 1.3 GHz elliptical cavity

The aim of this section is to apply the methodology and results presented so far to a real RF cavity. This allows investigating to which extent the magnetron plasma and transport simulations can be used to accurately model coating processes in real cavity configurations. The use of a complex geometry as in real cavity designs is also a good case study for thin film morphology simulations, since various niobium impinging angles induce different film growth orientations and compactness along the cavity geometry, which have an impact on RF properties (see section 1.1.5). As such, a single-cell elliptical copper cavity of the TESLA[3] geometry type [82] and operating at a frequency of 1.3 GHz has been chosen. Even though this copper cavity is only used at CERN for Research and Development purposes, its design has been studied or applied in its niobium bulk variant for accelerator projects such as the International Linear Collider (ILC) or the European X-Ray Free-Electron Laser (XFEL) [83].

4.2.1 Experimental configuration

4.2.1.1 Cavity geometry and experimental procedure

The 1.3 GHz copper cavity geometry is presented in figure 4.11(a) with its critical regions, while the dimensions of the cell are shown in figure 4.11(b). The *equator* and the *iris* correspond respectively to the regions of maximum magnetic field and electric field intensity during RF operation, and the cut-off tubes allow extinguishing the RF electromagnetic field before it reaches the cavity flanges and the normal conducting elements beyond. Therefore, the whole inner surface of the copper cavity has to be coated from flange to flange with a superconducting niobium thin film, although the region of interest for the present study is limited to the cavity cell. This restriction is justified because the coating of the cut-off tubes is less critical with respect to the cell part and does not add any valuable information in terms of simulation

[3] Teraelectronvolt Energy Superconducting Linear Accelerator

validation compared to the cavity central region.

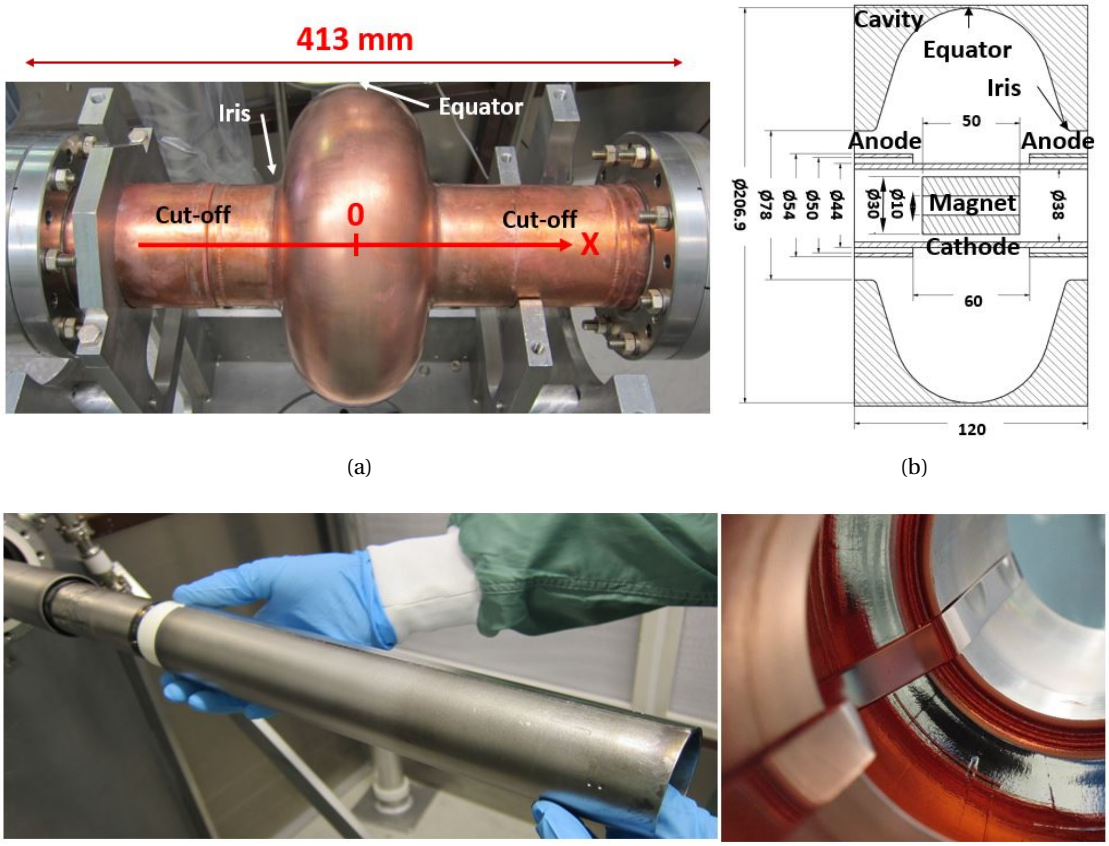

(a) (b)

(c) (d)

Figure 4.11 – (a) Picture of the 1.3 GHz elliptical cavity with its critical regions and axis of reference X. (b) Dimensions of the cavity cell [mm], with cathode and anodes. (c) Mounting of the niobium anode sleeves around the niobium cathode central tube. (d) Picture of the copper band inserted inside the cavity.

Before coating, the niobium cathode and anodes tubes are separated by ceramics, and assembled horizontally in a clean room environment as shown in figure 4.11(c). The cavity is finally mounted around them, together with a copper band shaped to follow its inner surface along its axis direction for *ex situ* thin film characterisation, as seen in figure 4.11(d). The cavity with anodes and cathode is vertically connected to a pumping system whose base pressure without bake-out is in the 10^{-7} mbar range, as represented in figure 4.12.
For one-to-one comparison with the simulation model, the cavity is coated at $P_{Argon} = 5.10^{-3}$ mbar at a discharge power of 10 W for 22 hours using an Advanced Energy MDX 500 DC power supply (the same as in chapters 2 and 3). A non-eroded cathode is used to match the simulation geometry, contrarily to what will be discussed in appendix C.

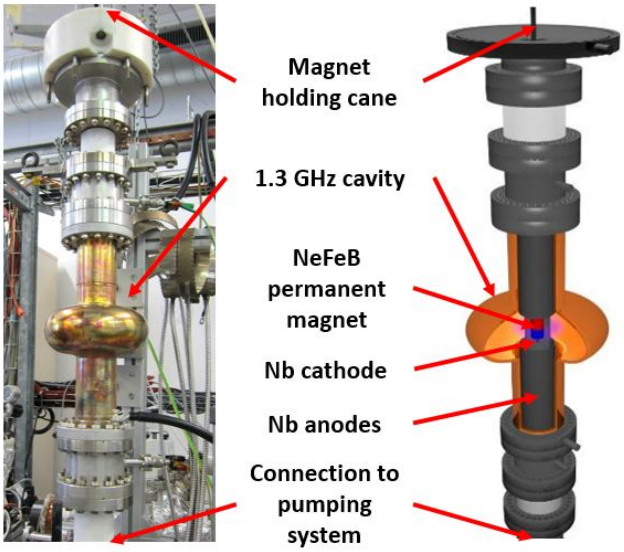

Figure 4.12 – 1.3 GHz cavity : picture of the coating system (left) and CAD view of the coating elements including cathode, anodes and permanent magnet for magnetron sputtering (right).

4.2.1.2 Permanent magnet characterization

To generate the magnetic field required for the balanced magnetron coating, a neodymium iron boron (NdFeB) permanent magnet is attached to a cane which can be vertically inserted from the top of the system inside the cathode tube, all along the cavity axis (see figure 4.12). This magnet is not in contact with the system vacuum and is air-cooled with a compressed air flow during plasma operation to avoid its demagnetisation. It has a hollow-cylinder shape of 30 mm outer diameter, 10 mm inner diameter and 50 mm length, and its magnetic characteristics are listed in table 4.4.

Table 4.4 – Neodymium iron boron permanent magnet data, manufacturer denomination N45SH in [74].

B_r [T]	H_c [kA.m^{-1}]	μ_r
1.32	1003	1.0473

Its axial magnetic flux component B_x is measured at the center plane of the magnet perpendicularly to the magnet axis X, and compared with FEMM and BEM simulations in the same configuration as in figure 3.3[4]. Results presented in figure 4.13 show a good match between the three profiles. Therefore, the BEM 3D mapping of the magnetic field is accurately modelling the experimental field, and is taken as input for the plasma simulation.

[4] B_x replaces here B_z from figure 3.3, as the axis magnet is here called X instead of Z.

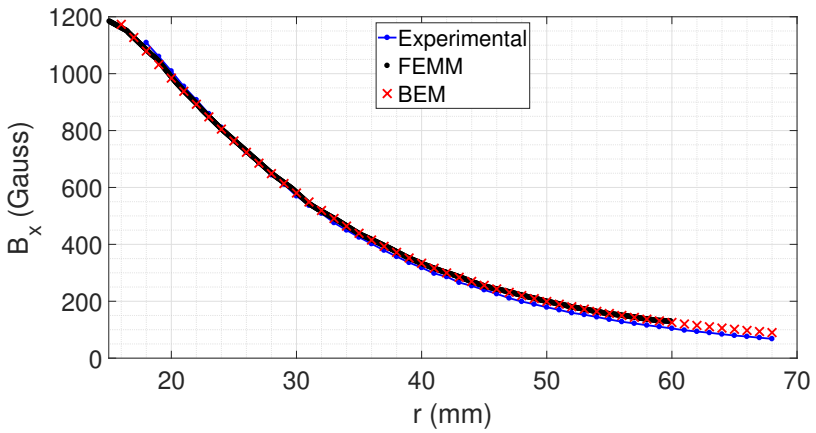

Figure 4.13 – Comparison of magnetic flux density axial component B_x (Gauss) radial profiles for BEM and FEMM simulation with experiment. The radius corresponds to the distance from the magnet axis.

4.2.2 Plasma simulation

A plasma simulation is performed to model the balanced magnetron discharge used in the coating process of the central cell of figure 4.11(b) with a discharge power P_{dis} = 10 W. Numerical parameters are listed in table 4.5, and non-listed parameters are the same as in the PICMC plasma simulation part of table 4.2. Moreover, the anodes and the cavity are grounded, while the cathode voltage is regulated during the simulation run to meet the power setpoint.

Table 4.5 – Physical and numerical simulation parameters for the 1.3 GHz elliptical cavity plasma modelling.

Domain size in XYZ [mm^3]	120 x 210 x 210
Mesh size [mm^3]	1 x 1 x 1
CPU used per run (cores)	150
Scale factor Ar	7x10^9
Ar pressure [mbar]	5x10^{-3}
Discharge power [W]	10
Simulation time	1 month

In the plasma simulation, stable I/V discharge values are reached after 20 μs, and the simulation is run for 42 μs in total such that outputs can be smoothed. The I/V values are time-averaged between t_{sim} = 27 μs and t_{sim} = 42 μs, and are in agreement with the experimental ones, as shown in table 4.6.

Table 4.6 – Discharge voltage and current for 1.3 GHz elliptical cavity simulation and experiment. P_{dis} = 10 W, P_{Ar} = 5x10^{-3} mbar.

	Simulation[1]	Experiment[2]
Voltage [V]	280 ± 8	289 ± 5
Current [mA]	36 ± 1	35 ± 1

[1] I/V values averaged between t_{sim} = 27 μs and t_{sim} = 42 μs of stable simulation, with ± their standard deviation.
[2] Values given for conditioned cathode (oxide layer removed) after some minutes of coating.

Two views of the simulated electron density are displayed in figure 4.14(a) along with a side photograph of the experimental discharge in the same configuration but in a cavity *mockup* featuring a lateral viewport in figure 4.14(b).

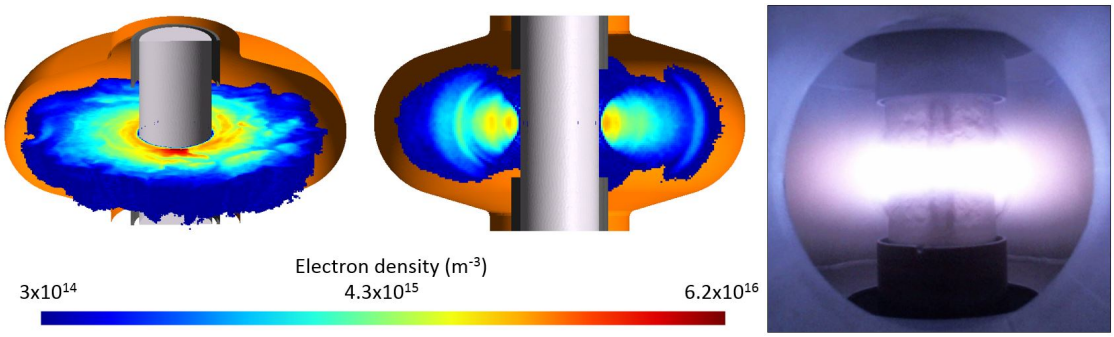

(a) (b)

Figure 4.14 – (a) Half views of the simulated electron density at t_{sim} = 42 μs (b) Photograph of the plasma discharge in a cavity *mockup* featuring a lateral viewport.

4.2.3 Sputtered atoms transport and thin film thickness profile

The niobium sputtering profile is averaged between t_{sim} = 27 μs and t_{sim} = 42 μs of the steady state plasma simulation such that inhomogeneities due to plasma instabilities are smoothed. This time-averaged profile is used as input for the DSMC transport simulation. It can be seen in 3D in figure 4.15(a), while figure 4.15(b) shows the 2D sputtering profile averaged over all azimuthal positions for each position x along the cathode axis. The peak value of ~ 3.2x10^{19} atoms.m^{-2}.s^{-1} corresponds to a maximum erosion depth of ~ 46 μm (see first line of equation 4.1) after 22 hours of coating. This erosion is negligible compared to the mesh resolution, and therefore has no influence on the validity of plasma and transport simulations when assuming a perfectly non-eroded cylindrical cathode. The influence of a larger cathode erosion on the plasma simulation will be discussed in appendix C.

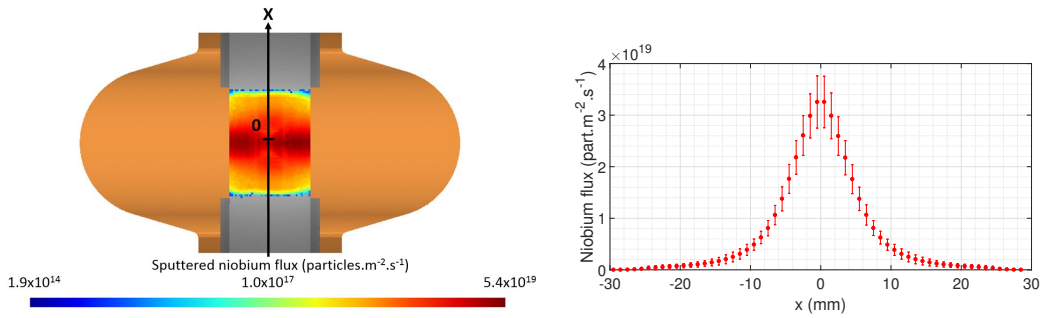

(a) (b)

Figure 4.15 – (a) 3D niobium sputtering profile averaged between t_{sim} = 27 μs and t_{sim} = 42 μs (b) Corresponding 2D profile averaged over all azimuthal positions and projected on the cathode axis X [mm].

Table 4.7 – Physical and numerical simulation parameters for the 1.3 GHz elliptical cavity transport modelling.

Species	Ar, Nb
Time step [s]	10^{-7}
Scale factor Nb	10^4
Simulation time	~ a week
Nb sputtering flux profile	Taken from the plasma simulation
Nb sputtering rate [sccm]	0.118, time-averaged between t_{sim} = 27 and t_{sim} = 42 μs
Sputtered Nb energy distribution	Thompson with E_b = 7.59 eV
Sputtered Nb angular distribution	Heart-shaped or Cosine with exponent 0.3, 0.5 and 1

The numerical parameters used for the DSMC transport simulation are listed in table 4.7. The cutoff ends are filled by virtual membranes absorbing niobium atoms and specularly reflecting argon atoms, such that the process gas pressure could remain constant inside the simulation volume.

We first study the thin film thickness profile of the simulation with a power cosine niobium angular distribution with exponent 0.5, which was already used in chapter 3 and section 4.1.2.3 of the present chapter. The stable deposited niobium flux on the cavity surface is time-averaged between t_{sim} = 100 and 120 ms for data smoothing. Then, the deposition profile is averaged for each axial position over the azimuthal direction, thus providing standard deviations. Finally, the deposition flux profile is converted to thickness according to the procedure described in section 4.1.3.2. In parallel, the experimental thickness profile is measured *ex-situ* by X-ray fluorescence on the copper band sample. Comparison of experimental and simulated thickness profiles projected along the cavity axis X is presented in figure 4.16.

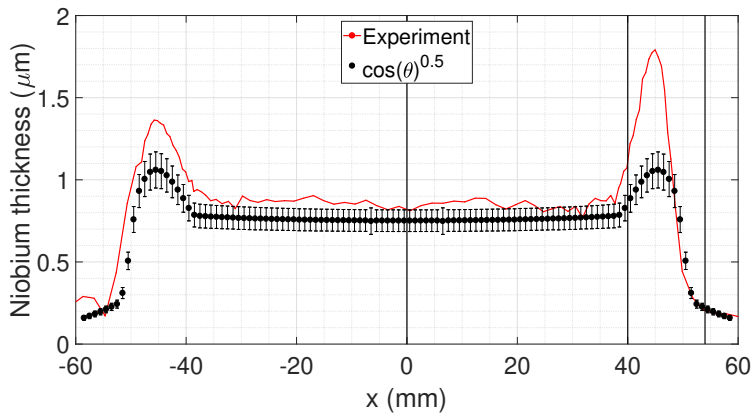

Figure 4.16 – Niobium experimental and simulated thin film thickness profiles with $\cos^{0.5}$ initial angular distribution of sputtered niobium atoms. Vertical black lines indicate the positions of samples for morphology analysis of section 4.2.4: $x_{Equator}$ = 0 mm, x_{Flat} = 40 mm, x_{Iris} = 54 mm.

Figure 4.16 shows that the experimental profile is asymmetrical, which could be explained by a slight misalignment of the permanent magnet with respect to the center of the cathode. This leads to a plasma shift along the X-axis, in turn causing a shift of thickness profile. Then, the simulation qualitatively reproduces the two experimental peaks, and is quantitatively close to the experimental values with an underestimation of ~ 8 % in the central flat region, and of ~ 25 % at the left peak. This could partially be explained if the copper band sample is not in full contact with the cavity surface during the coating, as it is only fixed at its two extremities. It would then be locally closer to the cathode than in the simulation, which could result in slightly larger experimental thin film thicknesses.

As was detailed in section 1.1.2, a power cosine distribution is generally assumed for the initial sputtered atoms angular distribution, but its exponent can vary depending on the voltage, cristallinity and surface state of the target. *Heart-shaped* angular distributions are also reported in the literature (see section 1.1.2). The influence of this parameter is investigated by performing three other DSMC simulations with the same input parameters except the sputtered niobium initial angular distribution, which is taken as a power cosine distribution with exponent 0.3 and 1, and a heart-shaped distribution $f(\theta) = cos(\theta) * (1 - 0.5 * cos^2(\theta))$. These three distributions are plotted in figure 4.17 along with the $\cos^{0.5}$ one.

For each DSMC simulation, thickness profiles projected along the cavity axis X are obtained similarly to the $\cos^{0.5}$ profile of figure 4.16. Figure 4.18 presents the comparison of the experimental thickness profile with the simulated ones for the different angular distributions of sputtered niobium atoms.

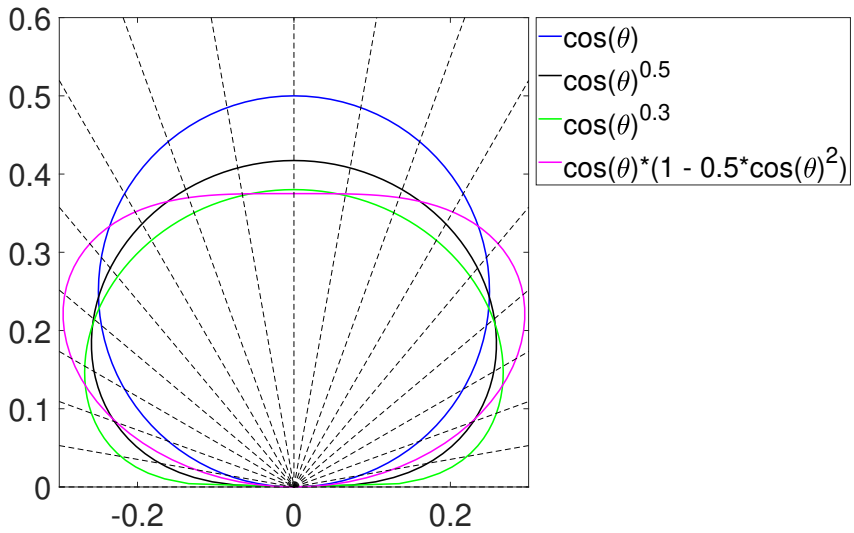

Figure 4.17 – Comparison of angular distributions of sputtered atoms: cosine with different exponents and heart-shaped. Dashed lines are equally spaced of 10 °.

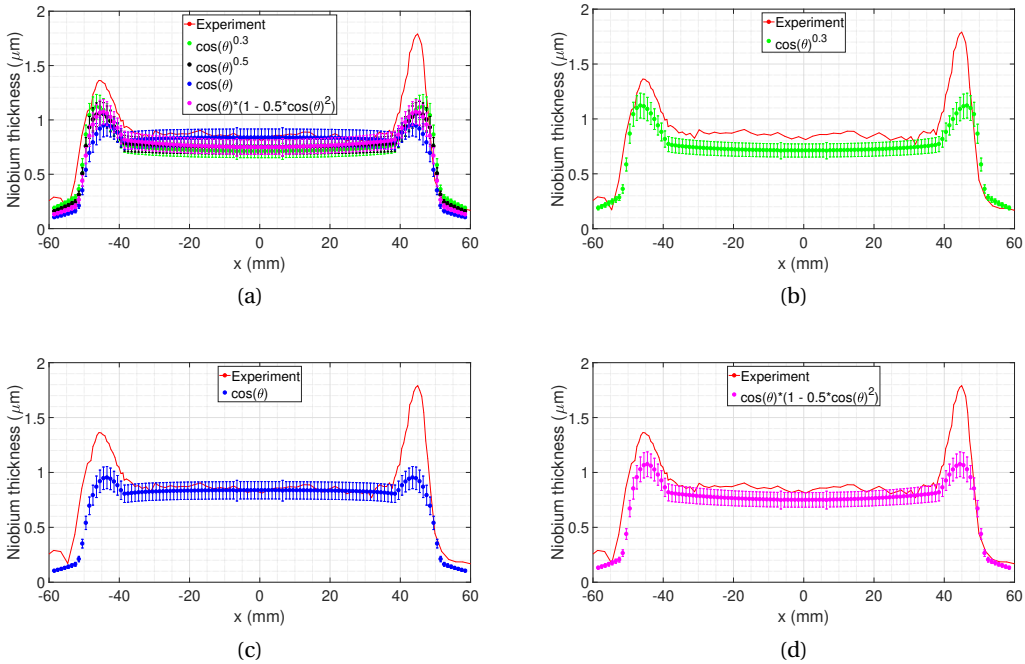

Figure 4.18 – Niobium experimental and simulated thin film thickness profiles (a) All data - Comparison of experiment with (b) $cos^{0.3}$ (c) cos and (d) heart-shaped angular distributions.

Figure 4.18(a) shows that a change of angular distribution only slightly influences the resulting niobium film thickness profiles, while a higher exponent in the cosine distribution increases the thickness on the sides. It is difficult to validate one distribution over the others, as the

cosine one is closer to the experimental profile at the center of the cavity, but is worse at its extremities. On the contrary, the $cos^{0.5}$ and the heart-shaped distributions present profiles very close to each other, with axial positions of the two peaks quite close to the experimental ones. Therefore, we choose to keep the $cos^{0.5}$ distribution which was already used in chapter 3 and section 4.1.2.3 of the present chapter as a good approximation for DSMC simulations.

4.2.4 Thin film morphology

In this section, we first present energy and angular distributions of deposited atoms extracted from the DSMC simulation at three distinct positions along the cavity surface. These three positions are chosen because of their different thicknesses (see figure 4.16) and tilts with respect to the cathode. Then, results of thin film growth simulations using these energy and angular distributions as inputs are compared with coupled Focused Ion Beam - Scanning Electron Microscopy (FIB/SEM) imaging of the thin film layer grown on the copper band sample at the same positions.

4.2.4.1 Extraction of energy and angular distributions of deposited atoms from DSMC simulation

In the DSMC simulation with the $cos^{0.5}$ initial angular distribution of sputtered atoms, three virtual surfaces (also dubbed *membranes*) are positioned at different positions just above the cavity surface at $x_{Equator}$ = 0 mm, x_{Flat} = 40 mm and x_{Iris} = 54 mm, as seen in figure 4.19.

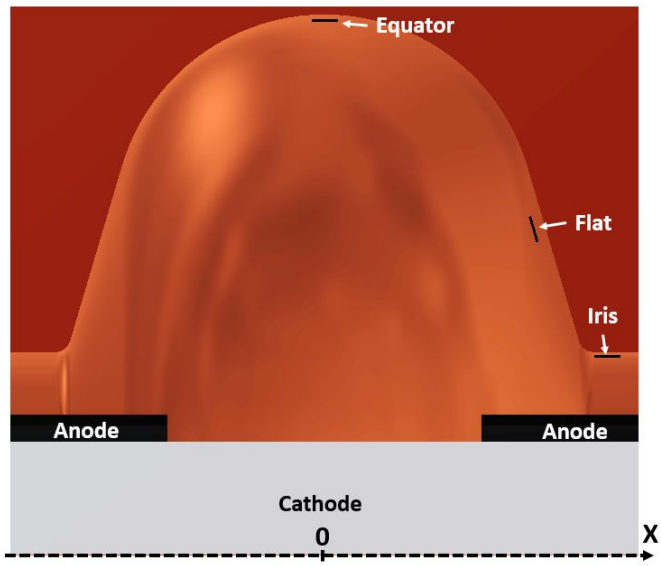

Figure 4.19 – Position of virtual surfaces for recording of sputtered atoms energy and angular distributions. Axial positions from the cavity center are : $x_{Equator}$ = 0 mm, x_{Flat} = 40 mm, x_{Iris} = 54 mm.

These membranes consist in square surfaces of 5x5 mm^2 which do not influence the simulation, but are used to record the number of sputtered niobium atoms passing through, along with their angular and energy distributions. The energy distributions on the three membranes are shown in figure 4.20.

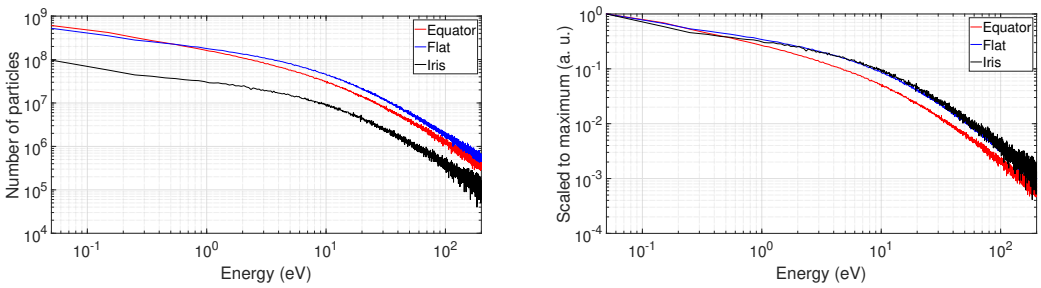

(a) (b)

Figure 4.20 – Energy distribution of sputtered atoms on the three membranes at t_{sim} = 120 ms, in logarithmic scale. (a) Real number of particles (b) Number of particles normalized to the respective maximum of each curve.

Figure 4.20(a) shows that the number of niobium atoms recorded at the iris is seven to eight times lower than on the other two regions, which is consistent with the thin film thickness trend of figure 4.16. These energy distributions can be normalized by their respective maximum as presented in figure 4.20(b). With this normalization, the distributions of the flat and iris regions are very similar. This is resulting from the mean distances from these regions to the cathode surface central point (x = 0 mm) being very close (respectively 57 and 56 mm) and the sputtered atoms passing through them having experienced a comparable number of collisions with the process gas atoms. In comparison, the equator is located at 80 mm from the cathode surface central point and sputtered atoms passing through it have experienced more collisions than for the other two regions, thus explaining its energy distribution shift towards slightly lower energies.

The angular distributions polar plots for each membrane are presented in figure 4.21, with θ being the impinging angle with respect to each membrane normal vector, and ϕ being the azimuthal angle in the membrane local system of reference. The ϕ = 0-180 ° axis is defined as the projection on each sample of the -XX axis displayed in figure 4.19. The displayed intensity corresponds to the number of particles per θ and ϕ angular bin normalized by their respective solid angle $d\omega(\theta,\phi) = sin(\theta)d\theta d\phi$. This normalization is done by dividing the number of particles of each bin by $sin(\theta)$.

The distributions of θ and ϕ in the three cases can be principally explained by the geometrical position of each sample. Indeed, $\theta \in [0° - 10°]$ in the equator membrane (figure 4.21(a)) because it is normally facing the cathode, while $\theta \in [20° - 40°]$ and $\theta \in [60° - 80°]$ respectively for the flat and iris membranes (figures 4.21(b) and 4.21(c)) because of their tilts with respect to

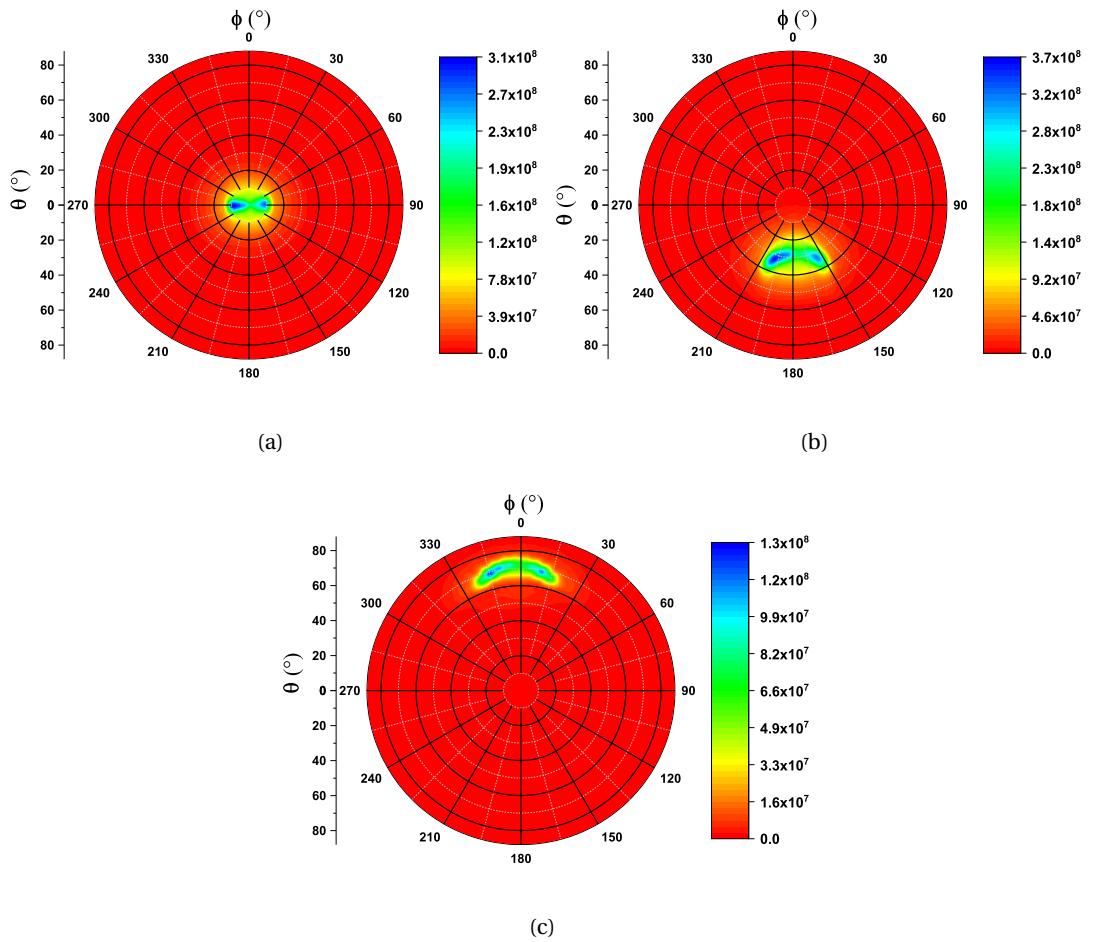

Figure 4.21 – Polar plots of sputtered atoms angular distributions: (a) Equator (b) Flat (c) Iris. The intensity is the number of particles. θ is the impinging angle with respect to the surface normal, and ϕ is the azimuthal angle. The ϕ = 0-180 ° axis is defined as the projection on each sample of the -XX axis displayed in figure 4.19.

the cathode axis. $\phi \sim 180°$ for the flat membrane because atoms coming from the cathode pass through it from the +X-X projected direction, while $\phi \sim 0°$ for the iris because atoms coming from the cathode pass through it from the -X+X projected direction. Without considering the influence of collision events discussed above, the spread in ϕ for all membranes is due to atoms being emitted from the whole cathode diameter (44 mm) and is larger than the spread in θ attributed to the sputtering profile full width at half maximum of ~ 15 mm (see figure 4.15(b)).

4.2.4.2 NASCAM film growth simulation

The energy and angular distributions of figures 4.20(a) and 4.21 on the three membranes are used as inputs for thin film growth simulations using the kinetic Monte Carlo (kMC)

Nanoscale Modeling (NASCAM) software [5] running on a regular desktop computer. For the three simulation cases, a copper cubic lattice of 1000 atoms length, 5 atoms depth and 10 atoms height is used as the substrate. The number of deposited atoms $N_{position}$ for each NASCAM simulation is chosen as close as possible (ten times lower) to the the total number of atoms recorded on each membrane in the DSMC simulation during a time span equivalent to the experimental coating time without overloading the computer memory: $N_{Equator}$ = 2.6x10^6, N_{Flat} = 3.4x10^6, N_{Iris} = 6.5x10^5. The cavity temperature during coating (T = 423 K) is negligible compared with the melting temperature of niobium (T_m = 2750 K), corresponding to $T/T_m \sim 0.15$. This leads to little adatom surface mobility according to [41, 42, 84]. Thus, diffusion is neglected in the simulations, resulting in shorter computational times. Moreover, crystal growth in the film is not included in the version 4.6.2 of NASCAM used for this study. Finally, the influence of the bombardment of energetic neutral argon atoms reflected from the cathode on the film growth characteristics is not taken into account, and will be investigated in the future.
Each simulation output consists of a 3D matrix containing the positions of the deposited atoms on top of the copper substrate, and is post-treated in Matlab to give visual results comparable to SEM images, with atom positions converted to dimensions in nm based on the covalent radius of niobium (164 pm).

4.2.4.3 Comparison with FIB/SEM analysis

For each of the three membrane positions, a part of the coated copper band is cut and analysed with FIB/SEM[5]. First, a protective platinum layer is deposited on the niobium thin film. Then, each sample is milled with the gallium ion source of the FIB along the X axis of the cavity (figure 4.19). At last, SEM side pictures are taken perpendicularly to the FIB milling direction and compared with the film growth simulations, as seen in figure 4.22.

The number of niobium particles used as input in each film growth simulation is ten times smaller than those impinging on each membrane in the DSMC simulation, due to computer memory limitations. This results in different absolute scales for SEM images and simulations. However, scaling simulation dimensions to the SEM ones results in a qualitative match of relative thicknesses for each sample location. Moreover, although cristallinity is not accessible in the simulations, the morphology of each simulated thin film matches the experimental one in terms of both angular growth and qualitative layer density. Indeed, the equator sample is characterized by a dense film with a normal angle growth direction, while the flat sample shows an oblique growth orientation in both SEM image and simulation ($\beta \sim$ 15-20 °, where β is the angle of growth defined with respect to the substrate normal). At last, the iris sample is largely porous with a growth orientation of $\beta \sim$ 45-50 ° in both simulation and experiment.

[5]Courtesy of Elisa Garcia-Tabares Valdivieso, Ana Teresa Perez Fontenla and Alexander Lunt, CERN-EN/MME/MM

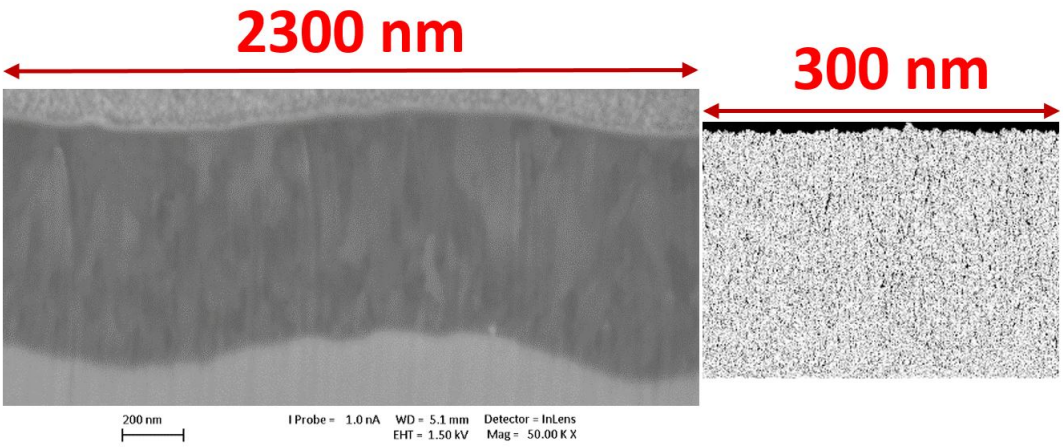

(a)

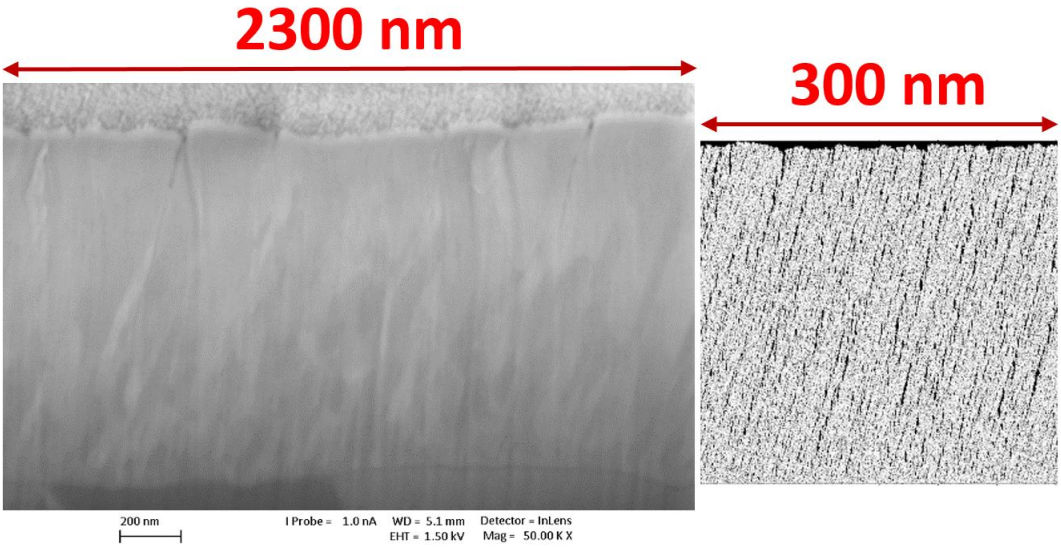

(b)

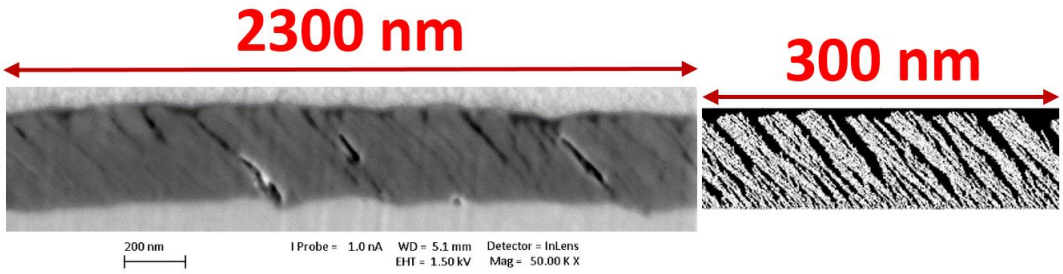

(c)

Figure 4.22 – Comparison of SEM images (left) with NASCAM simulations (right): (a) Equator (b) Flat (c) Iris.

A *tangent rule* is empirically derived in [85] and used in [86] to describe oblique film grown by evaporation at low pressures in the 10^{-8} mbar range corresponding to a collisionless regime. This rule states that:

$$tan\theta = 2 \times tan\beta. \tag{4.5}$$

where θ and β are respectively the incident angle of the sputtered particles impinging on the substrate and the film growth angle with respect to the substrate normal. In table 4.8, we compute β on each location according to equation 4.5 by taking rough values of θ from figure 4.21, and compare them to angles β taken from the SEM images and corresponding simulations.

Table 4.8 – Comparison of film growth angle β depending on impinging angle θ, as computed by the tangent rule and as taken from SEM images and simulations.

Sample	θ [°] - figure 4.21	β [°] - tangent rule	β [°] - simulations/SEM images
Equator	0-10	0-5	~ 0
Flat	20-40	10-23	15-20
Iris	60-80	41-71	45-50

The film growth angles from simulations and SEM images are within the intervals predicted by the tangent rule, which assumes no collisions between evaporated atoms and chamber residual gas atoms. This match is due to the low process pressure, which means that niobium atoms experience very few collisions before being deposited. It is also stated in [87] that the tangent rule is valid for deposition angles θ below 60°, which is mostly true in our case. These two points further explain the good match of film growth angles observed in the SEM images with the tangent rule estimates.

At last, we compare in table 4.9 and figure 4.23 thin film thicknesses evaluated by XRF, FIB/SEM (from figure 4.22) and DSMC simulation (undercosine with exponent 0.5) at the three sample locations. XRF and simulation thicknesses are taken from figure 4.16 at the position of the three vertical black lines corresponding to the sample positions.

Table 4.9 – Comparison of thicknesses measured by XRF, FIB/SEM with simulations on the three sample locations. XRF and simulation thickness values are taken at the position of the three vertical black lines of figure 4.16 corresponding to the sample positions.

Sample	FIB/SEM [nm]	XRF [nm]	Simulation [nm]
Equator	808	812	750
Flat	1172	1072	860
Iris	304	208	220

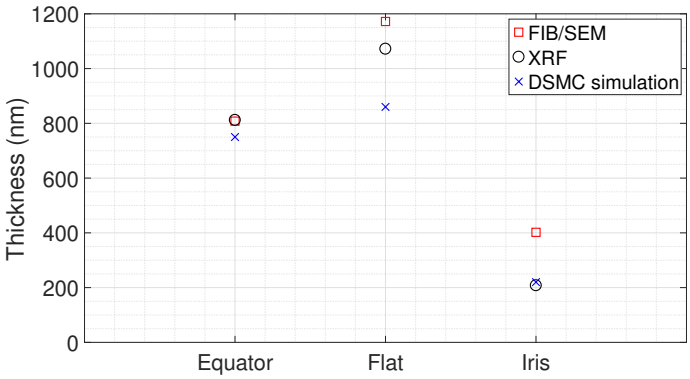

Figure 4.23 – Comparison of thicknesses measured by XRF, FIB/SEM with simulations on the three sample locations. Data taken from table 4.9.

At the equator position, XRF and FIB/SEM measurements agree with each other, while the simulation underestimates the FIB/SEM measurement by ~ 60 nm (equivalent to ~ 7 %). This agreement is attributed to the dense film morphology at this location. The XRF measurement underestimates the thin film thickness with respect to FIB/SEM measurements on the *flat* sample by ~ 100 nm (equivalent to ~ 9 %), which is within the error of the XRF instrument estimated in section 1.1.6.3. The thickness mismatch with simulations at this location was already visible in figure 4.16. At last, simulation and XRF measurement agree well with each other at the iris, and underestimate by ~ 30 % the thickness measured by FIB/SEM, which is explained by the porosity of the film at this position. Indeed, FIB/SEM thickness estimates are directly measured on the SEM cross-section images of the film, while DSMC simulated thicknesses assume that the thin film has the density of the bulk[6] and XRF measurements rely on the number of excited atoms in the thin film layer. Therefore, simulations and XRF measurements do not take film porosity into account contrarily to FIB/SEM analysis, and always underestimate thicknesses of porous films.
The qualitative agreement between film growth simulations and FIB/SEM imaging, as shown in this section, points towards a promising use of thin film morphology simulation tools as

[6]This assumption appears in the conversion from deposition flux to deposition rate of equation 1.20, which uses the niobium bulk density in the conversion factor.

another step in the methodology for modelling thin film coating processes.

4.3 Conclusion

In this chapter, the scalability of low power simulation results to realistic coating powers was first explored with a planar magnetron system. It showed that cathode erosion and thin film thickness profiles are comparable at different experimental discharge powers while keeping the product *discharge power* × *coating time* constant, and that low power simulation results are matching the experimental ones within 15 % of their absolute values.

Then, the results and methodology presented in chapters 2 and 3 were applied to an elliptical 1.3 GHz RF cavity cell. Simulated and experimental results are in agreement in terms of plasma parameters and deposited niobium thickness profiles, while changing the initial angular distribution of sputtered niobium atoms in the simulation shows little influence on the simulated thickness profile.

Thin film growth was successfully modelled with the NASCAM simulation software, and matched experimental FIB/SEM cross-sections of the film at three different locations of the cavity in terms of film growth orientation and more qualitatively in terms of film porosity.

Summary and future plans

Summary

In this thesis, we investigated the use of a Particle-in-Cell Monte Carlo/ Direct Simulation Monte Carlo (PICMC/DSMC) code to model niobium thin film deposition by DC sputtering in argon discharges for different geometries and plasma configurations. An *ab initio* methodology has been developed to include plasma modelling at low discharge power, sputtered atoms transport and thin film growth, and has been benchmarked against experiments for each of these steps. This methodology was motivated by the complexity and variety of sputtering sources and configurations used at CERN, which often involve expensive and time-consuming experimental R&D phases.

We identified critical physical parameters such as ion-induced secondary electron emission (IISEE) yield and energy distribution for accurate plasma modelling in chapter 2, or angular distribution of sputtered atoms for neutral transport in chapter 4. In chapters 3 and 4, experimental thin film thickness profiles on different substrate geometries have been reproduced by the simulations both qualitatively and quantitatively. In chapter 4, some numerical limitations have been overcome by showing that low power discharge simulation results can be scaled to realistic powers used in coating applications in terms of cathode erosion and thin film thickness profiles.

The benchmarking study, combined with applications to typical coating systems used at CERN and including an elliptical RF cavity cell, have confirmed the usefulness of the simulation approach in gaining further understanding of existing coating processes, thus being promising for guiding the design phase of future coating systems.

Future plans

The present study focused on niobium as the deposited element and argon as the plasma process gas. Both the methodology and the results of this work will be extended to the modelling of niobium coatings for future RF cavity projects, such as the Nb/Cu crab cavity shown in figure 1.1(c). Modelling the coating process of this cavity will be challenging due to its peculiar geometry and large size in particular, resulting in a potential need for multiple sputtering sources and deposition steps.

For some applications, krypton is preferred to argon when neutral process gas atoms incorporation in the film is critical [88, 89]. Therefore, the methodology presented in this work will be extended to krypton with a pre-required validation of physical input parameters (e.g. IISEE parameters, volume collision reactions, ...) such that fast neutral atoms incorporation can be modelled accurately and benchmarked against measurements done by laser ablation of the film. The inclusion of energetic neutrals in the simulation reaction model will also have an impact on sputtering rates at the cathode surface and on the deposited film growth.

A further field of investigation involves modelling of amorphous carbon coatings used at CERN for reducing the electron-induced secondary electron emission yield of vacuum components surfaces and thus mitigating the electron cloud effect [2]. In this case, the change of target material from niobium to graphite will also imply a validation of IISEE parameters. This will be experimentally determined with measurements of secondary electron current and energy distribution under ion gun bombardment. The presence of small hydrogen quantities in the plasma discharge is known to deteriorate amorphous carbon film properties in terms of secondary electron emission yield reduction. Modelling of this process will require benchmarking hydrogen-carbon chemical reactions in the plasma discharge and at the surfaces against experimental measurements done by ions and neutral atoms mass and energy resolved spectrometry.

The last topic of research will involve simulations of multi-compound thin film deposition such as titanium-zirconium-vanadium (TiZrV) for Non-Evaporable Getter coatings [1] or Nb_3Sn and V_3Si as potential replacements for pure niobium films due to their higher critical temperatures T_c. This will add new layers of complexity in the modelling process, including IISEE parameters of the alloy target and different sputtering yields for each element, different collision reaction cross-sections with the process gas atoms. Such a modelling will result in quantitative predictions of thin film stoichiometry.

All of these future extensions of the present study could involve thin film growth simulations, and will require a continued exchange of information with the developers of the PICMC/DSMC simulation code [4], for instance regarding the implementation of proper boundary conditions for magnetron plasma simulation of quarter models with azimuthal symmetry. Other interesting upgrades of the simulation code could include the ability to record angular and energy distributions of charged particles and neutrals on non-planar virtual surfaces. This would provide valuable insight in the local phenomena occurring respectively in the cathode sheath and at the surface of complex-shaped substrates, and in the latter case could be used for film growth simulations.

A Research and Development plan has already been defined at CERN to tackle these objectives and support thin film deposition activities by numerical simulations for future coating projects of CERN accelerator components.

A Matlab scripts for sputtering yield computation

The Matlab script used to generate the sputtering yield expression for the PICMC simulations according to Yamamura's development given in [6] is the following:

```
%Computation of sputtering yields under normal incidence ion bombardment
%Based on ENERGY DEPENDENCE OF ION-INDUCED SPUTTERING YIELDS
%FROM MONATOMIC SOLIDS AT NORMAL INCIDENCE, Y. Yamamura and H. Tawara
%Atomic Data and Nuclear Data Tables 62, 149-253 (1996)

%Comment/Uncomment/add parameters Q to Z2 depending on materials of
%interest
%1 is the incident ion, 2 is the target material

clear all, close all

%Sputtering Yield of Ar+ -> Nb PAGE 208
%Ar + -> Nb
Q = 0.93;
U_s = 7.57;
s = 2.8;
w = 2.65;
M1 = 40; %Standard atomic weight of 1, argon
M2 = 93; %Standard atomic weight of 2, niobium
Z1 = 18; %Atomic number of 1, argon
Z2 = 41; %Atomic number of 2, niobium

%Sputtering Yield of Kr+ -> Nb PAGE 209
% % Kr + -> Nb
% Q = 0.93;
% U_s = 7.57;
% s = 2.8;
% w = 2.65;
% M1 = 83.8;
% M2 = 93;
% Z1 = 36;
% Z2 = 41;

[A, Gamma, k_e, B, E_th] = SputteringYieldForSimulation(Q, U_s, w, M1, M2, Z1, Z2
    );

YamamuraYieldExplicit = [];
E = ceil(E_th):1:1000000;

```

```
for i = 1:1:length(E)
    YamamuraYieldExplicit(i) = A /(1 + Gamma* k_e * (B*E(i))^(0.3)) *...
    (3.441*sqrt(B*E(i)) * log(B*E(i) + 2.718))/...
    (1 + 6.355 * sqrt(B*E(i)) + B*E(i)*(6.882*sqrt(B*E(i)) - 1.708)) *...
    (1 - sqrt(E_th /E(i)))^s;
end

figure
loglog(E, YamamuraYieldExplicit, 'b');
xlabel('Ion energy (eV)')
ylabel('Sputtering yield (atoms/ion)')
xlim([10 1e6])
ylim([1e-3 1e2])

YieldExpressionForPICMC = sprintf('(E>%d) ? (%f/(1+%f*%f*(%g*E)^(0.3))*(3.441*
  sqrt(%g*E)*ln(%g*E+2.718)/(1+6.355*sqrt(%g*E)+%g*E*(6.882*sqrt(%g*E)-1.708))))
  *(1-sqrt(%f/E))^(%g) ! 0', E(1), A, Gamma, k_e, B, B, B, B, B, B, E_th, s);
disp(YieldExpressionForPICMC)
```

It relies on the following Matlab function:

```
%Computes sputtering yield parameters depending on atom 1 and
%atom 2 for PICMC simulation formula
%Based on ENERGY DEPENDENCE OF ION-INDUCED SPUTTERING YIELDS
%FROM MONATOMIC SOLIDS AT NORMAL INCIDENCE, Y. Yamamura and H. Tawara
%Atomic Data and Nuclear Data Tables 62, 149-253 (1996)

function [A, Gamma, k_e, B, E_th] = SputteringYieldForSimulation(Q, U_s, w, M1,
  M2, Z1, Z2)
k_e = 0.079 * (M1+M2)^(3/2)/(M1^(3/2)*M2^(1/2))*Z1^(2/3)*Z2^(1/2)/(Z1^(2/3) + Z2
  ^(2/3))^(3/4);
Gamma = w / (1 + (M1/7) ^ 3);

if M1 <= M2
    alpha = 0.249 * (M2/M1)^(0.56) + 0.0035*(M2/M1)^(1.5);
else
    alpha = 0.0875 * (M2/M1)^(-0.15) + 0.165*(M2/M1);
end

gamma = 4*M1*M2/(M1 + M2)^2;

if M1 <= M2
    E_th = U_s * (1 + 5.7* (M1/M2))/gamma;
else
    E_th = U_s * 6.7/gamma;
end

A = 0.042*alpha*Q/U_s * 84.78 * Z1 * Z2 * M1 /((Z1^(2/3) + Z2^(2/3))^(1/2)*(M1+M2
  )); %Part of equation (15)
B = 0.03255/(Z1*Z2*(Z1^(2/3)+Z2^(2/3))^(1/2))*M2/(M1+M2); %Equation (22)
end
```

B Discussion on simulated sputtering yields

For each 3D plasma simulation presented in this work, the actual sputtering yield $Y(E_{ion})$ is computed as the ratio of the production rate of niobium atoms sputtered from the cathode to the number of argon ions bombarding the cathode. These sputtering yields can be compared with values of sputtering yields $Y(V_{dis})$ computed with Yamamura's formula [6] by assuming that $E_{ion} = V_{dis}$, where E_{ion} is the impinging ion energy, and V_{dis} is the cathode voltage. A summary of $\frac{Y(E_{ion})}{Y(V_{dis})}$ with respect to the discharge pressure for each group of simulations is shown in figure B.1. Though the simulations involve different systems and magnetic configurations, it can be seen that increasing the pressure leads to a decrease of the yield ratio. This can be explained by the mechanism of charge exchange between ions and neutrals in the cathode sheath[78, 79, 80]. Indeed, at higher pressures, ions are more likely to lose their kinetic energy to neutrals through collisions, which means that the average ion energy at the cathode surface is decreased and in turn leads to a reduction of the sputtering yield under ion bombardment. Also, it is worth recalling that sputtering caused by bombardment of high energy neutrals was not included in this work, although it can start to have a non-negligible contribution on the total number of sputtered species at high pressures. The influence of this contribution will be investigated in future work.
Nevertheless, figure B.1 justifies the need for self-consistently determined sputtering profiles in the plasma simulation rather than assimilating ion energies to the cathode fall voltage, when quantitative analysis is pursued.

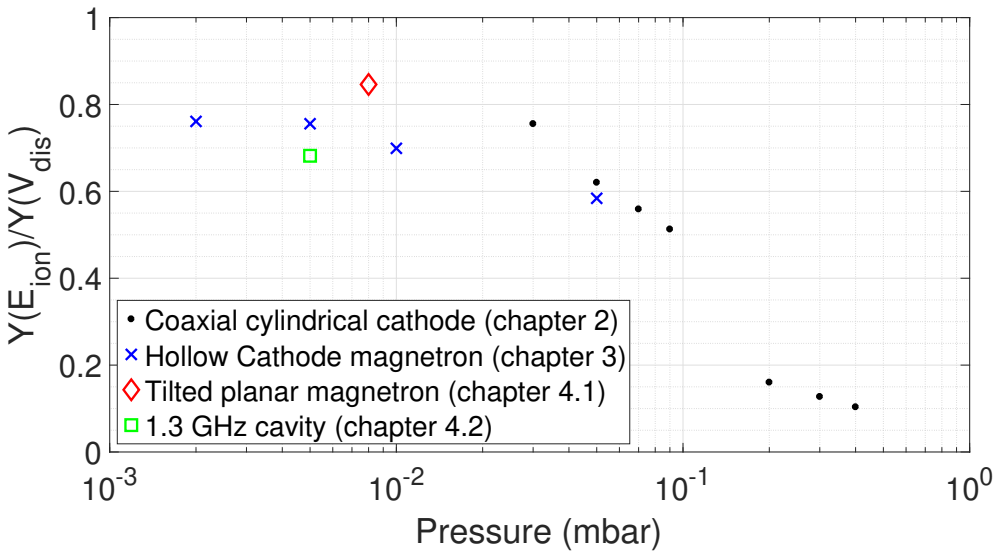

Figure B.1 – Comparison of $\frac{Y(E_{ion})}{Y(V_{dis})}$ for all simulations presented in this work.

C Discussion on additional results on the 1.3 GHz elliptical cavity case study

In this appendix, we present two complementary results on the 1.3 GHz cavity case study investigated in section 4.2. We first show a preliminary study regarding the impact of the cathode erosion profile on the plasma simulation stability. Then, we discuss the change of process gas by comparing experimental thickness profiles obtained with argon and krypton.

Eroded cathode simulation divergence

A perfectly non-eroded cylindrical cathode was considered in the previous study, as its shape would be prior to its first coating. However, cathodes are not replaced after each cavity coating, and as such usually present erosion profiles. The influence of the cathode erosion on the plasma simulation is studied by modifying the simulated cathode geometry according to figure C.1(a) with a peak erosion of 1.5 mm at the center out of 3 mm cathode thickness, close to the real cathode erosion of figure C.1(b), while keeping all other parameters unchanged. The minimum distance between the cathode surface and the magnet surface becomes equal to 5.5 mm instead of 7 mm without erosion.

As can be seen in figure C.2, the eroded cathode simulation case is rapidly diverging compared with the perfectly cylindrical cathode case: the discharge voltage is falling to 0, while the discharge current is dramatically increasing. Indeed, taking into account the cathode erosion profile means that the magnetic field at the cathode surface is locally higher, thus providing a better plasma confinement at its vicinity. This leads to high local plasma densities which are not compliant with the mesh size of 1 mm^3, as can be seen in figure C.3, where the electron density peak value of $3x10^{18}$ m^{-3} is 50 times larger than for the non-eroded cathode case of figure 4.14(a).

This study demonstrates the importance of the mesh size on the plasma simulation stability with respect to the simulated model geometry, and also opens a path towards taking into

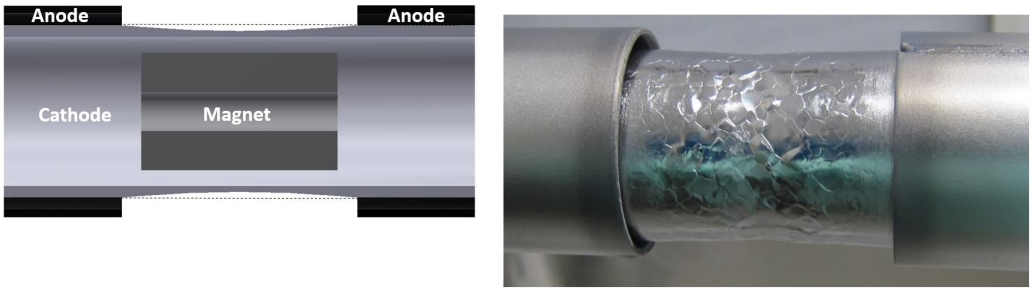

(a) (b)

Figure C.1 – (a) Half-view of the eroded cathode model. The peak erosion at the center is 1.5 mm out of 3 mm of cathode thickness. (b) Picture of an eroded cathode used for 1.3 GHz cavity coating.

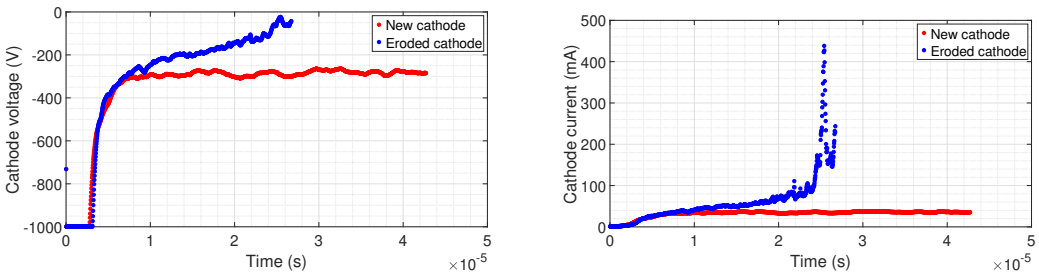

(a) (b)

Figure C.2 – 1.3 GHz cavity plasma simulation : influence of cathode erosion on discharge (a) voltage and (b) current time evolution.

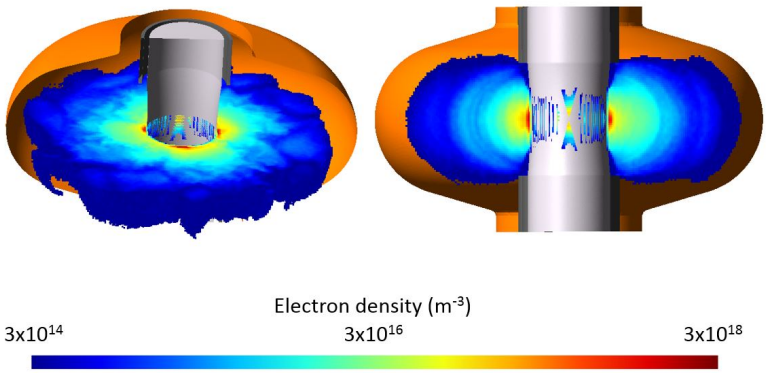

Figure C.3 – Half views of the simulated electron density for the eroded cathode case at t_{sim} = 26 μs.

account erosion profiles of used cathodes in plasma simulations. This last point could require a mesh size refinement in the high plasma density regions near the cathode.

Experimental comparison of thin film thickness with argon and krypton as process gases

Plasma simulations with krypton as the process gas were not investigated in this thesis study, and are left for future investigations. Nevertheless, krypton is also often used at CERN for coatings, and this section aims at comparing experimental results obtained for the 1.3 GHz cavity when the process gas is changed, and when the discharge power is scaled up while keeping *discharge power* × *coating time* constant, as discussed in section 4.1.
In addition to the coating presented before with argon as the process gas at a discharge power P_{dis} = 10 W (see figure 4.16), two coatings are performed with krypton at P_{dis} = 10 W and P_{dis} = 1000 W. The experimental coating parameters are listed in table C.1.

Table C.1 – Experimental parameters for the 1.3 GHz elliptical cavity coating with argon and krypton.

	1	2	3
Process gas	Argon	Krypton	Krypton
Pressure [mbar]	$5x10^{-3}$	$5x10^{-3}$	$5x10^{-3}$
Power [W]	10	10	1000
V [V]	289	240	347
i [mA]	35	43	3000
Coating time [min]	1320	1320	15
Cathode state	New	Eroded	Eroded

In order to keep *discharge power* × *coating time* constant in the three cases, thin film thickness profiles of cases 1 and 2 of table C.1 are linearly scaled from 1320 to 1500 minutes. XRF thickness measurements on copper bands identical to the ones of section 4.2.3 are shown in figure C.4.

Both thickness profiles using krypton at different discharge powers are almost identical, thus further confirming the power scaling results of section 4.1 for a real cavity geometry with a different process gas. Then, the change of process gas does not seem to greatly change the thickness profile shape and absolute values in this particular case, although the magnet misalignment and the subsequent profile asymmetry in the argon case added to different cathode erosion states for the three cases make difficult a more quantitative analysis.

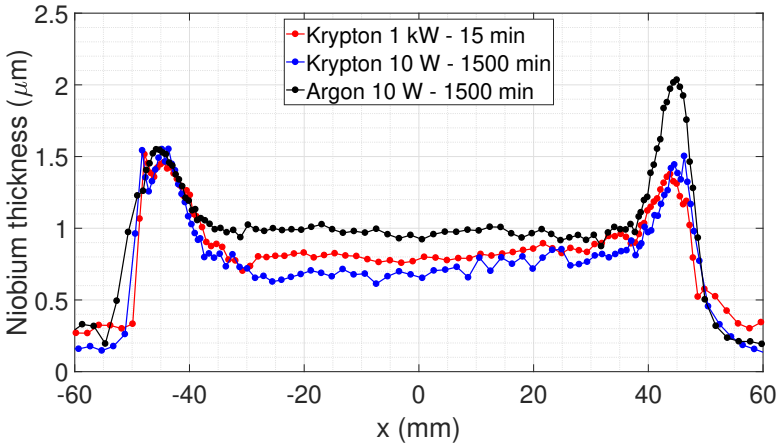

Figure C.4 – 1.3 GHz: comparison of thin film thickness profiles for argon and krypton, at different discharge powers, with *discharge power* × *coating time* constant.

Bibliography

[1] P. Chiggiato and P. Costa Pinto. Ti-Zr-V non-evaporable getter films: From development to large scale production for the Large Hadron Collider. *Thin Solid Films*, 515:382–388, 2006.

[2] C. Yin Vallgren, G. Arduini, J. Bauche, S. Calatroni, P. Chiggiato, K. Cornelis, P. Costa Pinto, B. Henrist, E. Metral, H. Neupert, G. Rumolo, E. Shaposhnikova, and M. Taborelli. Amorphous carbon coatings for the mitigation of electron cloud in the CERN Super Proton Synchrotron. *Physical Review Special Topics - Accelerators and Beams*, 14:071001, 2011.

[3] S. Calatroni. 20 years of experience with the Nb/Cu technology for superconducting cavities and perspectives for future developments. *Physica C*, 441:95–101, 2006.

[4] Simulation group webpage of Fraunhofer IST. https://www.ist.fraunhofer.de/en/our-services/simulation.html. Accessed: 2018-09-24.

[5] NASCAM webpage, University of Namur, Belgium. https://www.unamur.be/sciences/physique/larn/logiciels/nascam. Accessed: 2018-11-21.

[6] Y. Yamamura and H. Tawara. Energy dependence of ion-induced sputtering yields from monatomic solids at normal incidence. *Atomic Data and Nuclear Data Tables*, 62:149–253, 1996.

[7] A.-M. Valente-Feliciano. Superconducting RF materials other than bulk niobium: a review. *Superconductor Science and Technology*, 29:113002, 2016.

[8] S. Turner, editor. *Superconductivity in Particle Accelerators*. CERN Accelerator School, 1988. 30 May - 3 June 1988, Hamburg, Fed. Rep. Germany.

[9] C. Benvenuti, N. Circelli, and M. Hauer. Niobium films for superconducting accelerating cavities. *Applied Physics Letters*, 45:583–584, 1984.

[10] N. Jecklin, S. Calatroni, B. Delaup, L. Ferreira, I. Mondino, A. Sublet, M. Therasse, and W. Venturini Delsolaro. Niobium coatings for the HIE-ISOLDE QWR superconducting accelerating cavities, TUP073. In *Proceedings of the 16th International Conference on RF Superconductivity (SRF2013), 23-27 September 2013, Paris, France*, pages 611–613.

[11] A. Grudiev, S. Atieh, R. Calaga, S. Calatroni, O. Capatina, F. Carra, G. Favre, L. M. A Ferreira, J.-F. Poncet, T. Richard, A. Sublet, and C. Zanoni. Design of a compact superconducting crab-cavity for LHC using Nb-on-Cu coating technique, THPB048. In *Proceedings of the 17th International Conference on RF Superconductivity (SRF2015), 13-18 September 2015, Whistler, BC, Canada*.

[12] J. T. Gudmundsson and A. Hecimovic. Foundations of DC plasma sources. *Plasma Sources Science and Technology*, 26:123001, 2017.

[13] Y. P. Raizer. *Gas Discharge Physics*. Springer-Verlag Berlin Heidelberg, 1991.

[14] M. A. Lieberman and A. J. Lichtenberg. *Principles of Plasma Discharges and Materials Processing*. New Jersey: Wiley, 2nd edition, 2005.

[15] R. Hippler, H. Kersten, M. Schmidt, and K. H. Schoenbach. *Low Temperature Plasmas: Fundamentals, Technologies and Techniques*, volume 1. Wiley, 2nd edition, 2008.

[16] R. A. Baragiola, E. V. Alonso, J. Ferron, and A. Oliva-Florio. Ion-induced electron emission from clean metals. *Surface Science*, 90:240–255, 1979.

[17] J. Ferron, E. V. Alonso, R. A. Baragiola, and A. Oliva-Florio. Electron emission from molybdenum under ion bombardment. *Journal of Physics D: Applied Physics*, 14:1707–20, 1981.

[18] H. D. Hagstrum. Theory of Auger Ejection of Electrons from Metals by Ions. *Physical Review*, 96:336–365, 1954.

[19] L. M. Kishinevsky. Estimation of electron potential emission yield dependence on metal and ion parameters. *Radiation Effects*, 19:23–27, 1973.

[20] N. Benazeth. Review on kinetic ion-electron emission from solid metallic targets. *Nuclear Instruments and Methods*, 194:405–413, 1982.

[21] D. Depla, S. Mahieu, and R. De Gryse. Magnetron sputter deposition: Linking discharge voltage with target properties. *Thin Solid Films*, 517:2825–2839, 2009.

[22] J. R. Rumble. *CRC Handbook of Chemistry and Physics*. CRC Press/Taylor & Francis, Internet Version, 99th edition, 2018.

[23] A. V. Phelps and Z. Lj. Petrovic. Review article: Cold-cathode discharges and breakdown in argon: surface and gas phase production of secondary electrons. *Plasma Sources Science and Technology*, 8:R21–R44, 1999.

[24] W. R. Grove. VII. On the electro-chemical polarity of gases. *Philosophical Transactions of the Royal Society*, 142:87–101, 1852.

[25] P. Sigmund. Theory of Sputtering. I. Sputtering Yield of Amorphous and Polycristalline Targets. *Physical Review*, 184:383–416, 1969.

[26] M. W. Thompson. Physical mechanisms of sputtering. *Physics Reports*, 69:335–371, 1981.

[27] G. K. Wehner and D Rosenberg. Angular distribution of sputtered material. *Journal of Applied Physics*, 31:177–179, 1960.

[28] Y. Yamamura, T. Takiguchi, and M. Ishida. Energy and angular distributions of sputtered atoms at normal incidence. *Radiation Effects and Defects in Solids*, 118:237–261, 1991.

[29] M. Stepanova and S. K. Dew. Estimates of differential sputtering yields for deposition applications. *Journal of Vacuum Science and Technology A*, 19:2805–2816, 2001.

[30] Z. L. Zhang and L. Zhang. Anisotropic angular distribution of sputtered atoms. *Radiation Effects and Defects in Solids*, 159:301–307, 2004.

[31] L. Zhang and Z. L. Zhang. Anisotropic energy distribution of sputtered atoms induced by low energy heavy ion bombardment. *Radiation Effects and Defects in Solids*, 160:337–347, 2005.

[32] R. Behrisch and W. Eckstein. *Sputtering by Particle Bombardment*. Springer-Verlag Berlin Heidelberg, 2007.

[33] F. M. Penning. *Physica*, 4:71–75, 1937.

[34] W. D. Gill and E. Kay. Efficient low pressure sputtering in a large inverted magnetron suitable for film synthesis. *Review of Scientific Instruments*, 36:277–282, 1965.

[35] K. Wasa and S. Hayakawa. Low pressure sputtering system of the magnetron type. *Review of Scientific Instruments*, 40:693–697, 1969.

[36] J. E. Greene. Review article: Tracing the recorded history of thin-film sputter deposition: From the 1800s to 2017. *Journal of Vacuum Science and Technology*, 35:05C204, 2017.

[37] J. A. Thornton. Magnetron sputtering: basic physics and application to cylindrical magnetrons. *Journal of Vacuum Science and Technology*, 15:171–177, 1978.

[38] G. Buyle. *Simplified model for the d.c. planar magnetron discharge*. PhD thesis, Gent University, 2004.

[39] N. Brenning, J. T. Gudmundsson, D. Lundin, T. Minea, M. A. Raadu, and U. Helmersson. The role of ohmic heating in dc magnetron sputtering. *Plasma Sources Science and Technology*, 25:065024, 2016.

[40] S. Calatroni, A. Miyazaki, G. Rosaz, A. Sublet, and W. Venturini Delsolaro. Performance analysis of superconducting RF cavities for the cern rare isotope accelerator. *Physical Review Accelerators and Beams*, 19:092002, 2016.

[41] J. A. Thornton. Influence of apparatus geometry and deposition conditions on the structure and topography of thick sputtered coatings. *Journal of Vacuum Science and Technology*, 11:666–670, 1974.

[42] A. Anders. A structure zone diagram including plasma-based deposition and ion etching. *Thin Solid Films*, 518:4087–4090, 2010.

[43] Helmut Fischer GmbH webpage. https://www.helmut-fischer.ch/en/switzerland/. Accessed: 2018-10-10.

[44] Carl Zeiss Microscopy webpage - Microscopes ZEISS Crossbeam 340 et Crossbeam 540. https://www.zeiss.fr/microscopie/produits/fib-sem-instruments/crossbeam.html. Accessed: 2018-12-21.

[45] DSMC/PIC-MC Fraunhofer IST Code Documentation. https://simulation.ist.fraunhofer.de/doku.php?id=start. Accessed: 2018-10-03.

[46] T. Melzig, M. Siemers, A. Pflug, and R. Rank. 3D PIC-MC simulation of anode effects in dual magnetron discharges. *Surface and Coatings Technology*, 241:30–32, 2014.

[47] M. Siemers, A. Pflug, T. Melzig, K. Gehrke, A. Weimar, and B. Szyszka. Model based investigation of Ar^+ ion damage in DC magnetron sputtering. *Surface and Coatings Technology*, 241:50–53, 2014.

[48] A. Pflug, M. Siemers, T. Melzig, L. Schäfer, and G. Bräuer. Simulation of linear magnetron discharges in 2D and 3D. *Surface and Coatings Technology*, 260:411–416, 2014.

[49] R. W. Hockney and J. W. Eastwood. *Computer Simulation using Particles*. Taylor and Francis Group, New York, 1988.

[50] C. K. Birdsall and A. B. Langdon. *Plasma Physics via Computer Simulation*. Adam Hilger, Bristol, 1991.

[51] C. K. Birdsall. Particle-in-Cell Charged-Particle Simulations, Plus Monte Carlo Collisions With Neutral Atoms, PIC-MCC. *IEEE Transactions on Plasma Science*, 19:65–85, 1991.

[52] D. Tskhakaya, K. Matyash, R. Schneider, and F. Taccogna. The particle-In-Cell Method. *Contributions to Plasma Physics*, 47:563–594, 2007.

[53] H. Ueda, Y. Omura, H. Matsumoto, and T. Okuzawa. A study of the numerical heating in electrostatic particle simulations. *Computer Physics Communications*, 79:249–259, 1994.

[54] G. A. Bird. *Molecular gas dynamics and the direct simulation of gas flows*. Oxford University Press, Oxford, 1994.

[55] A. V. Phelps. Cross Sections and Swarm Coefficients for Nitrogen Ions and Neutrals in N2 and Argon Ions and Neutrals in Ar for Energies from 0.1 eV to 10 keV. *Journal of Physical and Chemical Reference Data*, 20:557–573, 1991.

[56] A. V. Phelps. The application of scattering cross sections to ion flux models in discharge sheaths. *Journal of Applied Physics*, 76:747–753, 1994.

[57] Cross sections between ions and atoms gathered by A. V. Phelps, JILA, University of Colorado. https://web.archive.org/web/20161102161406/http:/jilawww.colorado.edu:80/~avp/collision_data/ionneutral/IONATOM.TXT. Accessed: 2018-11-01.

[58] C. Geuzaine and J.F. Remacle. Gmsh: A 3-D finite element mesh generator with built-in pre- and post-processing facilities. *International Journal for Numerical Methods in Engineering*, 79:1309–1331, 2009.

[59] A. A. Abrahamson. Born-Mayer-Type Interatomic Potential for Neutral Ground-State Atoms with Z = 2 to Z = 105. *Physical Review*, 178:76–79, 1969.

[60] S. Senthil Nathan, G. Mohan Rao, and S. Mohan. Transport of sputtered atoms in facing targets sputtering geometry: A numerical simulation study. *Journal of Applied Physics*, 84:564–571, 1998.

[61] H. Hofsäss, K. Zhang, and A. Mutzke. Simulation of ion beam sputtering with SDTrimSP, TRIDYN and SRIM. *Applied Surface Science*, 310:134–141, 2014.

[62] H. M. Mott-Smith and I. Langmuir. The theory of collectors in gaseous discharges. *Physical Review*, 28:727–763, 1926.

[63] I. Furno, C. Theiler, V. Chabloz, A. Fasoli, and J. Loizu. Pre-sheath density drop induced by ion-neutral friction along plasma blobs and implications for blob velocities. *Physics of Plasmas*, 21:012305, 2014.

[64] F. F. Chen. Langmuir probe analysis for high density plasmas. *Physics of Plasmas*, 8:3029–3041, 2001.

[65] P. Guittienne, A. A. Howling, and I. Furno. Two-fluid solutions for Langmuir probes in collisionless and isothermal plasma, over all space and bias potential. *Physics of Plasmas*, 25:093519, 2018.

[66] G. Buyle, W. De Bosscher, D. Depla, K. Eufinger, J. Haemers, and R. De Gryse. Recapture of secondary electrons by the target in a DC planar magnetron discharge. *Vacuum*, 70:29–35, 2003.

[67] P. N. Giuliano and I. D. Boyd. Modeling particle-induced electron emission in a simplified plasma Test Cell. *Journal of Applied Physics*, 113:113302, 2013.

[68] Autodesk Inventor Software webpage. https://www.autodesk.co.uk/products/inventor/overview. Accessed: 2018-12-07.

[69] Opera Simulation Software webpage. https://operafea.com. Accessed: 2018-12-07.

[70] J. A. Thornton. End-effects in cylindrical magnetron sputtering sources. *Journal of Vacuum Science and Technology*, 16:79–80, 1979.

[71] E. Klawuhn, G. C. D'Couto, K. A. Ashtiani, P. Rymer, M. A. Biberger, and K. B. Levy. Ionized physical-vapor deposition using a hollow-cathode magnetron source for advanced metallization. *Journal of Vacuum Science & Technology A*, 18:1546–1549, 2000.

[72] G. C. D'Couto, G. Tkach, K. A. Ashtiani, L. Hartsough, E. Kim, R. Mulpuri, D. B. Lee, K. Levy, M. Fissel, S. Choi, S.-M. Choi, H.-D. Lee, and H.-K. Kang. In situ physical vapor deposition of ionized Ti and TiN thin films using hollow cathode magnetron plasma source. *Journal of Vacuum Science & Technology B: Microelectronics and Nanometer Structures Processing, Measurement, and Phenomena*, 19:244–249, 2001.

[73] U. Helmersson, M. Lattemann, J. Bohlmark, A. P. Ehiasarian, and J. T. Gudmundsson. Ionized physical vapor deposition (IPVD): A review of technology and applications. *Thin Solid Films*, 513:1–24, 2006.

[74] Maurer Magnetic AG website. http://maurermagnetic.ch/055_E_Informationen.html. 5. Technical informations, 51. Properties of Materials. Accessed: 2018-10-25.

[75] Finite Element Method Magnetics homepage, D. Meeker. http://www.femm.info. Accessed: 2018-10-25.

[76] D. Depla, S. Heirwegh, S. Mahieu, J. Haemers, and R. De Gryse. Understanding the discharge voltage behavior during reactive sputtering of oxides. *Journal of Applied Physics*, 101:013301, 2007.

[77] A. Palmero, H. Rudolph, and F. H. P. M. Habraken. Study of the gas rarefaction phenomenon in a magnetron sputtering system. *Thin Solid Films*, 515:631–635, 2006.

[78] W. D. Davis and T. A. Vanderslice. Ion Energies at the Cathode of a Glow Discharge. *Physical Review*, 131:219–228, 1963.

[79] D. Czekaj, E. K. Hollmann, A. B. Kozirev, V. A. Volpyas, and A. G. Zaytsev. Ion Energies at the Cathode of the DC Planar Magnetron Sputtering Discharge. *Applied Physics A : Solids and Surfaces*, 49:269–272, 1989.

[80] C. V. Budtz-Jørgensen, J. Bøttiger, and P. Kringhøj. Energy spectra of particles bombarding the cathode in glow discharges. *Vacuum*, 56:9–13, 2000.

[81] Zeiss O-Inspect 863 Data Sheet. https://applications.zeiss.com/C1257A26006EFF9E/0/B360533B411E9B94C1257A45002E8996/$FILE/O-INSPECT_EN_60_022_0343IX.pdf. Page 3, Optical confocal white light distance sensor, Measuring range 3 mm. Accessed: 2018-11-09.

[82] J. Sekutowicz. TESLA superconducting accelerating structures. *Measurement Science and Technology*, 18:2285–2292, 2007.

[83] H. Hayano. Review of SRF cavities for ILC, XFEL, and ERL applications, THXRA02. In *Proceedings of the International Particle Accelerator Conference (IPAC'10), May 23-28 2010, Kyoto, Japan*, pages 3625–3629.

[84] J. Dervaux, P.-A. Cormier, P. Moskovkin, O. Douheret, S. Konstantinidis, R. Lazzaroni, S. Lucas, and R. Snyders. Synthesis of nanostructured Ti thin films by combining glancing angle deposition and magnetron sputtering: A joint experimental and modeling study. *Thin Solid Films*, 636:644–657, 2017.

[85] J. M. Nieuwenhuizen and H. B. Haanstra. Microfractography of thin films. *Philips Technical Review*, 27:87–91, 1966.

[86] M. Wu, J. Moulin, and A. Bosseboeuf. Oblique angle deposition of Au/Ti porous getter films. *Journal of Applied Physics*, 124:055301, 2018.

[87] R. N. Tait, T. Smy, and M. J. Brett. Modelling and characterization of columnar growth in evaporated films. *Thin Solid Films*, 226:196–201, 1993.

[88] C. Benvenuti, S. Calatroni, I. E. Campisi, P. Darriulat, M. A. Peck, R. Russo, and A.-M. Valente. Study of the surface resistance of superconducting niobium films at 1.5 GHz. *Physica C*, 316:153–188, 1999.

[89] S. Amorosi, M. Anderle, C. Benvenuti, S. Calatroni, J. Carver, P. Chiggiato, H. Neupert, and W. Vollenberg. Study of the discharge gas trapping during thin-film growth. *Vacuum*, 60:89–94, 2001.

Thibaut Richard

Born: Saint Nazaire, 13 December 1989
Nationality: French

Education

January 2015-February 2019 — **PhD student in Plasma Physics**, *CERN-TE-VSC/EPFL-SPC*, Geneva.
Experiments and modelling for glow discharge plasmas applied to niobium sputter deposition in superconducting radiofrequency cavities
Validation of a Particle-in-Cell plasma simulation code by comparison of the plasma parameters with experimental data
Application to real cavity geometries and prediction of coating profiles

2010–2014 — **Engineering school in Aeronautics and Space**, *ISAE-Supaero*, Toulouse.
Specialization in Applied Mathematics and Universe Sciences

2013-2014 — **Master of Research**, *Paul Sabatier University*, Toulouse.
Fundamental and Applied Mathematics

2007-2010 — **Classes Préparatoires aux Grandes Ecoles**, *Lycée Louis Le Grand*, Paris.
Physics and Chemistry Specialization

Experience and Projects

April 2014/September 2014 — **Master Thesis**, *ISAE-ONERA*, Toulouse.
Mathematical modelling and numerical simulation of Dielectric Barrier Discharge plasma actuators for aerodynamic flow control
Modelling of a realistic air kinetics set of chemical reactions
Numerical simulation of a DBD and comparison with experimental results

September 2012/August 2013 — **Technical Student Programme**, *CERN-TE-VSC*, Geneva.
Numerical simulation of ionization pressure gauges in Ultra-High Vacuum
Optimization of the gauges characteristics with the Vector Fields-Opera 3D software
Participation in the laboratory activities : calibration of gauges and residual gas analyzers

Languages

French — **Mother tongue**.
English — **Advanced level**, *C1*.
Italian — **Basic**.

Ce document a été imprimé au Centre d'impression EPFL,
imprimerie climatiquement neutre, certifiée myClimate.